Optical Modulation by Controlling the Charge State of Deep Impurity Levels in Silicon

McMaster University

McMaster University

Optical Modulation by Controlling the Charge State of Deep Impurity Levels in Silicon

by

ÉDGAR HUANTE-CERÓN

B.Eng. (UAM-A, México) 1998
M.Sc. (CICESE, México) 2001

A Thesis
Submitted to the School of Graduate Studies
in Partial Fulfilment of the Requirements
for the Degree
Doctor of Philosophy

McMaster University
©Copyright by Édgar Huante-Cerón, 2011

McMaster University

DOCTOR OF PHYLOSOPHY (2011) McMaster University
(Engineering Physics) Hamilton, Ontario

TITLE: Optical Modulation by Controlling the Charge State of Deep Impurity Levels in Silicon

AUTHOR: Édgar Huante-Cerón

SUPERVISOR: Dr. A. Knights and Dr. P. Jessop

NUMBER OF PAGES: xvi, 183

McMaster University

Abstract

Measurements of thallium and indium doped Silicon-On-Insulator rib waveguides show optical absorption at a wavelength of 1550nm, dependent on the charge state of the associated deep-level. Therefore, it is possible to use this effect to modulate waveguide transmission by means of local depletion and/or injection of free-carriers to change deep-level occupancy. A one-dimensional model based on the generation and recombination process described by the modified Shockley-Read-Hall (SRH) mechanism was developed using MATLAB© programming language in order to compute the optical absorption of a 1550nm wavelength as a function of the density of neutrally-charged thallium or indium centers. This numerical model is in reasonable agreement with the experimental data for samples co-doped with low and medium phosphorus concentrations. The values of optical absorption cross-section calculated for thallium are $2.9\times10^{-17} \pm 0.25\text{cm}^2$ and $3.2\times10^{-17} \pm 0.12\text{cm}^2$ for ion implantation doses of $7.4\times10^{-13}\text{cm}^{-2}$ and $1.2\times10^{-14}\text{cm}^{-2}$, respectively. Also described is the the design, fabrication and characterization of an optical modulator using a four-terminal p^+pnn^+ diode on an indium-doped Silicon-On-Insulator rib waveguide. Modulation by controlling the charge state of deep impurity levels in silicon was thus demonstrated. Modulation bandwidth in the 2-10MHz regime was measured and the depth of modulation is approximately 0.48dB/V in forward bias and 0.25dB/V in reverse bias. This is the first report of the implementation of an optical silicon-waveguide modulator based on a periodically interleaved *pn*-junction configuration. In addition, the influence of indium, as a dopant in silicon (utilizing the Impurity Photovoltaic Effect), as a means to increase the efficiency of a thin film silicon solar cell was investigated using the same samples. Under certain doping conditions and geometrical configurations, a cell efficiency greater than 24% was measured —a somewhat remarkable result for these silicon thin films of 2.5μm.

McMaster University

McMaster University

Acknowledgements

This work could not be finished without the help of a great group of people, in particular my supervisors of whom I am deeply grateful, thank you Dr. Andrew Knights and Dr. Paul Jessop for believing in me at a time that I even did not believe in myself, and for giving me financial, technical and moral support to continue and finish this, sometimes frustrating, path called PhD.

I would like to thank Dr. Chang-Qing Xu for being part of my committee, to Doug Bruce for his readiness because every single time I asked for help, he always gave it to me, no matter the topic or subject, to Graham Pearson for always been willing to help, to Doris Stevanovic for sharing her experience and knowledge, to Zhilin Peng for being so helpful solving whatever problem occurred in the clean room and to the rest of the persons working in the CEDT, to Jim Garret for his help with the vacuum systems and annealing process, and for allowing me to modify a vacuum system for Freeze-drying, and to Jack Hendriks for the ion implantation.

To my father, who gave us the best example of life and taught us not to give up in achieving our dreams and who left this world before we expect it. To my mother who has been and always will be my biggest supporter, to my brothers Alejandro and Jose Ignacio, and the rest of my family, to Julia's parents and sisters who always help us and continuously are trying to convince us to move to the beautiful Vancouver, and last but not least to that great woman without whom this thesis could not be completed, thank you Julia for your love, friendship and overall your patience.

One time I was asked about what I liked the most in my PhD and without any doubt I said: "*all the people I met along that time*". Therefore, I would like to thank all my friends that directly and indirectly participated in the creation of this thesis

McMaster University

with special mention to my great friend Jorge Fonseca for joining me in this incredibly journey, to Ana Villafranca for offering her friendship since the first moment we met, to Robert Lockhart for his unconditional friendship and patience to introduce me to the Canadian way of life, to Ruchi Gupta, Andrei Zdanovich and Yuan He for that great moments and experiences in our small office, to Mike Bulk for showing me the trick and tips of the waveguide coupling, to Chris Brooks for sharing his knowledge, to Manuel Campidelli for being a sincere friend, to Somaradi Khiev for the irreverent way of being herself, to Adam Prescot for proving me that the reality is just an illusion produce by the lack of alcohol. To all the people in the silicon-photonics lab who make this time an enjoyable one, thank you Shabnam Homampour, Dylan Logan, Jason Ackert, Thomas Jacob, Jonathan Doylend, Joel Milgram, David Walters, John Gelleta. My sincere thanks to Fabiola Vallejo, Arun Vady, Lina Gunawan, Shery Chang, Arnaud Weck, Hector, Martin Couillar, Carmen, Paul Drider, Andrew Younker, Jonathan Bradley, Abhi Rampal, Akihide, Nooshin Tajik, Simona Salati, Travis, Tayler, Carlos, Lidia, Parsian, Francisco Ucan to CONACYT and IPN for the financial support and to you that I forgot without meaning it.

Unluckily fake or a fame.

McMaster University

Contents

Manchester University

McMaster University

List of Figures

McMaster University

Uncorrected Version

Manuscript

McMaster University

List of Tables

McMaster University

Chapter 1

Introduction and Motivation

In the search for smaller and faster data transfer components, the silicon industry is reaching its limit in size, device integration and complexity, as the physical limitations of metallic interconnects begin to constrain the future of microelectronics [1, 2]. The solution may be *silicon photonics*, a technology that employs silicon as an optical material, and which has been driven by recent technological advances and increasing investment by governments and the private sector. Silicon photonics represents a combination of existing silicon manufacturing capability[1] with the advantages of optical telecommunications[2], whose premise is the implementation of an efficient and low loss platform at low cost. The resulting dual-function technology seems to be a viable approach to extending the limits imposed by conventional metal interconnects to high speed communications in modern computer systems [3–5], while the development of this technology opens the possibility of new applications in many different markets [6].

[1] High manufacturing volumes at low-cost

[2] Which is able to transmit information faster, further and that is completely immune to electromagnetic interference, in comparatione to copper cable

McMaster University

1.1 The Need for Silicon Photonics

Photonics is the technology responsible for the generation, modulation, transmission, processing and detection of photons (light). One of the most successful examples of application is fiber-optics for long-haul communications, although photonics plays a significant role in industries requiring sensing, data acquisition, micromachining, and more.

Fiber-optic communications is a well-established technology for information transmission. It enables tremendous data capacity (bandwidth), over transmission distances of hundreds of kilometers without the need for regeneration; while in a local data centre (communications distances up to about 100 meters), gigabits of data is transferred with almost no attenuation, which the performance of metal wires cannot compete. These properties may well be transferred to even shorter reach. For instance, at the present time, microprocessors have two or more cores as a response (a practical but temporary solution) to demands for higher performance. More instructions per cycle and demand for higher energy efficiency lead to the problem of heat dissipation which becomes more severe as the microprocessor clock speed increases (dissipation of so much power that the cooling requirements are more demanding with each generation) and metal connectors reduce in size. The demand for greater bandwidth plus the problem of power dissipation in metallic transmissions lines may be solved thanks to the advantages provided by optical interconnections. However, optical interconnect technology, after many years of development, still has a reputation for being an expensive solution, due to its use of exotic materials, low fabrication yield, tricky integration of different devices and costly manufacturing processes. Some examples of materials used in the manufacture of optical components include ferroelectric materials such as lithium niobate oxide ($LiNbO_3$), and III-V semiconductors

McMaster University

such as gallium arsenide ($GaAs$) and indium phosphide (InP). This situation motivates a relatively new field of research into using more common materials, such as silicon, for the fabrication of photonic components [6–8]. Silicon has excellent material properties important in photonics devices, such as high thermal conductivity, high optical damage threshold, a high quality and stable oxide, a low-loss wavelength window extending from $1.1\mu m$ to nearly $7\mu m$, and high third-order optical nonlinearities. In addition, silicon wafers have the lowest cost and the highest crystal quality of any semiconductor material. Nevertheless, silicon has some basic material drawbacks. It is an inefficient light generator; the electro-optic (Pockels) effect is non-existent and there is no conventional photodetection in the region $1.3\mu m$-$1.6\mu m$ (communication band) [9, 10].

Optical interconnects will also have a role to play on the inter-and-intra-chip level. Estimates are that today 40 percent of the power needed to run a chip is consumed by moving data on and off the device [11]. Higher data rates (gigascale and terascale I/O) and more cores will drive this number higher. Using light as the communicator allows lower energy consumption when transmitting signals and optical interconnects are much better suited than copper to handling high data rates ($>$ 10Gb/s). Therefore, it is foreseen that the highest impact of silicon photonics may be in bringing the optical interconnection to the computer realm [12], resulting in an increase in computing speed and efficiency for microprocessors by reducing the response time between components and the heat dissipation. Additionally, silicon photonics is expected to influence other areas of technology like the sensing industry, biomedical applications, telecommunications and consumer electronics [13,14]. For a more detailed discussion on the motivation for silicon photonics the reader is referred to Zeno Gaburro's excellent chapter in the Pavesi and Lockwood text *Silicon Photonics* [14] which provides a comprehensive explanation about the problems associated

McMaster University

with electrical interconnects and the solution offered by an optical paradigm.

The biggest challenge for silicon photonics is the manufacture of efficient and low-cost information processing components. Ultimately, the biggest limitation on the success of the technology might not be the laws of physics but those of economics [15]. Therefore, silicon photonics is developed within the protocols of a manufacturing technology based on compatibility with the mature Complementary-Metal-Oxide-Semiconductor (CMOS) process and the availability of high-quality silicon-on-insulator (SOI) [16].

1.2 Silicon-On-Insulator Waveguides

Silicon-On-Insulator (SOI) is a generic term used to describe structures formed by a thin layer of crystalline silicon (Si) on an insulating layer, which typically is silicon dioxide (SiO_2) [17]. SOI optical waveguides possess unique optical properties due to the high transparency of silicon in the infrared spectrum and the large refractive index difference between silicon (guiding layer or core, $n = 3.45$) and SiO_2 (insulator layer or cladding, $n = 1.46$). This high difference in indices of refraction strongly confines the electromagnetic field into the silicon layer. These excellent optical properties, as well as compatibility with silicon CMOS integrated technology, enables low-cost optoelectronic integrated circuits [18].

The most common methods to manufacture SOI wafers are described here. *Separation by implanted oxygen* (SIMOX) was until 2000 the most popular method for large volume fabrication (no longer preferred). It is basically the implantation of high doses ($> 10^{18}\text{cm}^{-2}$) of oxygen ions below the surface of a silicon wafer. In order to prevent an amorphous silicon overlayer from forming during implantation the

McMaster University

wafer is kept at high temperatures ($\sim 600°C$) during implantation. The thickness of the silicon overlayer is determined by the energy used for oxygen implantation since that determines the depth of the SiO_2. Due to the high oxygen doses, the peak concentration of the implantation profile saturates, thus producing a uniform concentration that results in a complete buried SiO_2 layer. After implantation the wafer is annealed approximately at 1300°C for several hours. This anneal removes implantation-related defects from the silicon overlayer and further defines the buried SiO_2 layer. The silicon overlayer thickness may be increased subsequent to ion implantation via epitaxial growth [17].

Another method for the formation of SOI is the *Bond and Etch-Back* (BESOI) technique. Initially, two silicon wafers are thermally oxidized. The two oxidized surfaces come into contact at room temperature to form a chemical bond which is subsequently strengthened by a thermal process at a temperature of approximately 1100°C. The thin silicon overlayer is formed by controllably removing one of the bonded wafers, typically, via Chemical Mechanical Polishing (CMP).

A technique which combines steps of both SIMOX and BESOI procedures is the *SmartCut Process*©. A silicon wafer is thermally oxidized and implanted with a high dose of hydrogen ions (10^{17}cm^2). The depth of the implantation peak depends on the energy used but generally is of the order of hundreds of nanometers to a few microns. Silicon lattice bonds are weakened as a result of the damage induced by the implantation coupled with the presence of hydrogen. At room temperature, a second wafer (with or without a thermally oxidized surface) is brought into contact with the implanted wafer, and the two weakly bond together. A thermal process at a temperature of 600°C is initially used to split the implanted wafer along the peak of the hydrogen concentration profile. A second thermal process at a temperature

McMaster University

of 1100°C is used to strengthened the bond between wafers. A fine CMP is used to reduced the surface roughness of the silicon overlayer. If required, the silicon overlayer thickness can be increased by epitaxial growth. The *SmartCut Process*© provides significant flexibility in final wafer dimension, coupled with high quality material. It is currently the most popular method for SOI formation.

There are multiple varieties of waveguide structures but it is the use of the ridge waveguide (Figure 1.1) that allows single mode propagation for relatively large waveguide dimensions and leads to low fiber-to-waveguide coupling loss. For optical wavelengths in the range of 1.3-1.55μm and silicon guiding layer thicknesses of a few microns, the thickness of the buried oxide (BOX) layer must be approximately one micron in order to prevent the evanescent field of the propagating signal from penetrating into the silicon substrate. A detailed description of the theory governing optical propagation in SOI structures is provided in chapter 2.

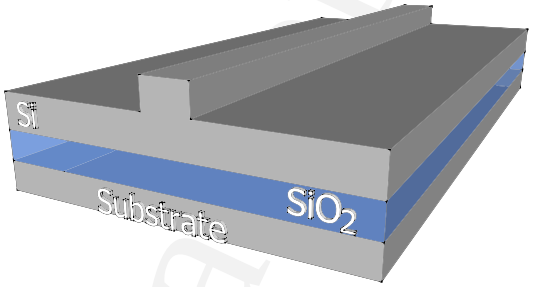

Figure 1.1: **Ridge waveguide made on a SOI platform.**

1.3 Optical modulation in a Silicon waveguide

Monolithic integration of optical and electrical components on one substrate provides the obvious progression to the vision of a fully integrated photonic system. As

was mentioned previously, the use of silicon for optical interconnects would allow such monolithic integration of microelectronics and optics [12]. Although the use of photonics on silicon was first proposed more than 30 years ago [7, 19], there remained many limiting factors preventing its implementation such as the lack of high quality and low price SOI and the mismatch between the thicknesses required for the waveguide layer and that required by the active electronic devices (the latter requires layer dimensions of less than a micron). However, it is in the last few years that submicrometer photonic structures have been realized making this monolithic integration possible. In order to fully exploit silicon as an integrated photonic material, a series of challenges still remains to be overcome. For example, it is well-known that silicon is an indirect semiconductor, which implies that it is an inefficient light source; while optical propagation losses have been found to increase as waveguide dimensions are reduced (mainly by the presence of side wall roughness); also silicon waveguides tend to have high fiber-to-waveguide coupling losses. Of great significance, silicon does not exhibit a linear electro-optic effect known as *the Pockels effect*, used for optical modulation in some semiconductors. In terms of detection, silicon is transparent in the wavelength range of 1300nm to 1550nm, commonly used in telecommunication [9,20].

Some of these challenges have been addressed to a greater or lesser degree. For example, propagation losses as low as 2.4 dB/cm for waveguides widths >500 nm [21] have been reported, while Raman scattering provides a method for optical amplification and lasing independent of the band structure of the material [2]. In 2005, a continuous wave silicon laser was demonstrated [22] using this effect. Another option for the integration of functionality is the incorporation of more emission-efficient III-V semiconductor compounds such as indium phosphide or indium gallium arsenide onto the silicon substrate, while the option to produce the light off-chip and use silicon only for modulation, routing and detection always remains. Many research groups thus

focus their attention on the development of active devices in silicon such as detectors and modulators. For example, a silicon-germanium avalanche photodiode with better performance than one built with more conventional III-V semiconductors [23] has been demonstrated.

The focus of this thesis is the exploration of novel methods for optical modulation in silicon waveguides. Optical modulators are devices that cause direct changes in the optical intensity of a light beam propagating in a waveguide. This is achieved via absorption, or by causing changes in the real part of the refractive index of the material (inducing a change in phase), which can be used to shift the relative phase of two propagating waves such that they interfere either constructively or destructively via an interferometer typically a Mach-Zehnder Interferometer (MZI) or a resonant device. These changes are usually produced via an applied electric field [24, 25]. *Electro-refraction* is known as the change in the real part of the refractive index (Δn) with an applied electric field, whereas *electro-absorption* is known as the change in the imaginary part of the refractive index ($\Delta \alpha$) [26, 27]. In semiconductors, the primary electric field effects are the *Pockels effect*, *Kerr effect* and *Franz-Keldysh effect*. However, the *Pockels effect* is non-existent in silicon and the *Kerr effect* and *Franz-Keldysh effect* are too weak in pure silicon at telecommunication wavelengths to be of any practical use [28,29]. A possible alternative is the *Thermo-optic effect* which is strong in silicon; however, it is too slow to be used in modern telecommunication (but still practical for sensing application). Therefore, the most common method (so far) of achieving fast optical modulation in silicon devices has been by means of the *plasma dispersion effect* [29–32], in which the concentration of free carriers in silicon changes the real and imaginary parts of the refractive index, discussing details in section 2.10. This effect relates the variation in the concentration of electrons (ΔN_e) and holes (ΔN_h) in a semiconductor to changes in the absorption coefficient ($\Delta \alpha$)

McMaster University

and refractive index (Δn), respectively. There are three device structures commonly used in silicon waveguides to electrically manipulate charge density interacting with propagating light: carrier injection in *forward-biased pin diodes*, carrier accumulation in *metal-oxide-semiconductors* (MOS) *capacitors*, and carrier depletion in *reverse-biased pn-diodes* [24, 33–35].

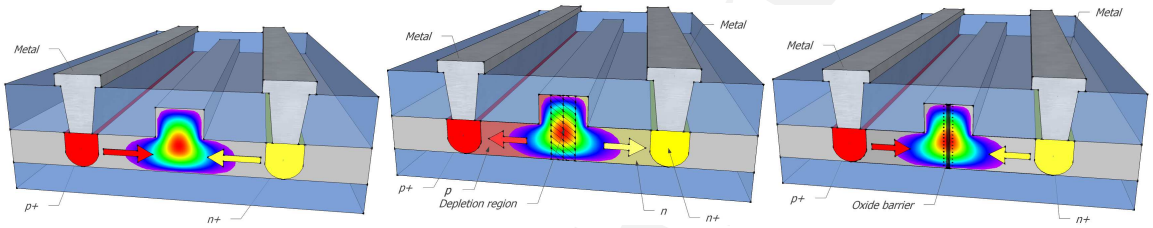

(a) (b) (c)

Figure 1.2: **Sketch of the three more common configuration used in silicon optical modulators based on the plasma-dispersion effect (a) Carrier injection, (b) carrier depletion and (c) carrier accumulation (MOS capacitors).**

In a *pin* $(p-type \mid intrinsic \mid n-type)$ *diode* structure, the waveguide is usually formed at the intrinsic region of the diode and the doping regions are located at a reasonable distance from the waveguide to avoid excessive loss resulting from the overlap between the doping regions and the optical mode. Electrons and holes can be injected into the path of the propagating light via the highly doped *n-region* and *p-region* respectively, such that either the refractive index or the absorption coefficient of the material can be modulated [36, 37]. The structure configuration of the MOS-capacitor is similar to the *pin*-diode with the difference that a thin dielectric layer is formed inside the waveguide to semblance a capacitor structure. The operating principle is based on carrier accumulation on either side of the thin dielectric layer inducing a change in the index of refraction and the absorption coefficient [38]. In

a device based on carrier depletion, the waveguide region is pre-doped forming a *pn*-junction which could be oriented either horizontally or vertically with respect to the buried oxide such as the light propagating in a waveguide interacts with the depletion region formed by the diode operated at reverse bias [39].

In this thesis, special interest is placed on the modulation of light in silicon waveguides based on the plasma dispersion effect. The novelty in the current work comes from the use of thallium as a deep level impurity in silicon, based on the recent demonstration of optical modulation by controlling the charge state of deep level impurities in silicon by Logan et. al. [40] and the construction of an optical modulator using indium as a deep level impurity in silicon waveguides to increase optical absorption. Furthermore, the geometrical configuration of the modulator proposed by Li et. al. [33] is adopted and is intended to improve the interaction between the depletion region (or metallurgical junction) and the optical mode propagating along the waveguide structure. The primary difference with respect to the traditional modulator configurations lies in how the *pn*-junction is oriented in the waveguide. Usually, the *pn*-junction is formed parallel to the light propagation direction and, for a reverse bias diode, the depletion region (usually a small depletion width) coincides with maximum intensity of the optical waveguide-mode[3]. The disadvantage of this configuration is that the depletion region only overlaps with a small portion of the optical mode and therefore modulation efficiency is relatively small. By arranging the *pn*-junctions perpendicular to the light propagation direction, the overlap between the optical mode and the depletion region is increased and therefore optical modulation improves considerably.

[3]The modulation efficiency is directly proportional to the overlapping between the optical mode and the depletion region

McMaster University

1.4 Thesis Contents

In the present chapter, the motivation for the research leading to this PhD thesis is given. Chapter II begins with the introduction of electromagnetic theory, followed by a description of dielectric waveguides and the "guiding" phenomena. There is a discussion provided on single mode propagation in a 3-D waveguide and its description by using an analytical formulation called the *effective index method*. Additionally, the *thermo-optic effect*, a particularly important phenomenon in silicon, is discussed. Analytical formulations for the typical losses observed in waveguide structures is presented. Optical absorption mechanisms in silicon are discussed and particular attention is focused on the absorption via free carriers.

Chapter III covers the numerical model developed by the author for optical modulation by controlling the charge state of deep impurity levels in silicon in which deep level refers to (in this case) that introduced by substitutional thallium in the silicon bandgap. The chapter begins with a numerical calculation of the occupancy fraction of the deep levels, followed by a discussion of sample fabrication and finally the experimental measurements of optical absorption in thallium-doped silicon waveguides. A comparison of the simulated results and experimental data is provided.

Chapter IV describes the optical modulation obtained by controlling the charge state of deep impurity levels in indium-doped silicon waveguides. The chapter begins with a description of different optical modulator configurations that use the plasma dispersion effect. In section 4.2 a new configuration proposed to improve the performance of modulators is introduced. Modulator fabrication is described in detail in section 4.4. Experimental results for the optical modulator are presented and discussed.

McMaster University

Chapter V contains final thoughts regarding the results presented in both chapter III and IV and discusses some possible improvements to the outcomes obtained and its consequences in future works.

1.5 A Summary of Novel Contributions in the Thesis

- Implementation of a numerical model for the calculation of optical absorption by deep-level centres in silicon.
- Demonstration of optical absorption in thallium-doped silicon waveguides.
- A report of the construction of a silicon waveguide modulator using perpendicularly oriented (to the propagation direction of the signal) *pn*-junctions.
- Demonstration of optical modulation in forward and reversed bias in indium-doped silicon waveguides.
- A proposal for improving the efficiency of solar cells by the use of the Impurity Photovoltaic (IPV) Effect together with the periodically arranged and vertically oriented *pn*-junctions designed initially for optical modulation.

McMaster University

Chapter 2

Background Theory

A layered media able to confine and guide electromagnetic fields in a specific direction is know as a *waveguide* and if the frequency of the electromagnetic field is in close proximity to the visible range it is known as an *optical waveguide*. The principle of electromagnetic radiation confinement is based upon the phenomenon of total internal reflection. The electromagnetic fields that are confined and guided are the so called *guided modes* or *guided waves* [41].

2.1 Electromagnetic Waves

The description of electromagnetic (EM) wave propagation has been presented in many excellent texts [27, 41–52]. In order to study the propagation of electromagnetic radiation in an isotropic medium, it is necessary to introduce Maxwell's equations. All electromagnetic waves, such as light, can be completely described by four field vectors that are functions of position and time. The description of these four field vectors – Electric Field intensity (**E** [V/m]), Magnetic field intensity (**H** [A/m]), Electric flux density (**D** [C/m^2]) and Magnetic flux density (**B** [Wb/m^2])– form Maxwell's equations,

McMaster University

$$\nabla \cdot \mathbf{D} = \rho \tag{2.1}$$

$$\nabla \cdot \mathbf{B} = 0 \tag{2.2}$$

$$\nabla \times \mathbf{E} = -\frac{\partial \mathbf{B}}{\partial t} \tag{2.3}$$

$$\nabla \times \mathbf{H} = \mathbf{J} + \frac{\partial \mathbf{D}}{\partial t} \tag{2.4}$$

In general, $\mathbf{E}$ and $\mathbf{H}$ are vectors commonly used to describe the electromagnetic field properties, and the vectors $\mathbf{D}$ and $\mathbf{B}$ are used to describe the effect of the field on matter. The quantities ρ [C/m^3] and $\mathbf{J}$ [A/m^2] are the electric charge density and current density, respectively, and may be considered as the source of the fields $\mathbf{E}$ and $\mathbf{H}$.

The physics of the propagating medium is contained in the following equations

$$\mathbf{D} = \epsilon \mathbf{E} = \epsilon_0 \mathbf{E} + \mathbf{P} \tag{2.5}$$

$$\mathbf{B} = \mu \mathbf{H} = \mu_0 \left(\mathbf{H} + \mathbf{M} \right) \tag{2.6}$$

$$\mathbf{J} = \sigma \mathbf{E} \tag{2.7}$$

where the parameters ϵ, μ and σ are tensors, known as the dielectric tensor (or permittivity tensor), the permeability tensor and the conductivity tensor, respectively. They are, in general, functions of the applied field intensity, position within the

McMaster University

medium, direction of the applied electric field and frequency of operation. **P** and **M** are the electric and magnetic polarization, respectively. The constant ϵ_0 is called the permittivity of vacuum and has a value of 8.854×10^{-12} F/m. The constant μ_0 is known as the permeability of vacuum and has a value of $4\pi \times 10^{-7}$ [V·s/(A·m)].

If the medium is isotropic, linear and non-dispersive, the polarization **P** and the magnetization **M** are defined in

$$\mathbf{P} = \epsilon_0 \chi_e \mathbf{E} \tag{2.8}$$

$$\mathbf{M} = \chi_m \mathbf{H} \tag{2.9}$$

where χ_e is the electric susceptibility and χ_m is the magnetic susceptibility. The substitution of equation (2.8) and equation (2.9) in equation (2.5) and equation (2.6), respectively, results in $\mathbf{D} = \epsilon_0 \epsilon_r \mathbf{E}$ and $\mathbf{B} = \mu_0 \mu_r \mathbf{H}$, where

$$\epsilon_r = 1 + \chi_e = \epsilon / \epsilon_0 \tag{2.10}$$

$$\mu_r = 1 + \chi_m = \mu / \mu_0 \tag{2.11}$$

with ϵ_r as the relative permittivity and μ_r as the relative permeability.

In cases where ρ and **J** vanish, and assuming that the medium is linear and isotropic, ϵ and μ became scalars. Using eq.(2.6) for **B** in eq.(2.3) and applying the curl operator to both sides, we obtain

McMaster University

$$\nabla \times (\nabla \times \mathbf{E}) = -\mu \frac{\partial}{\partial t} \nabla \times \mathbf{H} \tag{2.12}$$

and using the eq.(2.4) in the right hand side of the eq.(2.12), we obtain

$$\nabla \times (\nabla \times \mathbf{E}) = -\mu\epsilon \frac{\partial^2 \mathbf{E}}{\partial t^2} \tag{2.13}$$

and with the identity

$$\nabla \times (\nabla \times \mathbf{E}) = \nabla (\nabla \cdot \mathbf{E}) - \nabla^2 \mathbf{E} \tag{2.14}$$

eq.(2.13) becomes

$$\nabla^2 \mathbf{E} = \mu\epsilon \frac{\partial^2 \mathbf{E}}{\partial t^2} \tag{2.15}$$

which is the *wave equation* for the field vector **E**. The wave equation for the magnetic field vector **H** can be obtained in a similar way and is given by

$$\nabla^2 \mathbf{H} = \mu\epsilon \frac{\partial^2 \mathbf{H}}{\partial t^2} \tag{2.16}$$

These electromagnetic wave equations are satisfied by a monochromatic plane wave of the form

$$\mathbf{E}(\mathbf{r}, t) = \mathbf{E}_0(\mathbf{r}, t) \ \exp\Big\{ j(\mathbf{k} \cdot \mathbf{r} - \omega t) \Big\} \tag{2.17}$$

and

McMaster University

$$\mathbf{H}(\mathbf{r},t) = \mathbf{H}_0(\mathbf{r},t)\ \exp\Big\{j(\mathbf{k}\cdot\mathbf{r}-\omega t)\Big\} \tag{2.18}$$

respectively, where $\mathbf{E}_0$ and $\mathbf{H}_0$ are amplitudes; $\mathbf{r} = x\hat{\mathbf{a}}_x + y\hat{\mathbf{a}}_y + z\hat{\mathbf{a}}_z$ is the position vector, $\mathbf{k} = k_x\hat{\mathbf{a}}_x + k_y\hat{\mathbf{a}}_y + k_z\hat{\mathbf{a}}_z$ is the propagation vector and its magnitude $|\mathbf{k}| = k = 2\pi/\lambda$, and $\omega = 2\pi\nu$ is the angular frequency with λ as the wavelength inside the medium and ν as the frequency. Introducing eq.(2.17) in the wave equation (2.15), we obtain

$$k^2 = \omega^2\mu\epsilon \tag{2.19}$$

which is the *dispersion equation* for isotropic medium. For any wave that propagates as $\exp\{j(\mathbf{k}\cdot\mathbf{r}-\omega t)\}$ (harmonic wave), the surface of constant phase (wavefronts) satisfies

$$\mathbf{k}\cdot\mathbf{r} - \omega t = const. \tag{2.20}$$

Then, the surfaces of constant phase travel in the direction of $\mathbf{k}$ with a velocity whose magnitude is

$$\upsilon = \frac{\omega}{k} = \frac{1}{\sqrt{\mu\epsilon}} \tag{2.21}$$

Note that the phase velocity is a characteristic of the medium expressed in terms of ϵ and μ. The phase velocity of the electromagnetic radiation in vacuum is

$$c = \frac{1}{\sqrt{\mu_0\epsilon_0}} = 2.99793\times10^8 m/s \tag{2.22}$$

McMaster University

and in a material media the phase velocity is defined as

$$\upsilon = \frac{c}{n} \tag{2.23}$$

where $n = \sqrt{\mu\epsilon/\mu_0\epsilon_0}$, is known as the *refractive index*. In general, transparent materials are non-magnetic and have a magnetic permeability μ_0. Then, $n = \sqrt{\epsilon/\epsilon_0}$ or simply

$$n = \sqrt{\epsilon_r} \tag{2.24}$$

Therefore, the dispersion relation can be expressed in a useful form as

$$k = \frac{\omega}{c} n \tag{2.25}$$

The absorption of light by an optical medium is quantified by the absorption coefficient α. This is defined as the fraction of power absorbed in a unit length of the medium [53]. Assuming a light beam propagates in the z-direction and the intensity at a position z is $I(z)$, then the decrease of intensity after it propagates a distance dz is given by:

$$dI = -\alpha I(z) dz \tag{2.26}$$

integrating equation (2.26) we obtain Beer's law:

$$I(z) = I_0 e^{-\alpha z} \tag{2.27}$$

McMaster University

where I_0 is the optical intensity at $z = 0$. The absorption coefficient is a strong function of frequency.

2.2 Reflection, Refraction and Fresnel's Equations in a Dielectric Interface

Maxwell's equations can be solved for a continuous medium; however, as a result of the abrupt change in index of refraction at the interface between two different dielectric materials, it is necessary to introduce the continuity relationships of the components of the electromagnetic field vectors at the dielectric boundary [26]. These continuity relationships are the *boundary conditions* obtained from the integral form of Maxwell's equations for a source free region, the conditions are

$$\hat{\mathbf{a}}_n \times (\mathbf{E}_1 - \mathbf{E}_2) = 0 \tag{2.28}$$

$$\hat{\mathbf{a}}_n \times (\mathbf{H}_1 - \mathbf{H}_2) = 0 \tag{2.29}$$

$$\hat{\mathbf{a}}_n \cdot (\mathbf{B}_1 - \mathbf{B}_2) = 0 \tag{2.30}$$

$$\hat{\mathbf{a}}_n \cdot (\mathbf{D}_1 - \mathbf{D}_2) = 0 \tag{2.31}$$

where $\hat{\mathbf{a}}_n$ is the unit vector normal to the surface and the indices denote the dielectric materials at the interface. Therefore, the tangential components of $\mathbf{E}$ and $\mathbf{H}$, and the normal components of $\mathbf{D}$ and $\mathbf{B}$ are continuous across the interface separating media 1 and 2. With the general form of $\mathbf{E}$ as in equation (2.17), Maxwell's equations reduce to

McMaster University

$$\mathbf{k} \times \mathbf{E} = \omega\mu\mathbf{H} \tag{2.32}$$

$$\mathbf{k} \times \mathbf{H} = -\omega\epsilon\mathbf{E} \tag{2.33}$$

$$\mathbf{k} \cdot \mathbf{E} = 0 \tag{2.34}$$

$$\mathbf{k} \cdot \mathbf{H} = 0 \tag{2.35}$$

showing that **E**, **H** and **k** are mutually perpendicular.

Consider an incident plane wave, expressed by equation (2.36), propagating in medium 1 with index of refraction n_1 and wave vector $\mathbf{k}_i$, incident upon an interface formed with the medium 2, characterized by an index of refraction n_2, for example Fig. 2.1.

$$\mathbf{E}_i = \mathbf{E}_{0i} \ \exp\Big\{ j(\mathbf{k}_i \cdot \mathbf{r} - \omega_i t) \Big\} \tag{2.36}$$

Let the reflected and transmitted electric fields be given by

$$\mathbf{E}_r = \mathbf{E}_{0r} \ \exp\Big\{ j(\mathbf{k}_r \cdot \mathbf{r} - \omega_r t) \Big\} \tag{2.37}$$

$$\mathbf{E}_t = \mathbf{E}_{0t} \ \exp\Big\{ j(\mathbf{k}_t \cdot \mathbf{r} - \omega_t t) \Big\} \tag{2.38}$$

with $\mathbf{k}_r$ and $\mathbf{k}_t$ as the corresponding wave vectors. The boundary conditions require that the tangential electric field should be continuous across the boundary. Thus,

McMaster University

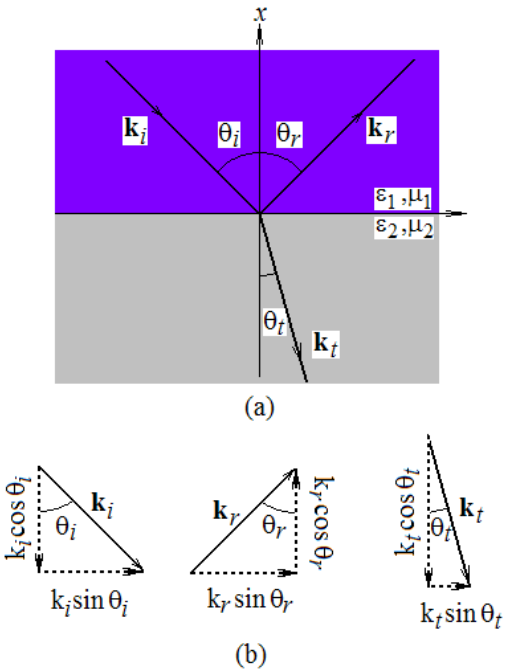

Figure 2.1: **Oblique incidence of a plane wave: (a) Illustration of the incident, reflected and transmitted wave with their respective angles, (b) Normal and tangential components of k**

$$\Big[\mathbf{E}_i(x=0)+\mathbf{E}_r(x=0)\Big]_{\tan}=\Big[\mathbf{E}_t(x=0)\Big]_{\tan} \tag{2.39}$$

thereby, the only way this boundary condition is satisfied is that

$$\omega_i=\omega_r=\omega_t=\omega \tag{2.40}$$

$$k_{iy}=k_{ry}=k_{ty}=k_y \tag{2.41}$$

$$k_{iz}=k_{rz}=k_{tz}=k_z \tag{2.42}$$

where equation (2.40) implies that the frequency does not change. Equations (2.41) and (2.42) are the *phase matching conditions*, which require that the tangential component of the propagation vectors be continuous. Therefore, the propagation vectors $\mathbf{k}_i$, $\mathbf{k}_r$ and $\mathbf{k}_t$ must lie in the plane of incidence (formed by the incident propagating vector and the normal to the surface vector). Thus,

$$k_i \sin\theta_i = k_r \sin\theta_r \tag{2.43}$$

$$k_i \sin\theta_i = k_t \sin\theta_t \tag{2.44}$$

where θ_r is *angle of refraction* and θ_t is *the angle of transmission*. Then,

$$k_i = \omega\sqrt{\mu_1\epsilon_1} = k_r \tag{2.45}$$

$$k_t = \omega\sqrt{\mu_2\epsilon_2} \tag{2.46}$$

from equations (2.43) and (2.45),

$$\theta_i = \theta_r \tag{2.47}$$

and from equations (2.44) and (2.46)

$$\frac{\sin\theta_t}{\sin\theta_i} = \frac{k_i}{k_t} = \sqrt{\frac{\mu_1\epsilon_1}{\mu_2\epsilon_2}} \tag{2.48}$$

McMaster University

using the equation (2.24) the expression (2.48) can be rearranged in a more convenient way

$$n_1 \sin\theta_i = n_2 \sin\theta_t \tag{2.49}$$

known as *Snell's law*.

This preliminary result for oblique incidence is used in two specific cases of the electric field polarization: TE (Transverse Electric) polarization or S-polarization, with the electric field perpendicular to the plane of incidence; and TM (Transverse Magnetic) polarization or P-polarization, with the magnetic field perpendicular to plane of incidence. Any other polarization may be consider as a linear combination of these two cases [54].

2.2.1 TE Polarization

The TE case is illustrated in Figure 2.2 where the electric field is perpendicular to the plane of incidence. After the direction of the propagation vector, $\mathbf{k}$, is chosen, the direction of the field vectors are depicted according to equations (2.32) to (2.35). Imposing the continuity conditions for the components E_y and H_z of the field vectors at the interface $x = 0$, leads to

$$E_{0i} + E_{0r} = E_{0t} \tag{2.50}$$

$$\sqrt{\frac{\epsilon_1}{\mu_1}} E_{0i} \cos\theta_i - \sqrt{\frac{\epsilon_1}{\mu_1}} E_{0r} \cos\theta_i = \sqrt{\frac{\epsilon_2}{\mu_2}} E_{0t} \cos\theta_t \tag{2.51}$$

McMaster University

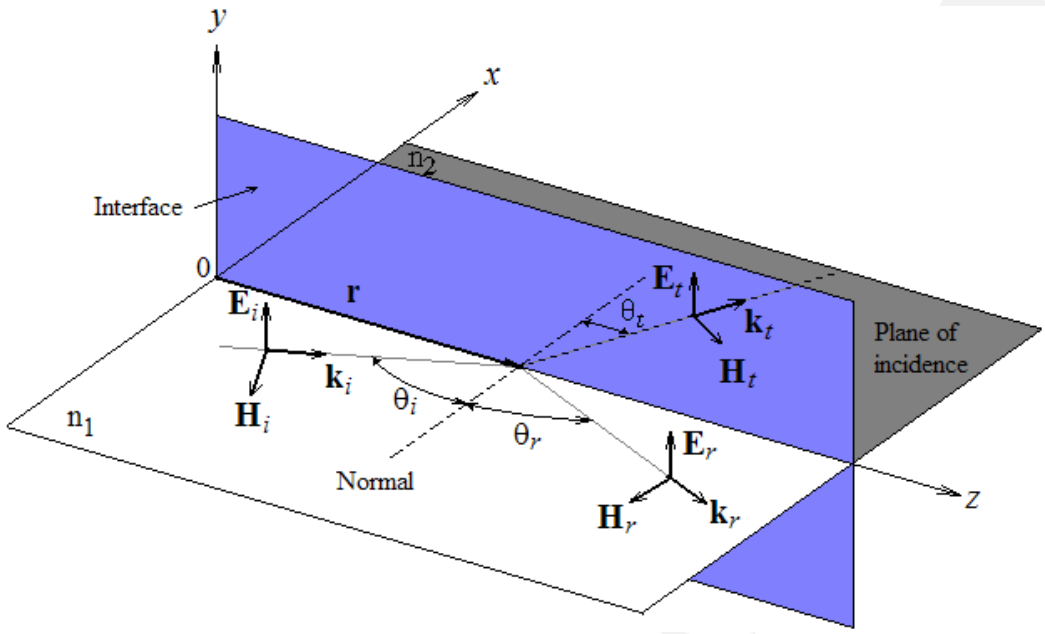

Figure 2.2: **Oblique incidence for TE polarization**

Assuming that the light is incident from medium 1, the *reflection* and *transmission coefficients* are given for a single interface as

$$r_{TE} = \frac{E_{0r}}{E_{0i}} \tag{2.52}$$

$$t_{TE} = \frac{E_{0t}}{E_{0i}} \tag{2.53}$$

From the boundary conditions we obtain

$$r_{TE} = \frac{n_1 \cos\theta_i - n_2 \cos\theta_t}{n_1 \cos\theta_i + n_2 \cos\theta_t} \tag{2.54}$$

$$t_{TE} = \frac{2n_1 \cos\theta_t}{n_1 \cos\theta_i + n_2 \cos\theta_t} \tag{2.55}$$

where $\mu_1 = \mu_2$ was assumed.

2.2.2 TM Polarization

For the TM case the magnetic field is perpendicular to the plane of incidence, illustrated in figure 2.3. The direction of the field vectors satisfy equations (2.32) to (2.35). The tangential components of **E** and **H** are continuous at the boundary $x = 0$, then

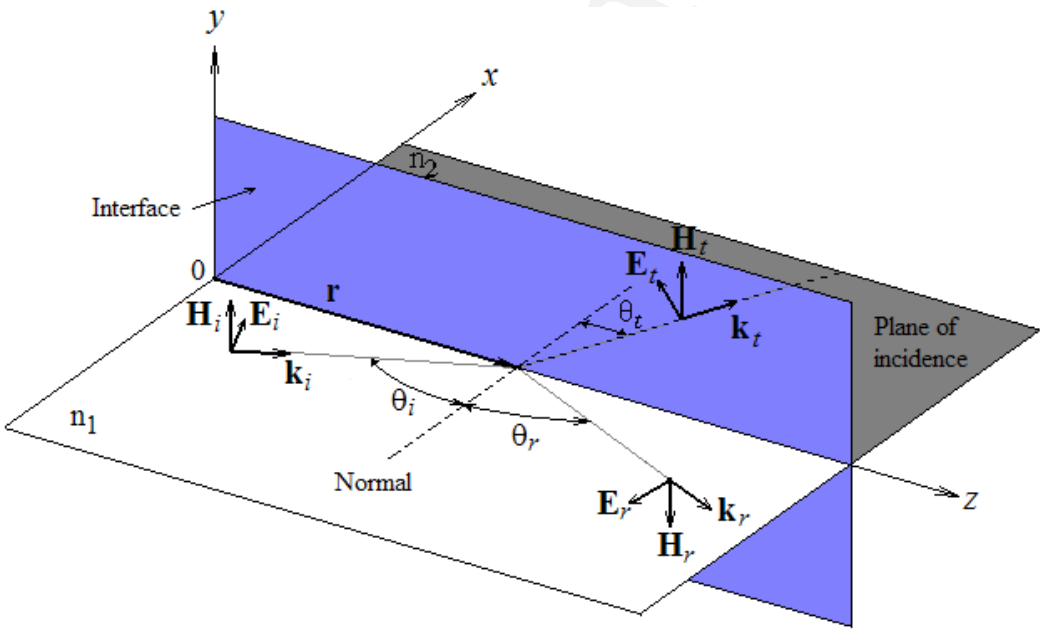

Figure 2.3: **Oblique incidence for TM polarization**

$$\sqrt{\frac{\epsilon_1}{\mu_1}}E_{0i} - \sqrt{\frac{\epsilon_1}{\mu_1}}E_{0r} = \sqrt{\frac{\epsilon_2}{\mu_2}}E_{0t} \tag{2.56}$$

$$(E_{0i} + E_{0r})\cos\theta_i = E_{0t}\cos\theta_t \tag{2.57}$$

The corresponding *reflection* and *transmission coefficients* are

$$r_{TM} = \frac{n_1 \cos\theta_t - n_2 \cos\theta_i}{n_1 \cos\theta_t + n_2 \cos\theta_i} \tag{2.58}$$

$$t_{TM} = \frac{2n_1 \cos\theta_i}{n_1 \cos\theta_t + n_2 \cos\theta_i} \tag{2.59}$$

where $\mu_1 = \mu_2$, which is generally the case for transparent materials.

2.2.3 Total Internal Reflection

The phenomenon of reflection can be classified for two types depending on the optical properties of the material in which the light travels. If the light is traveling in a low density material, with an index of refraction lower than that of the material that it encounters (*i.e.* is reflected from), the reflection is defined as *external reflection* but if the light is traveling in the high index material, it is known as *internal reflection*. In the case of internal reflection there is a particular situation known as *total internal reflection*. It occurs when the angle of incidence θ_i exceeds the critical angle, defined as

$$\theta_c = \sin^{-1}\frac{n_2}{n_1} \tag{2.60}$$

when $\theta_i > \theta_c$ a plane wave is totally reflected with no power flowing into the less dense material, equation (2.61). The electric and magnetic fields do, however, penetrate into the lower index of refraction material, with their amplitudes decreasing exponentially away from the surface [46] as described by the complex relationship

McMaster University

$$\cos\theta_t = -j\left[\left(\frac{\sin\theta_i}{\sin\theta_c}\right)^2 - 1\right]^{1/2} \tag{2.61}$$

The negative sign ensures that the transmitted wave decays exponentially as x approaches -∞. Then the reflection coefficients (2.54) and (2.58) become

$$r_{TE} = \frac{n_1\cos\theta_i + jn_2\sqrt{\left(\frac{\sin\theta_i}{\sin\theta_c}\right)^2 - 1}}{n_1\cos\theta_i - jn_2\sqrt{\left(\frac{\sin\theta_i}{\sin\theta_c}\right)^2 - 1}} \tag{2.62}$$

$$r_{TM} = \frac{-jn_1\sqrt{\left(\frac{\sin\theta_i}{\sin\theta_c}\right)^2 - 1} - n_2\cos\theta_i}{-jn_1\sqrt{\left(\frac{\sin\theta_i}{\sin\theta_c}\right)^2 - 1} + n_2\cos\ \theta_i} \tag{2.63}$$

It is noted that these reflection coefficients become complex numbers, which can be represented in their complex polar form as $r = |\rho|\exp(j\phi)$ where ϕ is the change of phase upon total internal reflection[1].

Since all the light energy is totally reflected by the surface, these two reflection coefficients have unit amplitude, that is $|r_{TE}| = |r_{TM}| = 1$. Then,

$$\phi_{TE} = 2\ \tan^{-1}\left(\frac{\sin^2\theta_i - \sin^2\theta_c}{1 - \sin^2\theta_i}\right)^{1/2} \tag{2.64}$$

$$\phi_{TM} = 2\ \tan^{-1}\left[\left(\frac{n_1}{n_2}\right)^2\left(\frac{\sin^2\theta_i - \sin^2\theta_c}{1 - \sin^2\theta_i}\right)^{1/2}\right] \tag{2.65}$$

Total internal reflection is the basis for dielectric waveguiding.

[1] $\rho = a + jb$ and $|\rho| = \sqrt{a^2 + b^2}$ and $\phi = \tan(b/a)$

McMaster University

2.3 Dielectric Waveguides

A waveguide should be able to confine and guide electromagnetic radiation along the guiding structure, therefore, the simplest optical waveguide structure is a dielectric slab, for example, a piece of glass surrounded by air. The region where the light is confined and guided is known as the guiding layer (or core) and is characterized by having a higher index of refraction than the surrounding medium.

In order to understand the concept of guiding modes an analysis of the *asymmetric slab waveguide* structure is a useful starting point.

The index of refraction profile associated with an asymmetric waveguide, such as the one shown in figure 2.4, is described by eq.(2.66)

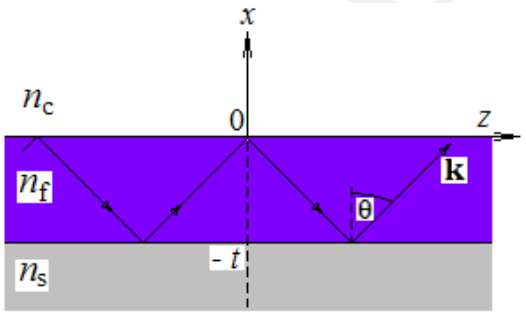

Figure 2.4: **Asymmetric slab waveguide index profile**

$$n(x) = \begin{cases} n_c, & 0 < x, \\ n_f, & -t < x < 0, \\ n_s, & x < -t, \end{cases} \tag{2.66}$$

where $n_c < n_s < n_f$ and t is the thickness of the guiding layer.

The solutions to the wave equation for monochromatic radiation propagating along

the z direction, in an homogeneous medium, are plane waves, described by

$$\mathbf{E}(\mathbf{r},t) = \mathbf{E}_0 \ \exp\Big\{j\left(\beta z \pm k_x x - \omega t\right)\Big\} = \mathbf{E}_m(x) \ \exp\Big\{j\left(\beta z - \omega t\right)\Big\} \tag{2.67}$$

$$\mathbf{H}(\mathbf{r},t) = \mathbf{H}_0 \ \exp\Big\{j\left(\beta z \pm k_x x - \omega t\right)\Big\} = \mathbf{H}_m(x) \ \exp\Big\{j\left(\beta z - \omega t\right)\Big\} \tag{2.68}$$

where $\beta = ksin\ \theta_i$ is the z component of the wave vector and it is known as the *propagation vector*. It determines whether the field varies with x sinusoidally or exponentially. $\mathbf{E}_m(x)$ and $\mathbf{H}_m(x)$ are the wavefuntions of the guided modes, and the subscript m is the *mode number*. This means that not all k_x values are allowed, and only a discrete set of solutions, called *modes of propagation*, exist for k_x. Substituting equation (2.67) in the wave equation (2.15), and equation (2.68) in equation (2.16), leads us to

$$\left[\frac{d^2}{dx^2} + \left(\frac{\omega}{c}n\right)^2 - \beta^2\right]\mathbf{E}_m(x) = 0 \tag{2.69}$$

$$\left[n^2\frac{d}{dx}\left(\frac{1}{n^2}\frac{d}{dx}\right) + \left(\frac{\omega}{c}n\right)^2 - \beta^2\right]\mathbf{H}_m(x) = 0 \tag{2.70}$$

where the TE and TM modes satisfy equation (2.69) and equation (2.70) respectively. These equations are solved separately for each layer of the waveguide structure such that they match the tangential components of the field vectors at each interface. Additionally, for guided modes the field amplitude vanishes at infinity. A guided mode requires that $n_s(\omega/c) < \beta < n_c(\omega/c)$ giving a sinusoidal solution in the guiding layer $(-t < x < 0)$, but exponential in the cover and substrate layers.

McMaster University

2.3.1 Guided TE Modes

For TE modes the polarization direction of the electric field is perpendicular to the plane of incidence, which according to Figure 2.4 is along the y direction. Then, E_y is the only component of the electric field vector, and the components of the magnetic field are H_x and H_z. Based on the previous description, the electric and magnetic fields are

$$E_y(x,z,t) = E_m(x)\ \exp\Big\{j\,(\beta z - \omega t)\Big\} \tag{2.71}$$

$$H_x(x,z,t) = \frac{\beta}{\mu\omega}E_m(x)\ \exp\Big\{j\,(\beta z - \omega t)\Big\} \tag{2.72}$$

$$H_z(x,z,t) = -\frac{j}{\mu\omega}\frac{\partial E_y}{\partial x} = -\frac{j}{\mu\omega}\frac{\partial E_m(x)}{\partial x}\exp\Big\{j(\beta z - \omega t)\Big\} \tag{2.73}$$

where $\mathrm{E}_m(x)$ is the wave function of the mth mode, and takes the following form

$$E_m(x) = \begin{cases} A\ \exp(-qx), & 0 \le x, \\ A\left[\cos(hx) - \dfrac{q}{h}\sin(hx)\right], & -t \le x \le 0, \\ A\left[\cos(ht) + \dfrac{q}{h}\sin(ht)\right]\exp\Big[p(x+t)\Big], & x \le -t, \end{cases} \tag{2.74}$$

where A is the normalization constant and h, q and p are given by

$$h = \left[\left(\frac{n_f\omega}{c}\right)^2 - \beta^2\right]^{1/2} \tag{2.75}$$

McMaster University

$$p = \left[\beta^2 - \left(\frac{n_c\omega}{c}\right)^2\right]^{1/2} \tag{2.76}$$

$$q = \left[\beta^2 - \left(\frac{n_s\omega}{c}\right)^2\right]^{1/2} \tag{2.77}$$

These relationships are obtained by substituting equation (2.74) in the expression (2.67).

Using the boundary conditions in the equation (2.73) at $x = -t$ we get the so called *mode condition* as,

$$\tan\Big(ht\Big) = \frac{p+q}{h\left[1 - \dfrac{pq}{h^2}\right]} \tag{2.78}$$

The propagation constant, β, for a guided TE mode must satisfy this condition.[2]

Once the propagation constant is obtained, the electric field distribution given by equation (2.74) is determined except for the constant A which can be defined with knowledge of the propagating optical power. This power P is expressed by

$$S_z = \frac{1}{2}\int \mathbf{Re}\Big\{\mathbf{E}\times\mathbf{H}^*\Big\}_z\, dx = P \tag{2.80}$$

or

$$\frac{\beta_m}{2\omega\mu}\int_{-\infty}^{\infty}\Big[E_m(x)\Big]^2 dx = P_m \tag{2.81}$$

[2]The equation (2.78) can be expressed as

$$-2ht + 2\tan^{-1}\frac{q}{h} + 2\tan^{-1}\frac{p}{h} = -2m\pi \tag{2.79}$$

McMaster University

where the subindex m denotes the mth confined TE mode. Substitution of equation (2.74) in equation (2.81) leads to

$$A_m = 2h_m \left(\frac{\omega \mu P}{\beta_m \left[t + \left(\frac{1}{q_m} \right) + \left(\frac{1}{p_m} \right) \right] (h_m^2 + q_m^2)} \right)^{1/2} \tag{2.82}$$

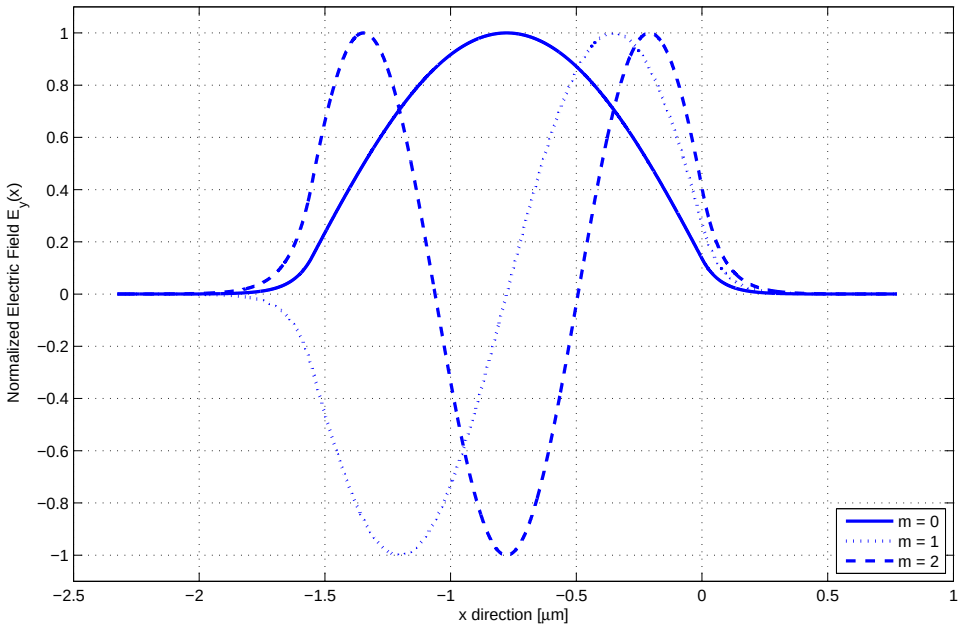

Figure 2.5: **Field distribution of the TE modes of a waveguide with $\mathbf{n}_c = 1$, $\mathbf{n}_f = 3.5$, $\mathbf{n}_s = 1.5$, and $t/\lambda = 1.0$.**

2.3.2 Guided TM Modes

For TM modes, the magnetic field is perpendicular to the plane of incidence, which according to figure 2.4 is along the y direction. Then, H_y is the only component of

the magnetic field vector, and the components of the electric field are E_x and E_z. Based on the previous description the magnetic and electric fields are

$$H_y(x,z,t) = H_m(x)\ \exp\Big\{j(\beta z - \omega t)\Big\} \tag{2.83}$$

$$E_x(x,z,t) = \frac{j}{\omega\epsilon}\frac{\partial H_y}{\partial z} = \frac{\beta}{\omega\epsilon}H_m(x)\ \exp\Big\{j(\beta z - \omega t)\Big\} \tag{2.84}$$

$$E_z(x,z,t) = -\frac{j}{\omega\epsilon}\frac{\partial H_y}{\partial z} \tag{2.85}$$

The function $H_m(x)$ takes the following form in each region:

$$H_m(x) = \begin{cases} B\ exp(-qx), & 0 \le x, \\ B\left[cos(hx) - \dfrac{\bar{q}}{h}sin(hx)\right], & -t \le x \le 0, \\ B\left[cos(ht) + \dfrac{\bar{q}}{h}sin(ht)\right]\exp\Big[p(x+t)\Big], & x \le -t, \end{cases} \tag{2.86}$$

where B is the normalization constant and h, q and p where defined previously in equations (2.75), (2.76) and (2.77) respectively and $\bar{q}$ is defined as follows

$$\bar{q} = \frac{n_f^2}{n_c^2}q \tag{2.87}$$

and the *mode condition*[3] for the TM modes is

[3]The equation (2.89) can be expressed as

$$-2ht + 2\tan^{-1}\frac{n_f^2 q}{n_c^2 h} + 2\tan^{-1}\frac{n_f^2 p}{n_s^2 h} = -2m\pi \tag{2.88}$$

McMaster University

$$\tan\Big(ht\Big) = \frac{h\big(\bar{p}+\bar{q}\big)}{h^2-\bar{p}\bar{q}} \tag{2.89}$$

where

$$\bar{p} = \frac{n_f^2}{n_s^2}p \tag{2.90}$$

The normalization constant B is calculated in a similar way as A. Thus, we have

$$\frac{1}{2}\int_{-\infty}^{\infty} H_y E_x^*\,dx = \frac{\beta}{2\omega}\int_{-\infty}^{\infty}\frac{H_m^2(x)}{\epsilon(x)}\,dx \tag{2.91}$$

or

$$\int_{-\infty}^{\infty}\frac{\Big[H_m(x)\Big]^2}{n^2(x)}\,dx = \frac{2\omega\epsilon_0}{|\beta_m|} \tag{2.92}$$

where $n^2(x) = \epsilon(x)/\epsilon_0$, and using equation (2.86) gives

$$B_m = 2\sqrt{\frac{\omega\epsilon_0}{|\beta_m|\,t_{eff}}} \tag{2.93}$$

where

$$t_{eff} \equiv \frac{\bar{q}^2+h^2}{\bar{q}^2}\left(\frac{t}{n_f^2}+\frac{q^2+h^2}{\bar{q}^2+h^2}\frac{1}{n_c^2 q}+\frac{p^2+h^2}{\bar{p}^2+h^2}\frac{1}{n_s^2 p}\right) \tag{2.94}$$

McMaster University

2.3.3 Single Mode Condition for The Planar Waveguide

To describe and compare the confined modes, it is necessary to define the normalized propagation constant, often called *the effective index of refraction of the mode* [41]

$$N_{eff} = \frac{\beta}{\omega/c} = n \sin\theta \tag{2.95}$$

The dependence of the propagation constant β on the normalized slab thickness (t/λ) for $n_f = 3.5$, $n_s = 1.5$ and $n_c = 1.0$ is shown in figure 2.6. In this plot only the allowed modes are shown for a slab waveguide with a thickness equal to the wavelength. In order to confine uniquely the fundamental modes for TE and TM polarization, a waveguide with a thickness of 0.15λ is required.

In order to calculate the total number of confined modes that can be supported by a waveguide, the normalization coefficients defined by H. Kogelnik from reference [43] are used. These coefficients are the normalization frequency V, the normalized guided index b, and the asymmetry coefficient a. They are defined respectively by

$$V \equiv \frac{2\pi t}{\lambda}\sqrt{n_f^2 - n_s^2} \tag{2.96}$$

$$b \equiv \frac{N_{eff}^2 - n_s^2}{n_f^2 - n_s^2} \tag{2.97}$$

$$a \equiv \frac{n_s^2 - n_c^2}{n_f^2 - n_s^2} \tag{2.98}$$

Substituting these coefficients into equation (2.79) for the TE modes, the dispersion equation can be expressed as

McMaster University

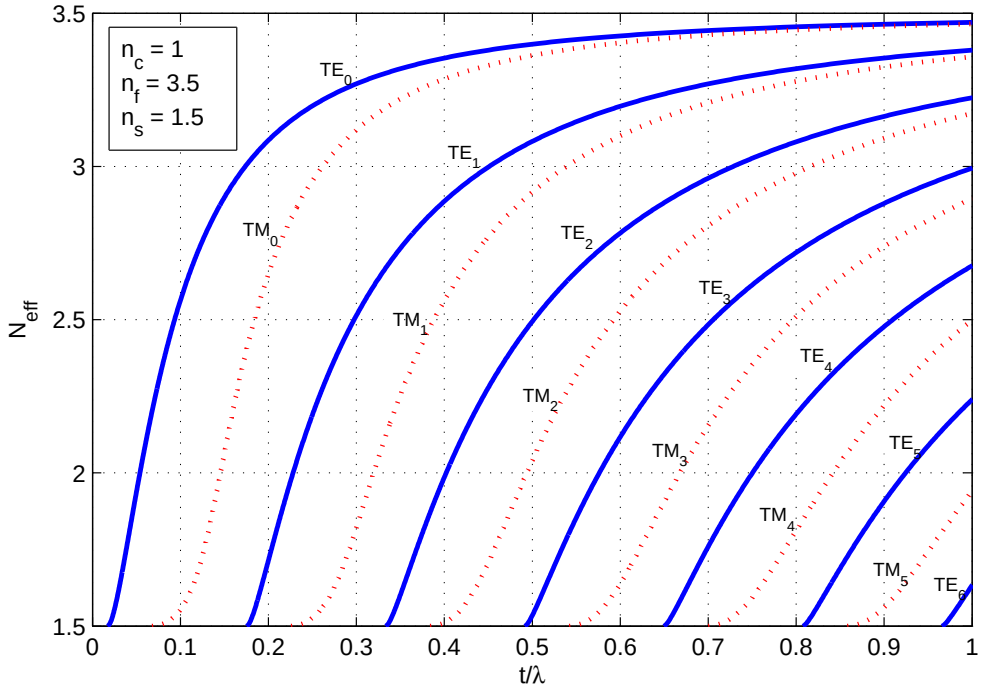

Figure 2.6: **Dispersion curves for the confined modes of c-Si film on SiO_2 substrate**

$$V\sqrt{1-b} = m\pi + \tan^{-1}\left[\sqrt{\frac{b}{1-b}}\right] + \tan^{-1}\left[\sqrt{\frac{b+a}{1-b}}\right] \tag{2.99}$$

The cut-off frequency of the mth mode is calculated when $b = 0$, then

$$V_m = m\pi + \tan^{-1}\left[\sqrt{a}\right] \tag{2.100}$$

and using equation (2.96) and equation (2.98), it is possible to obtain an approximate formula for the number of guided modes, expressed by

$$m = \frac{2t}{\lambda}\sqrt{n_f^2 - n_s^2} \tag{2.101}$$

The value obtained for m is increased to the nearest integer [55] which corresponds to the approximate number of modes.

For TM modes a similar procedure is followed with the exception of the asymmetric coefficient definition, which for this case is given by

$$a \equiv \frac{n_f^4}{n_c^4}\frac{n_s^2 - n_c^2}{n_f^2 - n_s^2} \tag{2.102}$$

2.4 3-D Optical Waveguides

In the previous section the concept of *guided modes* was introduced using the slab waveguide, which is a simple but useful structure to visualize and understand the concept of light confinement and propagation. However, the slab waveguide (2-D waveguide) lacks practical application since it only allows the confinement of light in the x direction, while it is free to spread out in the y direction. In practice, more complicated structures are used in optical integrated circuits to confine the light in both transverse directions. These types of structures are referred to as a three-dimensional (3-D) structure because a variation in the field distribution occurs in three dimensions rather than two [46]. Examples of 3-D waveguide structures are the rectangle waveguide, ridge waveguide and trapezoidal rib waveguide. In a 3-D dielectric waveguide, pure TE and TM modes are not supported and two families of *hybrid modes* exist [45].

The use of numerical methods, such as the finite element method and finite difference method, are often required in order to analyze the supported modes of 3-D

McMaster University

waveguide structures, although the analytical procedure (*Effective Index Method*) described below is extremely useful in certain restricted cases.

2.5 Effective Index Method

The effective index method is an analytical method based on the concept of the effective index of the guided mode [45]. It is applicable to complicated waveguide structures, such as ridge, buried channel and diffused waveguides [47], where approximate solutions of the propagation constants are sufficient.

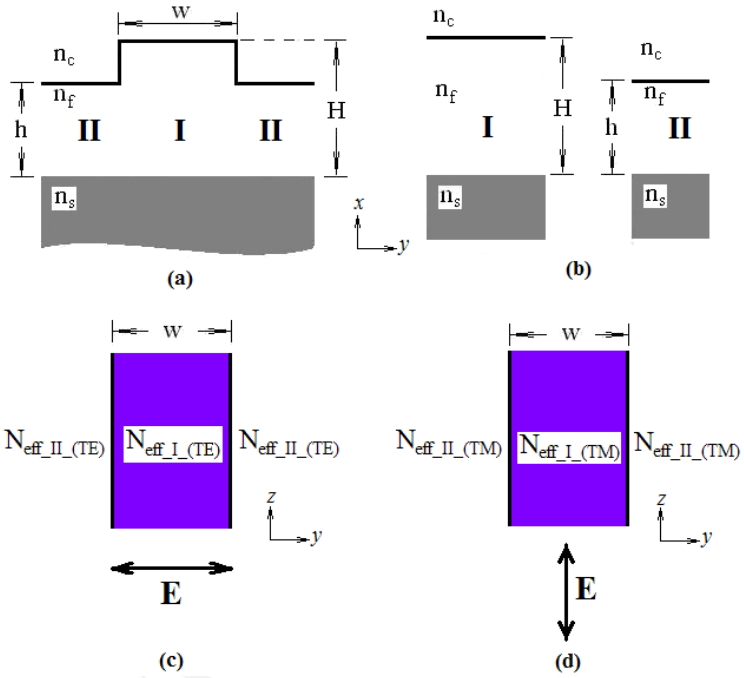

Figure 2.7: **a) Ridge waveguide structure, b) decomposition of the ridge waveguide in two sections showing the vertical distribution of the indices of refraction and thickness, c) virtual slab waveguide for TE modes, d) virtual slab for TM modes**

In general, with this method, the solutions for modes confined in a 3-D ridge waveguide can be solved for in terms of two slab waveguides; one with vertical light confinement and the other with horizontal light confinement. In the ridge waveguide the light is confined in the vertical direction by the difference in index of refraction of the guiding layer with respect to the cladding and substrate layers, and in the lateral direction by a step in the guiding layer thickness between the centre and the outer regions [56]. The first step in using the *Effective Index Method* is dividing the ridge waveguide into two regions, the centre region identified by the number **I** and the outer regions labeled as **II**, figure 2.7.*a*. The TE effective index for each region and for each polarization is then calculated (as described by Figure 2.7.*b*) to form a virtual slab waveguide of thickness w. It is noted that the polarization direction of the electric field is now perpendicular to the boundaries of this virtual slab waveguide. Thus, the symmetrical TM eigenvalue equation is used in order to calculate the equivalent effective index for this virtual slab structure. Similar procedure is followed to calculate the propagation constant of the TM modes. First, the asymmetrical TM eigenvalue equation is used to obtain the effective index values for the virtual slab waveguide from figure 2.7.*d*. As the polarization of the electric field is now parallel to the boundaries of the virtual slab waveguide the symmetrical TE eigenvalue equation is used to calculate the equivalent effective index for the TM modes. For a more detailed description of the Effective Index Method, the reader is referred to the numerical example presented in pages 61-63 of reference [17].

2.6 Single Mode Condition Of 3-D Waveguides

In a waveguide structure the single-mode propagation condition for electromagnetic radiation depends on the geometry and dimension ratio of the waveguide, the

McMaster University

indices of refraction of the materials used and the polarization state of the light. The structure used throughout this study is a ridge waveguide, figure 2.8, and in the present section the dimension ratio that fulfills the single-mode condition will be discussed.

The advantage of using a single-mode ridge waveguide resides in the fact that the waveguide cross-section area can be of several square microns instead of the sub-micron dimensions required for the single-mode-slab condition. This large cross section not only implies an easier manufacturing tolerance but also a better coupling efficiency to single mode fibers [57]. In addition, single-mode propagation is desired to ensure a perfect matching of the amplitude profiles in integrated devices which require the control of optical phase.

The single-mode ridge waveguide condition for a large cross-section (here defined as $>1\mu\text{m}^2$) was originally proposed by Petermann [19, 58] using a mode-matching technique. Later, Soref, *et al* [59] presented it in an empirical, normalized form given by

$$t < 0.3 + \frac{r}{(1-r^2)^{\frac{1}{2}}} \tag{2.103}$$

with

$$t = \frac{w}{H}, \tag{2.104}$$

and

$$r = \frac{h}{H} \geq 0.5 \tag{2.105}$$

McMaster University

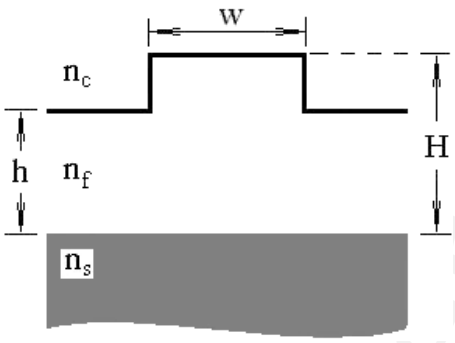

Figure 2.8: **Scheme of a ridge waveguide and its dimensions**

In eqs.(2.103-2.105), H is the ridge height, w is the ridge width and h the slab height, as shown in figure 2.8. For large cross-section ridge waveguides the mode size is much larger than the wavelength. Therefore, both polarizations (TE and TM) present very similar behavior and equation (2.103) can be applied to either.

A "corrected" and more restrictive condition using the Effective Index Method (EIM) was proposed by Pogossian *et al.* [60]. The only difference in the empirical expression was the elimination of the constant 0.3 from equation (2.103). They concluded this study by comparing both equations against experimental values reported by Rickman *et al.* [61], Figure 2.9. One may ask which is the best in practice? Different numerical studies were developed in order to compare these empirical models. One of these was conducted by *Olly Power* [62, 63] using the Beam Propagation Method (BPM), which concluded that the formula presented by *Soref et al.* is the most accurate for determining single-mode propagation. In an independent study developed by *Timo Aalto et al.* [64] it is shown that the single-mode behavior is observed according to the prediction of *Soref*; however, it is noted that a slight polarization dependence exist besides a small geometrical birefringence that is emphasized as the thickness of the waveguide is reduced. On the other hand, a finite element

analysis suggested that the *Soref* formula is more accurate for lower values of r, while Pogossian's approach fits better for high values of r [65]. Or as *J. Lousteau et al.* [66] describes, equations (2.103) and (2.104) are not sufficient to ensure effective single-mode operation, because these conditions were established for the case in which the first order mode will not propagate due to lateral leakage; however, nothing was said about higher order modes which may be guided with low loss. In any case, seeking values for t and r far from the multimode region and using the data reported in reference [66] plus numerical simulations with available commercial software is in general sufficient to ensure single-mode propagation.

In order to explain why a ridge waveguide can be single-mode for large transverse dimension it is necessary to divide the ridge waveguide structure into two regions, the central or ridge region and the side or slab region of the waveguide. The condition presented in equation (2.103) eliminates the higher order horizontal modes. It means that the effective index of any higher horizontal mode in the ridge region is lower than the effective index of the fundamental mode in the slab region. This negative difference of effective index in the central region produces a leakage of the higher order horizontal modes to the surrounding slab waveguide. On the other hand, to prevent the propagation of higher order vertical modes, the condition $r \geq 0.5$ needs to be satisfied. This assures that any mode with two or more maxima in the vertical direction is always radiated into the slab region because the bottom maxima will couple to the fundamental mode of the surrounding slab region [59, 62].

2.7 Thermo-optic Effect

The attractiveness of the use of the thermo-optic effect in optical waveguide devices arises from the fact that it is present in practically all waveguide materials and

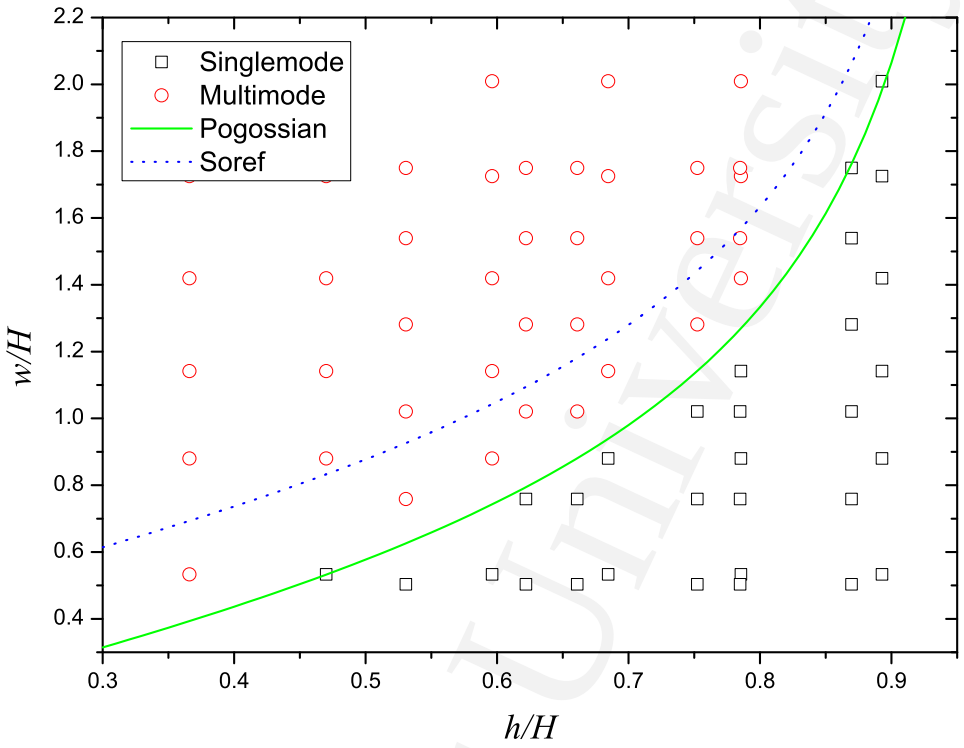

Figure 2.9: **Plots of the theoretical curves for the single mode. The circles and squares correspond to multimode and single-mode waveguides, respectively. Extracted from reference [60].**

mainly for the simplicity and flexibility that the effect offers [67]. First of all, it is necessary to understand what is happening in an optical material when the temperature changes. In order to do so, the main temperature-dependent material properties are identified, which are *size*, *refractive index*, *density* and *polarizability*. The macroscopic coefficients resulting from the material changes due to temperature variation are the thermal expansion coefficient, α_l, and the thermo-optic coefficient, dn/dT. The thermo-optic coefficient can be a positive or negative value, since the coefficient depends on the polarizability (tendency of electrons of a molecule to be deformed by

McMaster University

an applied electric field) and density of the particular material, which at the same time are temperature-dependent. The electronic *polarizability* is defined as the ratio of the induced dipole moment **p** of an atom to the electric field **E** that produces this dipole moment.

$$\mathbf{p} = \alpha_{pol}\mathbf{E} \tag{2.106}$$

The thermal expansion coefficient[4], α_l, indicates the degree to which a material expands upon heating. If the number of atoms or molecules remain constant it is obvious that the density of the material decreases as the volume increase as a result of heat. Then, the thermo-optic coefficient can be expressed as

$$\frac{dn}{dT} = \frac{1}{2\epsilon_0 n}\left(\alpha_{pol}\frac{dN}{dT} + N\frac{d\alpha_{pol}}{dT}\right) \tag{2.107}$$

where N is the number of dipole moment per unit volume (density). It is noted that the right hand side of the equation is divided into two terms, the first one is the density-dependent part representing the influence of particle density on polarizability, and the second one corresponds to the density-independent part representing the temperature dependence of the polarizability per particle [68]. Additionally, the first term in the right hand side is usually negative because the density tends to decrease as the temperature increases and the second term in the right hand side is usually positive since the polarizability tends to increase with a change in temperature, which implies that these two effects compete to determinate the actual behavior of the refractive index with the temperature. For silicon the thermo-optic coefficient is approximately $1.89\times10^{-4}K^{-1}$ [17].

[4]Which can be defined as $\alpha_l = (\frac{1}{l_0})(\frac{\Delta l}{\Delta T})$, where l_0 is the initial length.

McMaster University

2.8 Waveguide Losses

When light propagates through a waveguide it may experience some type of loss. In waveguide structures the losses are classified as coupling, propagation and radiation losses, which are generally attributed to three different mechanisms: *scattering*, *absorption* and *radiation* [69]. The following section describes some of these losses and introduce some analytical expressions used for their calculation.

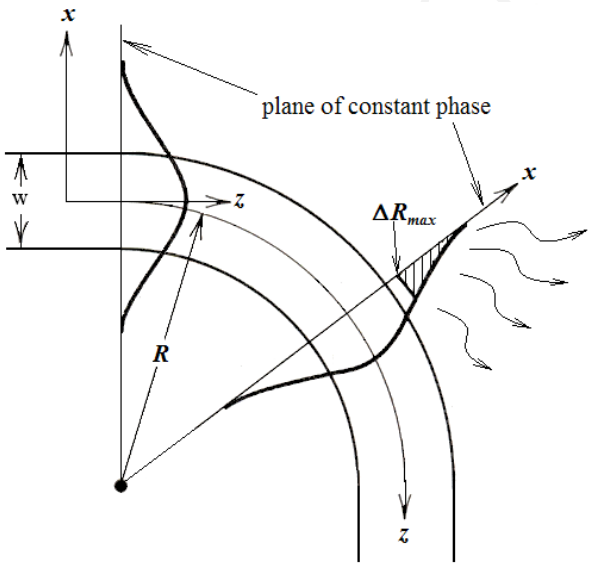

Figure 2.10: **A curved waveguide and the symbolic representation of bent loss [46].**

The integration of multiple non collinear dielectric waveguides into the same chip requires curved waveguides to interconnect them. The introduction of these curved waveguide sections induces bending and transition losses in addition to the loss mechanism encountered in a straight waveguide, *e.g.* propagation losses that for a SOI waveguide are typically in the range 0.1 - 0.5 dB/cm [17]. Bending loss is the continuous radiation of mode power tangentially out of a curved waveguide as light travels

through the bend [70]. Transition loss occurs at the junction of two waveguides having different radii of curvature [70]. Under the condition of single-mode propagation, a small part of the energy associated with the mode that is traveling through the waveguide is propagating outside of the waveguide core, whose profile decays exponentially with respect to distance from the waveguide axis. Close to the waveguide axis, the surface of constant phase, which tends to be perpendicular to the waveguide axis, moves with a velocity that is typical for the propagation for the particular mode in the straight waveguide [68]. It is noted that the tangential velocity of points on the surface of constant phase which are further from the centre of curvature is higher than those closer to the waveguide axis. However, because all these points lie in the same phase front they all have the same angular velocity. Then, their tangential velocity increases with R up to some point R_{max} where the velocity will exceed the velocity of light in the surrounding medium. This means, that the part of the mode outside of the waveguide core beyond the R_{max} cannot travel sufficiently quickly to stay in phase with the remainder of the guided mode and therefore must split away from the guide and radiate into the surrounding medium, Figure 2.10. Since this tail always exists, it is necessary for a continuous supply of energy to be provided from the rest of the guided mode as it travels around the bend implying a decrease of the mode amplitude with propagation [46].

The bending loss formula, presented here, is based on Marcuse's method [42] (other analytical models are the one presented by Lee [46] and by Marcatili [71]). The formula for bending loss is defined as

$$\alpha_{BL} = C_1 e^{-C_2 R} \tag{2.108}$$

where α_{BL} is the bending loss coefficient, R is the curvature radius and the constants

McMaster University

C_1 and C_2 have the values

$$C_1 = \frac{\alpha_x^2 \cdot k_{2x}^2}{k_0^3 N_{eff3}\left(N_{eff1}^2 - N_{eff2}^2\right)\left(1 + \alpha_x \frac{\mathrm{w}}{2}\right)} \cdot e^{\alpha_x \mathrm{w}} \tag{2.109}$$

$$C_2 = \frac{2\alpha_x^3}{3k_3^2} \tag{2.110}$$

with $\alpha_x = k_0\sqrt{N_{eff3}^2 - N_{eff2}^2}$, $k_2 x = k_0\sqrt{N_{eff1}^2 - N_{eff3}^2}$, $k_2 = N_{eff2}k_0$, N_{eff1} is the effective index of the rib section, N_{eff2} is the effective index of the slab section and N_{eff3} is the effective index of the slab-rib-slab section calculate using the effective index method (section 2.5).

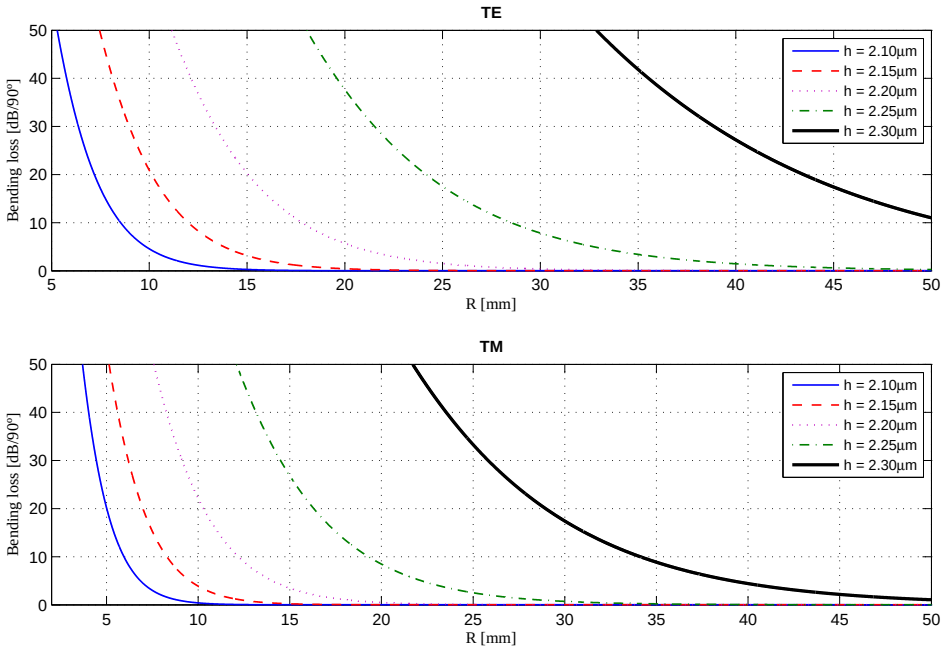

Figure 2.11: **Bending loss calculated with Marcuse's method for a waveguide with H = 2.5μm and w = 4μm.**

Transition loss can be described as the change in the mode shape when light is transferred between two waveguides with different curvature radii. For example, the shape of the mode in a straight waveguide is symmetric with respect the field peak which occurs at the centre of the waveguide. However, the mode shape in a curved waveguide is not symmetric, the peak is moved laterally from the waveguide centre further from the arc centre. This lateral displacement of the peak breaks the symmetry of the mode and its width with respect to the mode in the straight waveguide [70]. The transition loss calculation for the straight-to-curve transition was described using the approximation proposed by Subramanian

$$\eta_{sc} = \frac{\left[1 + \frac{\left(k_0 \cdot N_{eff1} \cdot \mathrm{w}_0\right)^2 a}{2R}\right]^2 e\left(-\frac{a^2}{2\mathrm{w}_0^2}\right)}{\left[1 + \frac{\left(k_0 \cdot N_{eff1} \cdot \omega_0\right)^4 \mathrm{w}_0^2}{2R^2}\right]} \tag{2.111}$$

where w_0 is the mode width and a the lateral offset; in this case $a = 0$. Figure 2.12 shows the transition loss for three different h values. It is noted that for less than 10mm radii transition loss can vary drastically, and for $R > 45$mm radii the transition losses are practically the same for all geometries.

The coupling of light between different optical elements introduces some loss of light commonly called *coupling loss*. Calculated here, as an example, is the reflection losses for an air-silicon interface for different incident angles and the coupling efficiency for a fiber-silicon waveguide connection.

The reflection loss may be calculated using the Fresnel equations [50] for the air-silicon interface. The results are presented in Figure 2.13. For normal incidence, $\sim$30% of the light is reflected which means $\sim$1.5dB of the power is lost per facet for both TE and TM polarization when light is coupled into a silicon waveguide.

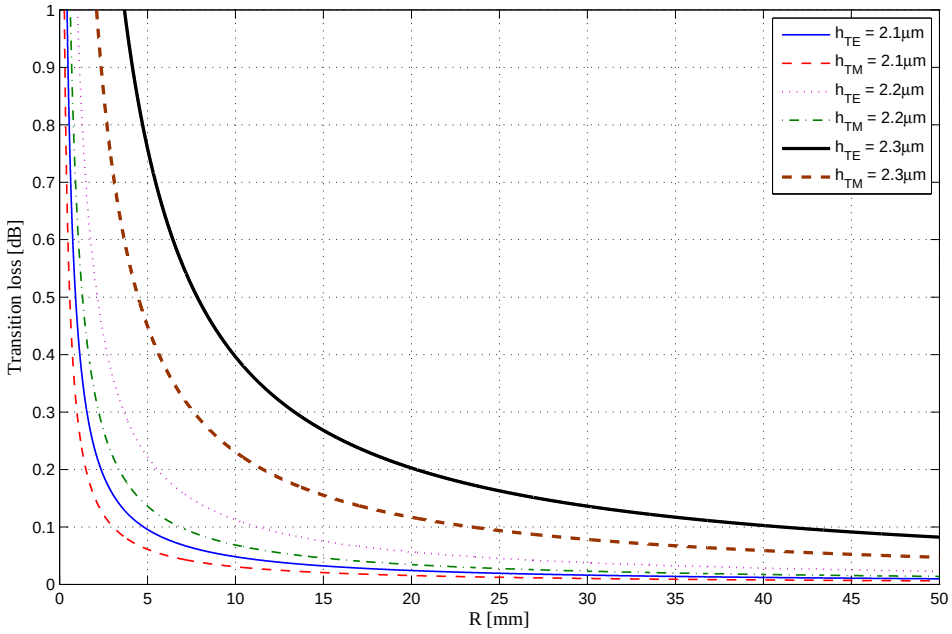

Figure 2.12: **Transition loss for a waveguide with H = 2.5μm and w = 4μm.**

However, it is observed that for TM polarization the reflections are reduced to zero for an angle of ∼74° (Brewster's angle). Above this angle, the reflections for TM polarization increase rapidly. On the contrary, reflection of light for TE polarization always increases as the incident angle increases.

Additional coupling loss between two waveguides, for example an optical fiber and a silicon ridge-waveguide, is found by calculating the overlap integral between the fiber optic field distribution and the waveguide field profile. This is a non-trivial task. However, assuming that both field profiles have a Gaussian distribution it is possible to use the analytical expression proposed by Shaodong Wu and Hans J. Frankena [72]

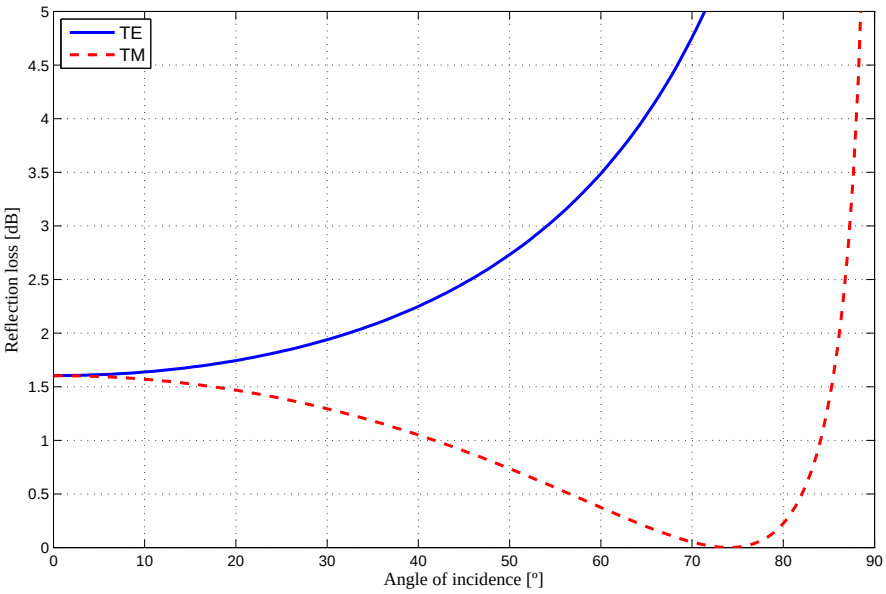

Figure 2.13: **Reflection losses for air-silicon interface for TE and TM polarization.**

$$\eta = \left(\frac{2w_1 w_2}{w_1^2 + w_2^2}\right) e^{\left(-\frac{2\delta^2}{w_1^2 + w_2^2}\right)} \tag{2.112}$$

where δ is the linear misalignment and w_1 is the beam waist for the fiber optic beam profile in the waveguide facet after it propagates through air a distance d, which is given by the formula

$$w_1^2 = w_0^2 \left[1 + \left(\frac{\lambda d}{\pi w_0^2}\right)^2\right] \tag{2.113}$$

with w_0 as the fiber's beam waist at the end of fiber optic, λ as the wavelength and w_2 is the beam waist for the mode in the waveguide, assuming single mode propagation,

shown in Figure 2.14.

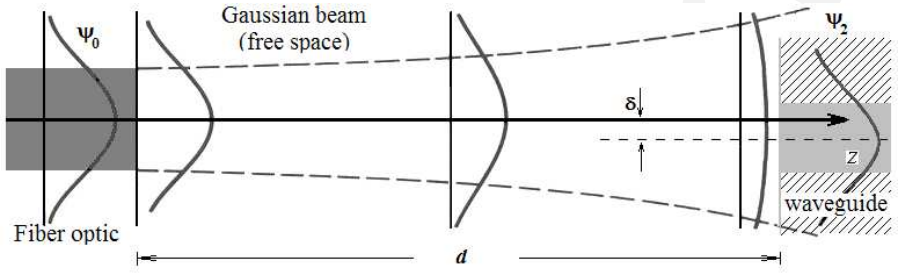

Figure 2.14: **Outline for the coupling efficiency, eagle eye view.**

Generally, the use of tapered optical fiber (in which the optical fiber diameter is reduced gradually up to a diameter similar to that of the waveguide cross sectional area) to couple light to the waveguide allows a better coupling efficiency. Figure 2.15(a) shows the coupling efficiency as a function of the distance between fiber and waveguide, assuming perfect alignment, for seven different fiber optic diameters. It is noted that if both the beam waist and the separation distant are small, the loss is minimized. Additionally, some loss calculations are described for a lateral misalignment of 0μm up to 2μm, the results are reported in figure 2.15(b) for a fiber diameter of 2.5μm.

2.9 Absorption

The absorption mechanisms in silicon are best explained by considering the interaction of its electrons and holes with the photons. For example, in silicon (an indirect bandgap semiconductor), photons with energy exceeding the bandgap energy E_g are absorbed, exciting electrons from the valence band to the conduction band (interband absorption) and forming electron-hole pairs, Figure 2.16(a). For photon energies less

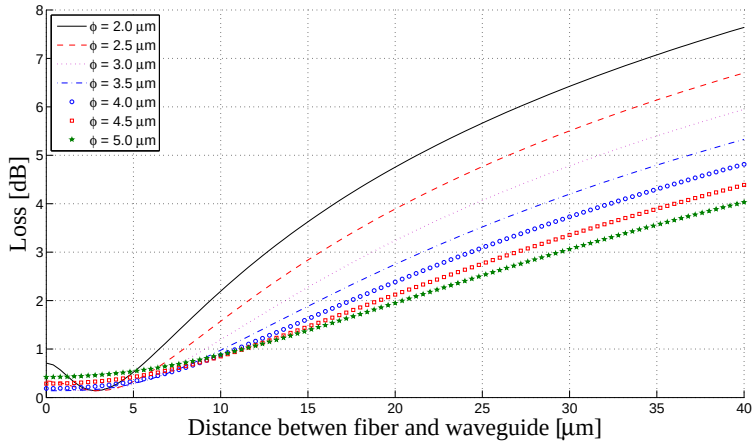

(a)

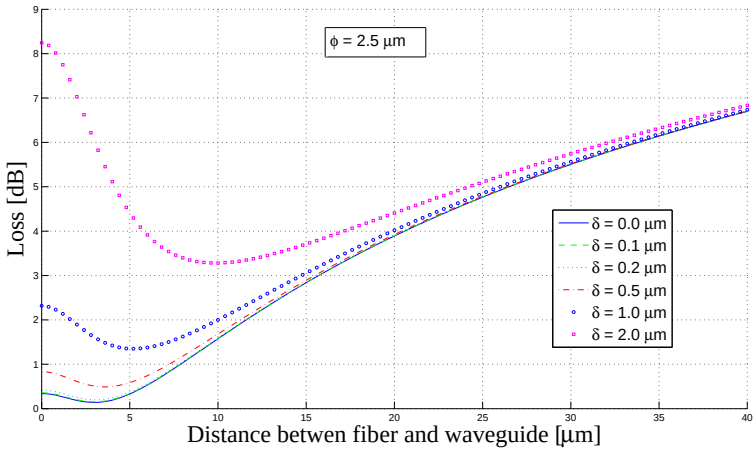

(b)

Figure 2.15: **Coupling efficiency (a) as function of distance d for seven different values of diameter ϕ, and (b) as a function of distance d for six different values of offset δ.**

than E_g, semiconductors are largely transparent, at least at moderate light intensities. Some photons are still absorbed by exciting electrons and holes within the conduction and valence bands to higher energies (free-carrier absorption —intraband absorption—). If the semiconductor is heavily doped with impurities that leads to

a large concentration of free carriers, the light beam can be fully absorbed, Figure 2.16(b). Absorption via carrier traps are associated with impurities or lattice defects having energy levels that lie within the energy bandgap but away from the band edges by several k_BT, which are usually referred to as deep-levels, Figure 2.16(c). For example, photons with energy[5] $E_T < h\nu < E_g$ can excite a carrier into a deep-level. After the capture of one type of carrier the deep-level can act as a trapping centre or as a recombination centre, either by re-exciting the carrier back to its original band without recombination taking place or by capturing the opposite type of carrier from the opposite band, respectively [27, 73, 74].

The refraction and absorption of an optical medium can be described by a single quantity called the complex refractive index, and is defined as:

$$\tilde{n} = n + j\kappa \tag{2.114}$$

where n is the real part of the complex refractive index, previously defined in eq.(2.23), κ is the imaginary part of $\tilde{n}$ and is called the extinction coefficient.

Optical attenuation is characterized by the Beer's law expression, eq.(2.27), where the absorption of light is quantified by the *absorption coefficient* of the material α. In order to determine the relationship between α and κ, consider the propagation of a plane wave, eq.(2.17), in the z-direction through a medium with a complex refractive index and the definition of the wave vector, eq.(2.26),

[5] E_T corresponds to the energy of the deep-level within the silicon bandgap and ν is the frequency of the photon that is being absorbed.

McMaster University

$$\begin{aligned} E(r,t) &= E_0 \exp\left[j(\tilde{n}\frac{\omega}{c}z - \omega t)\right] \\ &= E_0 \exp\left(-\kappa\frac{\omega}{c}z\right) \exp\left[j(n\frac{\omega}{c}z - \omega t)\right] \end{aligned} \tag{2.115}$$

It is noted that a non-zero extinction coefficient leads to an exponential decay of the wave in the medium. The optical power, or intensity, of the wave is proportional to the square of the electric field, $I \propto EE^*$, and comparing this result with Beer's law, eq.(2.27), it is concluded that

$$\alpha = \frac{2\kappa\omega}{c} = \frac{4\pi\kappa}{\lambda} \tag{2.116}$$

This suggest that α is directly proportional to the extinction coefficient and inversely proportional to wavelength.

Figure 2.17 shows that the experimentally determined silicon absorption coefficient varies over many orders of magnitude with varying wavelength λ. The continuous line corresponds to the absorption of intrinsic c-Si. It can be seen that α decreases strongly with increasing wavelength. Short-wavelength photons ($\lambda < 1.12\mu$m) have an energy larger than the (indirect) bandgap. These photons are able to create electron-hole pairs and are readily absorbed by the c-Si (*interband* absorption). However, long-wavelength photons ($\lambda > 1.12\mu$m) cannot generate electron-hole pairs and silicon is virtually transparent for these wavelengths.

Intrinsic silicon is a poor conductor, but the addition of doping reduces its resistivity. By adding n- or p-type doping to a semiconductor, *free electrons* or *holes* are introduced. These free charge carriers can absorb photons by free-carrier (*intraband*) absorption (but electron-hole pairs are not generated), as can be seen for the two

McMaster University

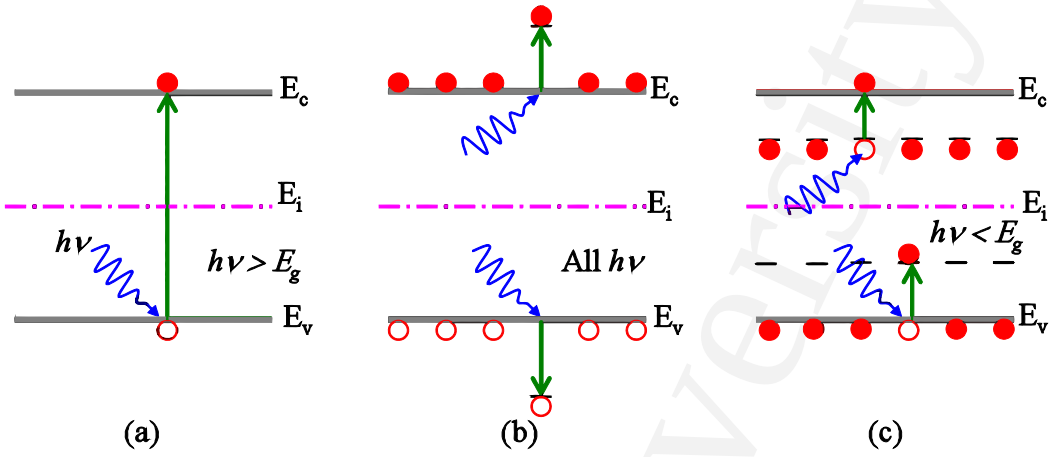

Figure 2.16: **Optical absorption via (a) band-to-band absorption (inter-band). (b) Free-carrier absorption (intraband), for n- and p-type materials (top and bottom scheme, respectively), and (c) Absorption via traps for n- and p-type material.**

doping cases presented in Figure 2.17. The use of free-charge carriers to engineer the optical properties of silicon is explored in section 2.10 below.

2.10 Free Carrier Effects

The free-carrier injection to, or depletion from, a silicon waveguide strongly affects its optical properties. Traditionally, the change in index of refraction, Δn, and the absorption, $\Delta\alpha$, induced by the presence of free-charge carriers is calculated using the Drude model [7]. The formulae are described thus:

$$\Delta n = -\frac{e^2\lambda^2}{8\pi^2 c^2 \epsilon_0 n}\left[\frac{\Delta N_e}{m^*_{ce}} + \frac{\Delta N_h}{m^*_{ch}}\right] \tag{2.117}$$

$$\Delta\alpha = \frac{e^3\lambda^2}{4\pi^2 c^3 \epsilon_0 n}\left[\frac{\Delta N_e}{m^{*2}_{ce}\mu_e} + \frac{\Delta N_h}{m^{*2}_{ch}\mu_h}\right] \tag{2.118}$$

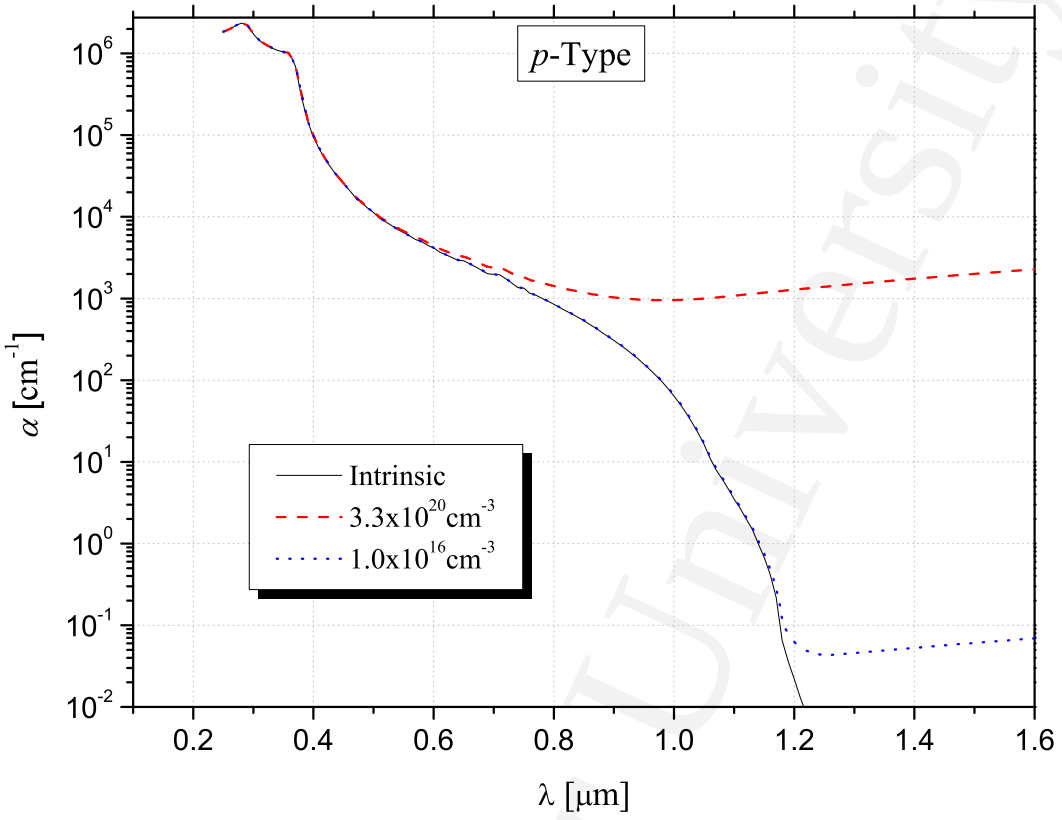

Figure 2.17: **The absorption coefficient of c-Si as a function of wavelength for intrinsic silicon [75], p-type silicon with typical doping concentration of $1.0 \times 10^{16}\mathbf{cm}^{-3}$ and with a high doping concentration of $3.3 \times 10^{20}\mathbf{cm}^{-3}$, extracted from [76].**

where e is the electronic charge, m^*_{ce} is the conductivity effective mass of electrons, m^*_{ch} is the conductivity effective mass of holes, μ_e is the electron mobility, μ_h is the hole mobility, ΔN_e is the change in electron concentration and ΔN_h is the change in hole concentration. However, an empirical expression for both Δn and $\Delta\alpha$ at $\lambda = 1.55\mu$m was reported by *Soref and Benett* [29, 77]

$$\begin{aligned} \Delta n &= \Delta n_e + \Delta n_h \\ &= -8.8 \times 10^{-22} (\Delta N_e) - 8.5 \times 10^{-18} (\Delta N_h)^{0.8} \end{aligned} \tag{2.119}$$

$$\begin{aligned} \Delta \alpha &= \Delta \alpha_e + \Delta \alpha_h \\ &= 8.5 \times 10^{-18} (\Delta N_e) + 6.0 \times 10^{-18} (\Delta N_h) \end{aligned} \tag{2.120}$$

From eq.(2.119) it is noted that the refractive index decreases as the concentration of carriers increases. Furthermore, from eq.(2.119) and eq.(2.120) (Figure 2.18) it is noted that a change in refractive index must also result in a change in absorption.

2.11 The Integration of Electrical and Optical Functions

In silicon photonics, the *pn*-junction diode acts as a selective barrier to charge carrier flow (current will flow readily in one direction —forward bias— but not in the other —reverse bias—) and provides a simple and effective way to control the concentration of free-charge carriers in order to modify the optical properties of the silicon waveguide. A great deal of the experimental work performed toward the completion of this thesis exploited the integration of a *pn* or p-i-n diode with a silicon waveguide. Therefore, a brief review of the basic *pn*-junction theory is presented here.

McMaster University

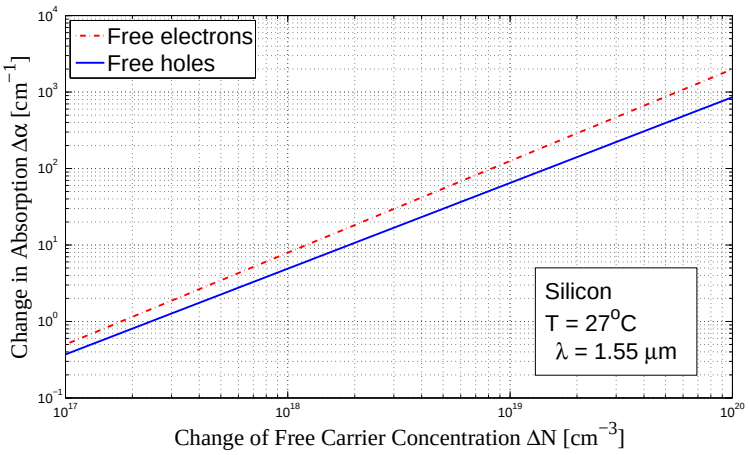

(a)

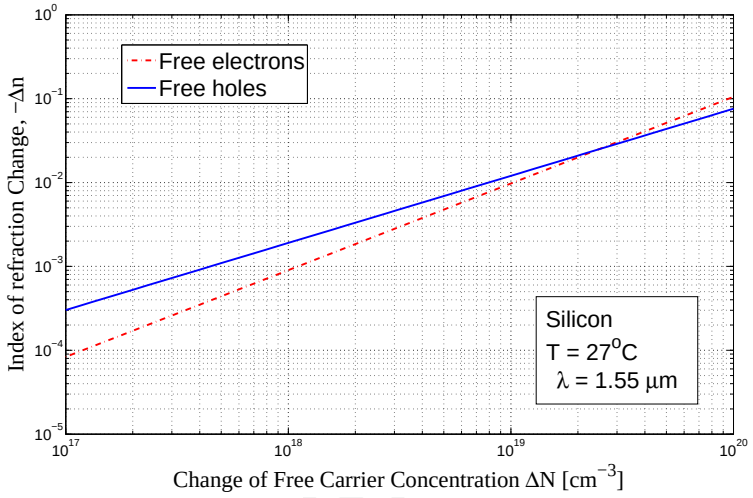

(b)

Figure 2.18: **(a) Absorption and (b) Index of refraction in c-Si as a function of free-carrier concentration at $\lambda = 1.55\mu$m and room temperature, extracted from [29].**

2.11.1 PN-Junction

When p-type and n-type materials[6] are placed in contact (in a conceptual experiment) with each other to form a junction, the junction behaves very differently than

[6]Semiconductors doped with donor impurities (pentavalent material, for example phosphorus) have an increase of number of electrons in the conduction band at room temperature and are known

either type of material alone. The difference in doping on each side of the junction cause a potential difference between the two type of materials and a diffusion of carries is expected to take place due to the large concentration gradient at the junction. Thus electrons diffuse from the n side to the p side and holes diffuse from p to n. However, this diffusion will create a charge imbalance by leaving behind uncompensated donor ions (N_d^+, positively charged), in the case of electron diffusion. Similarly, holes diffusing from p to n leave behind uncompensated acceptors (N_a^-, negatively charged). These uncompensated ions are fixed in place within the crystal lattice, thus developing a space charged-region on each side of the junction. The result is a region where majority carriers are depleted and implies in turn the existence of an electric field. The region that is depleted of mobile majority carriers at each side of the junction is referred to as *the depletion region* and is illustrated in Figure 2.19(a). The resulting electric field is directed from the positive charge to the negative charge region. Thus, this electric field will oppose the diffusion of holes from the p-side and electrons from the n-side and an equilibrium situation will be obtained [73, 78–81].

The number of majority charge carriers (electrons in the conduction band) per cm^3 in the n-type material is defined by the quantity

$$n_n = n_i \exp\left(\frac{E_f - E_i}{kT}\right) \tag{2.121}$$

and holes in the valence band in the p-type material

$$p_p = n_i \exp\left(\frac{E_i - E_f}{kT}\right) \tag{2.122}$$

as n-type materials. Those doped with acceptors (trivalent materials for example boron) have an increase number of holes in the valence band at room temperature and are known as p-type materials.

McMaster University

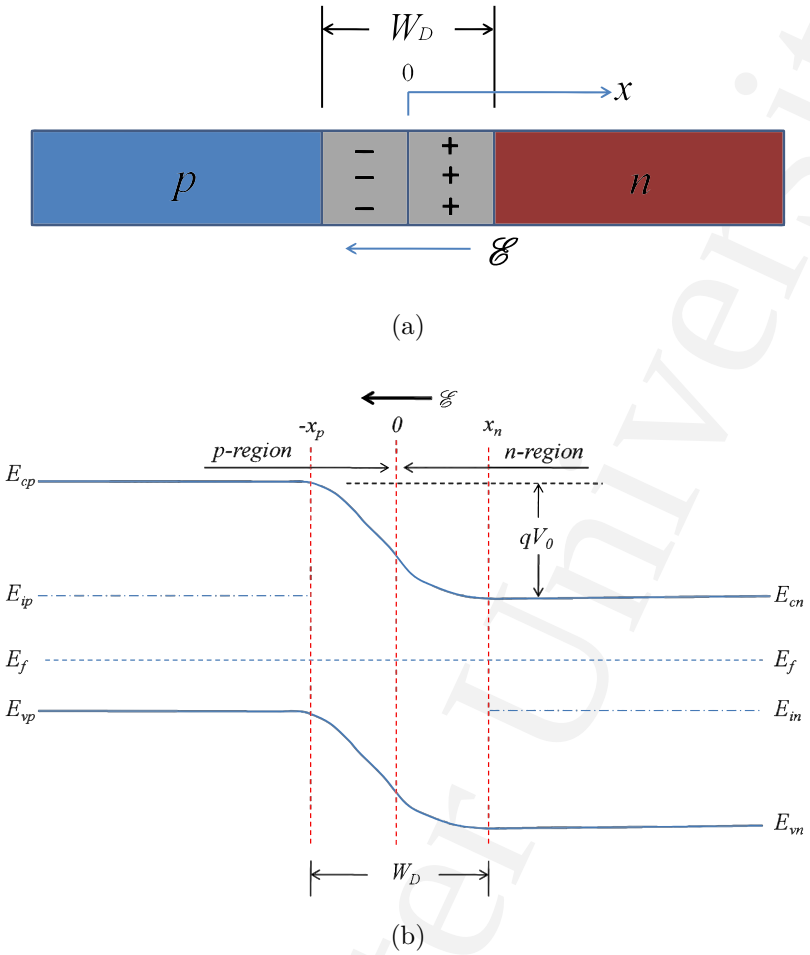

Figure 2.19: **(a) Junction showing space charge in the transition region W_D; (b) A *pn*-junction energy band diagram at thermal equilibrium.**

where E_f is the Fermi energy, which is the energy level at which the probability of occupation by an electron is 1/2, E_i is the intrinsic energy level and lies near the centre of the bandgap and n_i represents both the number of electrons and holes in their respective bands in intrinsic silicon ($n_i = 1.45 \times 10^{10} \text{cm}^{-3}$ at room temperature). The intrinsic carrier concentration can be related to the number of mobil electrons and holes such that $n_i^2 = n_n p_n = p_p n_p$.

McMaster University

In thermal equilibrium there is a net built-in potential V_0 across the depletion region, which cause the energy band to bend, Fig. 2.19(b). If the doping concentration is known, the built-in potential of an abrupt *pn*-junction can be calculated using the following expression

$$V_0 = \frac{kT}{q} \ln \left[\frac{N_a N_d}{n_i^2} \right] \tag{2.123}$$

where N_d is the concentration of donors in the n-side and N_a is the concentration of acceptors in the p-side of the junction. The depletion region width, W_D, is given as

$$W_D = \left[\frac{2\epsilon V_0}{q} \left(\frac{N_a + N_d}{N_a N_d} \right) \right]^{1/2} = \left[\frac{2\epsilon V_0}{q} \left(\frac{1}{N_a} + \frac{1}{N_d} \right) \right]^{1/2} \tag{2.124}$$

where ϵ is the permittivity of the medium and is defined as $\epsilon = \epsilon_0 \epsilon_r$, where ϵ_0 is the vacuum permittivity, ϵ_r is the relative permittivity and the permittivity for silicon at room temperature is 1.04×10^{-12} F/cm.

The current across a *pn*-junction is composed of the sum of two contributions - *drift* and *diffusion* current. Drift current is the movement of charge carriers under the influence of an electric field, such as the built-in electric field present across the depletion region. Diffusion current is the result of the difference in concentration of charge carriers between the two doping regions. In forward bias, with a positive voltage applied at the p-region, the junction is no longer in equilibrium and the electrostatic potential barrier and the built-in electric field within the depletion region are changed. In addition the separation of the energy bands are affected and the Fermi level is no longer constant. The result is a reduction in the potential barrier by the applied voltage V_f and a corresponding increase in the carrier diffusion current (more

McMaster University

electrons and holes now have sufficient energy to overcome the potential barrier). The width of the depletion region decreases because V_0 in equation 2.124 is now replaced by $V_0 - V_f$. The current due to diffusion increases significantly as more carriers are injected across the barrier into both the p and n regions, where they recombine with the abundant opposite-type of carrier. The diffusion current dominates in forward bias because for a small increase in voltage the result is a large increase in current, while the drift current remains small and constant independent of the applied bias. This is due to the fact that the drift current depends on how often minority carriers are generated within a diffusion length of the depletion region, not on how rapidly the carriers are swept through the potential barrier. In other words, the drift current depends solely on the small amount of minority carriers that become available not on the strength of the applied field. In reverse bias, where a negative potential is now applied at the p-region relatively to n-region, the depletion width becomes larger and the electrostatic potential barrier is increased, which decreases the diffusion of carriers. The result is that the only current flowing in this pn-junction is the small and relatively constant drift current. This current is generally called the *generation current,*[7] or in reverse bias the *reverse saturation current* or I_0.

In forward bias the probability of diffusion across the junction is found to increase by a factor of $\exp(qV/kT)$ and in reverse bias the diffusion current is reduced by the same factor with $V = -V_r$. In equilibrium ($V = 0$) the diffusion current is equal to the drift current, I_0. The resulting current-voltage equation for an ideal diode is given by

[7] As a reference to the carriers generated in the depletion region or minority carriers which diffuse to the junction and are collected.

McMaster University

$$\begin{aligned} I &= I_0 \left(e^{qV/kT} - 1 \right) \\ &= qA \left(\frac{D_p}{L_p} p_n + \frac{D_n}{L_n} n_p \right) \left(e^{qV/kT} - 1 \right) \end{aligned} \tag{2.125}$$

where A is the cross-sectional area of the diode, D_p and D_n are the diffusion coefficients of holes and electrons ($\mathrm{cm^2 s^{-1}}$) and L_p and L_n are diffusion lengths for holes and electrons. The diffusion length is the average length a carrier diffuses before recombining and can be expressed by $L = \sqrt{D\tau}$, where τ is the recombination lifetime. The diffusion coefficient, D, is related to the carrier mobility, μ ($\mathrm{cm^2/Vs}$) through the *Einstein relation* $D/\mu = kT/q$. The corresponding *current-voltage* $(I - V)$ characteristic curve is shown in Figure 2.20

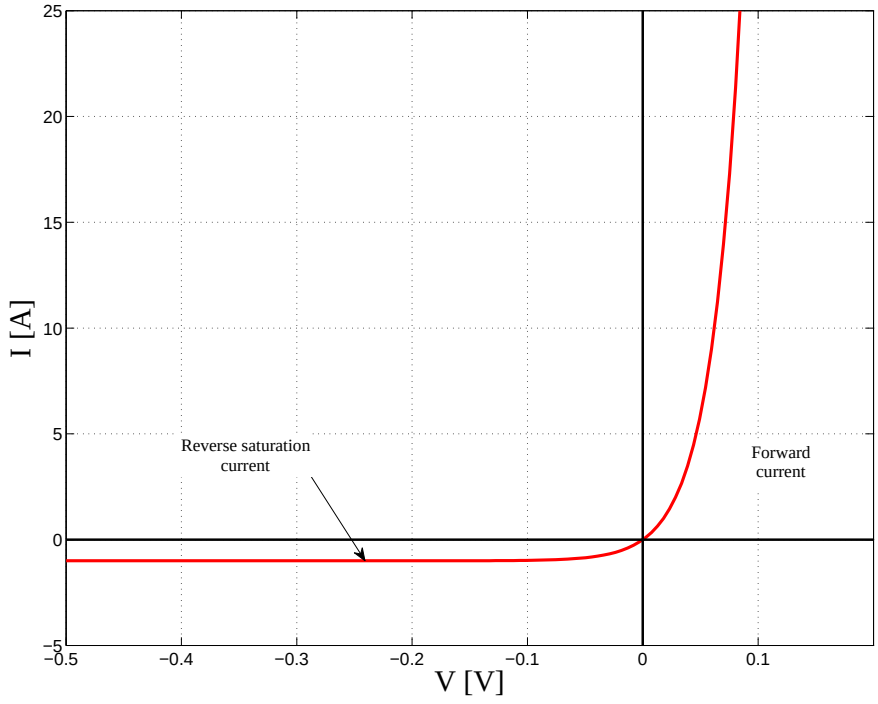

Figure 2.20: **I-V characteristic of an ideal diode.**

The transient response of a diode is affected by the transit time of charge carriers and capacitive effects. There are essentially two contributions to the capacitance of a *pn*-junction: the junction capacitance and the charge storage capacitance[8]. Junction capacitance is due to the dipole formed by the ionized donors and acceptors in the transition region and dominates in reverse bias. Charge storage capacitance, which dominates in forward bias operation of the diode, is determined by the minority carrier lifetime and the operating current. The junction capacitance, C_j, of an abrupt *pn*-junction is given by

$$C_j = \epsilon A \left[\frac{q}{2\epsilon \left(V_0 - V \right)} \frac{N_d N_a}{N_d + N_a} \right]^{1/2} = \frac{\epsilon A}{W} \tag{2.126}$$

which is an analogy to the parallel plate case where $C = \epsilon A/d$, with d as the plate separation. The junction capacitance decreases with an increase on the width of the depletion region. Therefore, as the reverse bias voltage is increased the junction capacitance is reduced. The diffusion capacitance, C_D, for a long and abrupt *pn*-junction and forward bias voltage $V \gg kT/q$ is given by the expression

$$C_D = \frac{q}{kT} \tau_p I \tag{2.127}$$

where τ_p is the minority charge carriers life time and I is the operation current.

2.12 Summary

This chapter presented the basic theory required for an understanding of the physical concept of light trapping and guiding in an optical waveguide, which is the

[8]The charge storage capacitance is sometimes called diffusion capacitance.

McMaster University

main structure used in this thesis work. The effective index method was described as a way to calculate the single mode conditions in 3d waveguide structures. Some of the most common loss mechanisms associated with waveguide structures were quantified. Optical absorption mechanisms in silicon and in particular the effect of free-carries on the real and imaginary part of the index of refraction of silicon were discussed. Finally, the basic working mechanism of a *pn*-diode, which is the configuration used to electrically modify the optical properties of the waveguide structure, was described. Theoretical considerations beyond this chapter are introduced as required throughout this thesis (for example to described the model for deep-level absorption). It is suggested that this approach enables the reader to consider such theory in the context of the specific work addressed.

McMaster University

McMaster University

Chapter 3

Thallium-Doped SOI Rib Waveguide

In the present chapter the effect of thallium doping of a silicon waveguide on the optical absorption of sub-band wavelengths around 1550nm is modeled and experimentally determined. These foundation measurements are used to assist in the design of the modulator described in chapter IV.

3.1 Background

Ion implantation is a useful way to introduce defects into the silicon lattice in order to increase the optical absorption at the communication wavelengths around 1550nm. In previous work [82], it was observed and reported that the type (either n-type or p-type) of background doping and its concentration influence the defect absorption strength. This effect was demonstrated in a waveguide structure [83].

A deep level impurity[1] located in silicon is almost completely un-ionized at room

[1]Impurity levels are considered "deep" if their distance from the band edges is larger compared

McMaster University

temperature because of the depth of the ionization energy level. Light at a wavelength of 1550nm may cause charge excitation from the valence band to the impurity level positioned in the bandgap, Fig. 3.1(a), or from the impurity level to the conduction band, Fig. 3.1(b). If the energy required to induce a charge excitation from the trapping level to the conduction band is greater than 0.82eV ($E > E(\lambda = 1550nm)$), Fig. 3.1 (a), excitation is not possible. Therefore, the impurity level behaves only as a trapping level. The concentration of deep level impurities is denoted by N_T ($N_T = n_T + p_T$) and in silicon can exist in a charged as well as a neutral state [86]. This study only focus on deep levels that present a single impurity level in the silicon bandgap and can only be single charged (+ or −). For example, when N_T is a *deep-donor impurity* (*i.e.* $n-$type deep-level), n_T denotes the amount of deep levels occupied by an electron which, for this type, corresponds to a neutral charge state and p_T is the amount of deep centres unoccupied by electrons (or occupied by holes) which corresponds to an ionized state with positive charge. However, if N_T is a *deep-acceptor level* (*i.e.* $p-$type deep-level), n_T refers to the ionized state (negatively charged) or centres occupied by electrons and p_T is the concentration of unoccupied centres and therefore, with a neutral charge state[2].

This behavior could become useful for active devices, since a large shift in absorption can be achieved by simply changing the defect charge state. This charge state depends on the defect level occupancy which may be altered by injecting or removing free carriers from the system. Previous experimental infrared absorption studies of thallium in silicon show the existence of a single-acceptor-impurity level to exist at 0.246eV above the valence band [87, 88], which makes thallium a deep single-impurity-level in silicon [78].

to k_bT (for example, $>3k_bT$) at room temperature; however, it is usually considered a level to be "deep" if it occurs at an energy which is greater than about 0.1eV from a band edge [84, 85].

[2]Or neutral state.

McMaster University

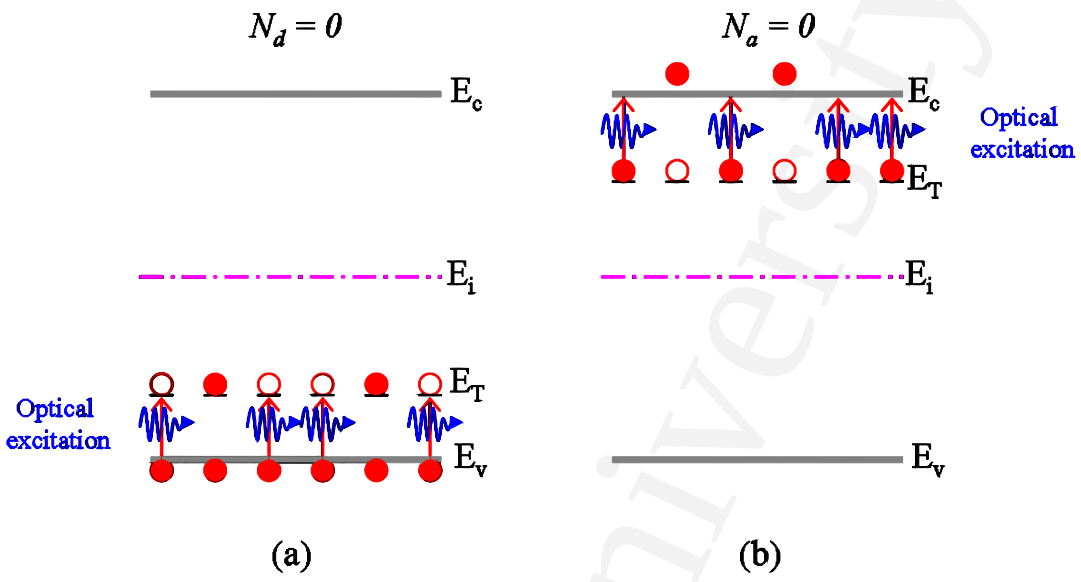

Figure 3.1: **Band diagram of silicon containing, (a) deep acceptor centres with ionization energy E_T without shallow donors, N_d and, (b) deep donor centres of energy E_T without shallow acceptors centres, N_a.**

3.1.1 Absorption Coefficient due to Thallium

The optical absorption of thallium-doped silicon at the 1550nm wavelength results from the excitation of an electron from the valence band into a neutral thallium centre located 0.246eV above the valence band. This transition changes the charge state of the centre from neutral to negative. This optically excited transition has an optical cross-section of approximately $2.6 \times 10^{-17} cm^2$ [89] for photons with an energy equivalent to 1550nm wavelength. The energy required to optically excite an electron from the thallium centre into the conduction band is 0.87eV, which is higher than the energy associated with 1550nm photons. The absorption coefficient strength for 1550nm has been found to be proportional to the overlap integral for the optical waveguide mode and the concentration of unoccupied (neutrally-charged) thallium centres [40], defined as

$$\alpha_d = \sigma_p^{opt} \iint_{x,y} \Phi(x,y) \left[N_T(x,y) - N_T^-(x,y) \right] \, \mathrm{d}x \, \mathrm{d}y \tag{3.1}$$

where σ_p^{opt} is the cross-section for optical absorption at 1550 nm wavelength; $\Phi(x,y)$ is the normalized (unit power) optical waveguide mode profile; $N_T(x,y)$ is the thallium concentration profile and N_T^- is the ionized (negatively charged) thallium centre profile.

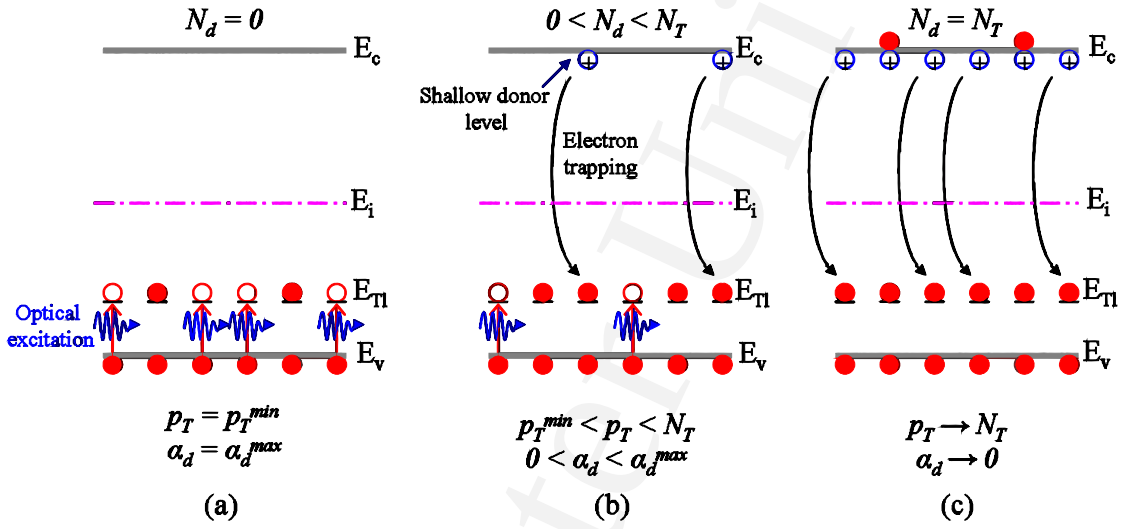

Figure 3.2: **Band diagram of silicon containing a constant trapping centres concentration, N_T, and (a) without shallow donors, N_d, (b) with a medium concentration of shallow donor, N_d, and (c) with a shallow donor concentration similar or equal to the trapping centres concentration, N_T.**

Thallium is a group-III impurity, which makes it a p-type dopant in silicon. In the three cases shown in figure 3.2, the thallium concentration, N_T, is depicted as being kept constant and the background doping concentration of a shallow donor such as phosphorus, N_d, is changed in order to demonstrate the effect of changing the

McMaster University

background doping concentration (phosphorus) on the optical absorption strength of thallium. Figure 3.2(a) shows that when there are no shallow donors, N_d, many deep acceptor centres are neutrally-charged and p_T takes its minimum value (p_T^{min}). Therefore in this case, many electrons are capable of being optically excited from the valence band to the thallium level. In figure 3.2(b), some shallow donors, N_d, are added. These donors supply free electrons that are readily trapped by the vacant deep level acceptors, decreasing the number of sites available for electrons to be optically excited. In other words, the thallium levels are being compensated. Figure 3.2(c), shows that when a large concentration of shallow donors are introduced the free electrons would completely compensate the deep acceptor centres, making the optical excitation process via electron excitation into the deep levels impossible. This model of thallium induced absorption leads to the somewhat remarkable prediction that optical absorption in deep-level doped silicon would decrease with increasing free carrier concentration (in contrast to the common observation of free carrier absorption, described by Figure 2.18(a)).

3.2 Calculation of the Concentration of Neutrally-Charged Deep-levels

In order to calculate the concentration of neutrally-charged centres as a function of the deep-level impurity and background doping concentration, I will review the generation-recombination (G-R) process described by the Shockley-Read-Hall (SRH) mechanism [90–94].

McMaster University

3.2.1 Carrier Recombination via Impurities

The *SRH* recombination process takes place mostly due to impurities having energy levels deep in the bandgap; these are so-called *G-R* centres or traps [95]. Referring to Figure 3.3, a *G-R* centre or trap can be seen to be in either one of two possible states, the occupied and the neutrally-charged. In its neutral state, it can capture an electron from either the valence band (Fig. 3.3(b)) or the conduction band (Fig. 3.3(c)). In its occupied state, it can give (emission process) its electron to either the valence band (hole capture, Fig. 3.3(a)) or the conduction band (Fig. 3.3(d)). The optical transition occurs when light with $E(\lambda) < E_g$ is able to excite an electron from the valence band to a neutrally-charged trapping level[3] (hole emission, Fig. 3.3(e)) or when an electron, occupying a trapping centre, is excited by a photon with $E(\lambda) > (E_c - E_T)$ enabling a promotion to the conduction band, Fig. 3.3(f).

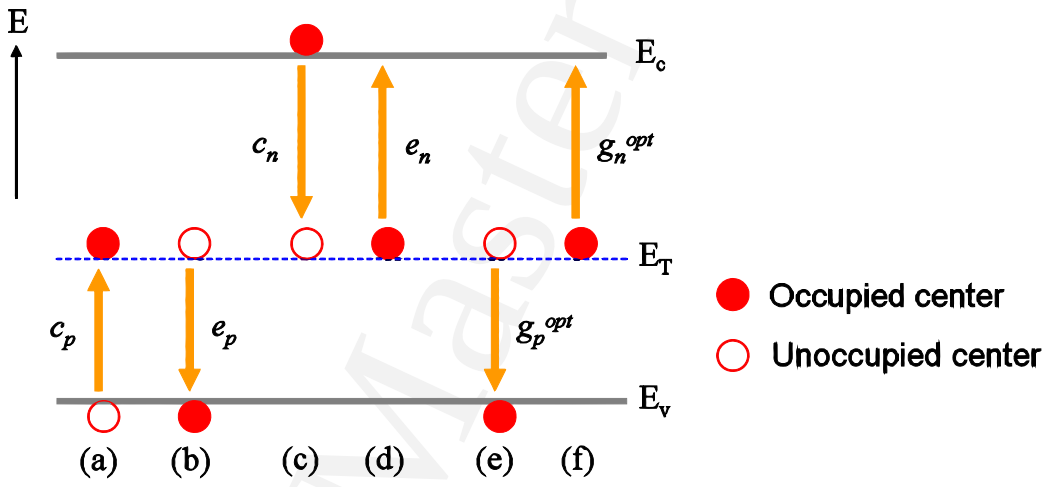

Figure 3.3: **Band diagram for a semiconductor with a single deep-level impurity located at E_T. The thermal capture and emission process and optical generation are described in text.**

[3] E_g is the band gap energy

For process (a) in figure 3.3, the rate of capturing a hole is proportional to the hole capture coefficient, c_p, the concentration of occupied trap states, n_T, and the hole density in the valence band, p; hence, the rate can be written as

$$U_{cp} = c_p \left(N_T - p_T\right) p = c_p n_T p \tag{3.2}$$

where N_T is the total density of deep-level impurities, p_T the concentration of neutrally-charged (*i.e.* occupied by holes) centres, n_T the concentration of occupied traps and p is the concentration of holes in the valence band. Using this terminology we may write:

$$N_T = n_T + p_T \tag{3.3}$$

Process (b), hole emission rate, is defined by the hole emission coefficient, e_p, and the density of centres occupied by holes,

$$U_{ep} = p_T e_p = p_T c_p p_1 = p_T c_p n_i \cdot exp\left(-\frac{E_T - E_i}{k_b T}\right) \tag{3.4}$$

where p_1 is the number of holes in the valence band for the case in which ($E_f = E_T$) [90], n_i is the intrinsic carrier concentration, E_T is the position of the deep-level impurity, E_i is the intrinsic position of the Fermi energy level, k_b is the Boltzmann constant and T is the temperature. The expressions for process (c) and (d) are obtained in a similar manner, where the electron capture rate is

$$U_{cn} = c_n p_T n \tag{3.5}$$

McMaster University

with n as the concentration of electrons. The electron emission rate is

$$U_{en} = n_T e_n = n_T c_n n_1 = n_T c_n n_i \cdot exp\left(-\frac{E_i - E_T}{k_b T}\right) \tag{3.6}$$

where n_1 is the number of electrons in the conduction band for the case in which the Fermi levels falls at ($E_f = E_T$) [90].

Optical emission rate of holes, g_p^{opt}, from the impurity level to the valence band[4] is proportional to the optical cross-section for capture of holes, σ_p^{opt}, the optical flux, ϕ_{opt} [Photons/cm^{2}s], and the concentration of neutrally-charged centres p_T.

$$g_p^{opt} = \sigma_p^{opt} \phi_{opt} p_T \tag{3.7}$$

The Optical emission rate of electrons, g_n^{opt}, from the impurity level to the conduction band is proportional to the optical cross-section for capture of electrons, σ_n^{opt}, the optical flux, ϕ_{opt} [Photons/cm^{2}s], and the concentration of occupied centres n_T.

$$g_n^{opt} = \sigma_n^{opt} \phi_{opt} n_T \tag{3.8}$$

In steady state, the net rate of change of concentration of holes must be equal to that of electrons, then

$$U_{ep} - U_{cp} + g_p^{opt} = U_{en} - U_{cn} + g_n^{opt} \tag{3.9}$$

[4]It is equivalent to the promotion of an electron from the valence band to an empty thallium level by the absorption of a photon.

McMaster University

substituting equations (3.2), (3.4), (3.5) and (3.6) into eq.(3.9) and rearranging terms, we obtain

$$p_T = \left(\frac{e_n + c_p p + \sigma_n^{opt} \phi_{opt}}{c_p p + e_p + \left(\sigma_p^{opt} + \sigma_n^{opt}\right) \phi_{opt} + c_n n + e_n} \right) N_T \tag{3.10}$$

which is the expression for neutrally-charged deep centres. The carrier capture coefficients are defined as

$$c_n = \sigma_n \upsilon_{Th-n} \tag{3.11}$$

$$c_p = \sigma_p \upsilon_{Th-p} \tag{3.12}$$

where σ_p is the cross section of holes and σ_n for electrons, and $\upsilon_{Th-p},\ \upsilon_{Th-n}$ are the thermal velocities for holes and electrons respectively [96]. For thallium the capture cross-section for holes is $2.4 \times 10^{-14}\text{cm}^2$ [88] and the capture cross-section for electrons is $1.0 \times 10^{-22}\text{cm}^2$ [97].

3.2.2 Numerical Modeling of Thallium induced absorption

Since thallium is a deep-acceptor-level, not all the impurity centres are ionized at room temperature, where this ionization fraction depends on the concentration of background doping, thallium doping, capture rate, emission rate and temperature. In this section a model is developed that calculates the occupancy concentration. This model applies to all cases where a shallow level impurity is co-doped with a deep-level impurity. The results presented here are for the specific case of silicon co-doped with thallium and phosphorus. Some terms described in eq.(3.3) are replaced to represent the specific case for thallium such that, N_T is now N_a and n_T is N_a^-; providing

McMaster University

$$N_a = N_a^- + p_T \tag{3.13}$$

From the charge neutrality equation

$$n + N_a^- = p + N_d^+ \tag{3.14}$$

it is assumed that all the shallow donors are ionized, $N_d^+ = N_d$, then,

$$n + N_a^- = p + N_d \tag{3.15}$$

using eq.(3.13) and the expressions $n = n_i^2/p$ in eq.(3.15), we get

$$\left(1 - \frac{e_n + c_p p + \sigma_n^{opt}\phi_{opt}}{c_p p + e_p + \left(\sigma_p^{opt} + \sigma_n^{opt}\right)\phi_{opt} + c_n n + e_n}\right) N_a = \frac{p^2 + N_d p - n_i^2}{p} \tag{3.16}$$

with $p = n_i \cdot exp\{(E_i - E_f)/k_b T\}$. Solving this expression, one may obtain the Fermi energy level position required in the calculation of p_T, equation (3.10). Figure 3.4 shows the concentration of centres neutrally-charged for ten different thallium concentrations as a function of varying phosphorus concentration ranging from 10^{15} to 10^{18}cm^{-3}. The maximum concentration value for thallium was limited to its solid solubility in silicon of $3.7 \times 10^{17}\text{cm}^{-3}$ [98].

Figure 3.4 shows how the concentration of thallium centres neutrally-charged, p_T, changes as a function of background doping concentration. These results support the notion that thallium levels are compensated by the presence of phosphorus up to the maximum phosphorus concentration.

McMaster University

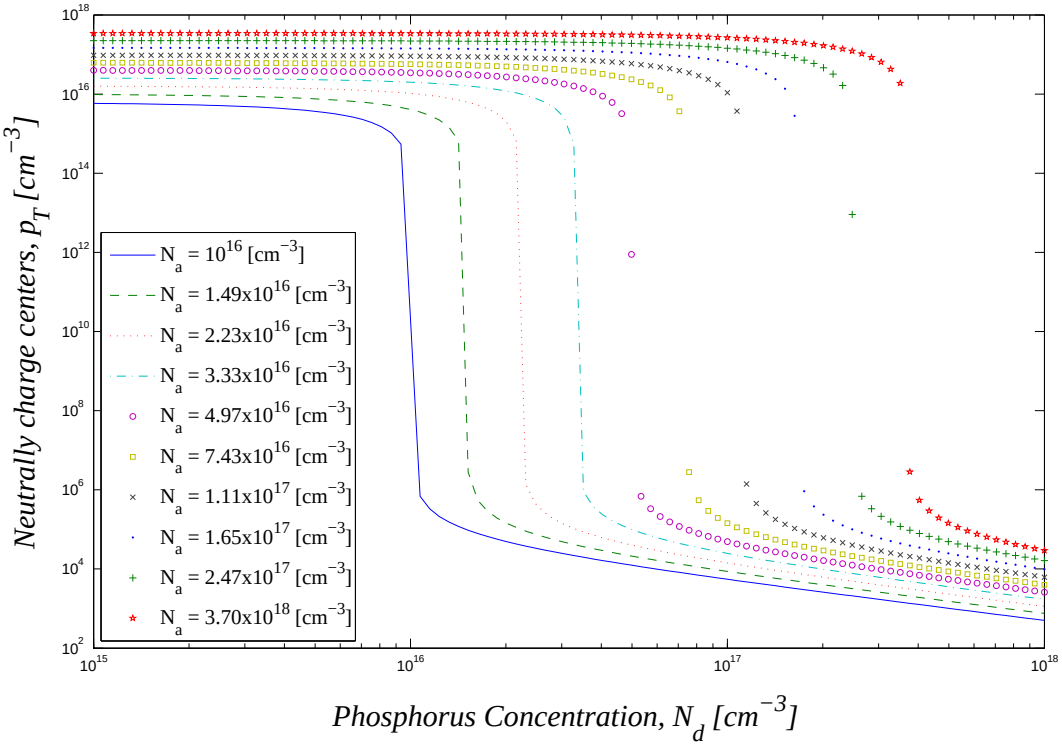

Figure 3.4: **Neutrally-charged thallium centres, p_T, as a function of phosphorus background doping, N_d, without optical excitation.**

The fraction of neutrally-charged to the total concentration of thallium centres for a constant background concentration can be increased by increasing the thallium concentration and, for a constant concentration of thallium, the fraction can be decreased as the background doping concentration is increased, as shown in Fig. 3.5. For example, for a thallium concentration of 10^{16}cm^{-3} at a phosphorus background concentration of 10^{16}cm^{-3}, ~60% of the thallium centres are neutrally-charged. But this percentage is decreased as the background doping is increased up to the point where all the centres are compensated. It is recalled that the amount of photons absorbed is directly proportional to the amount of neutrally-charged centres, as expressed from eq.(3.1). From the previous discussion, optical modulation by ways of

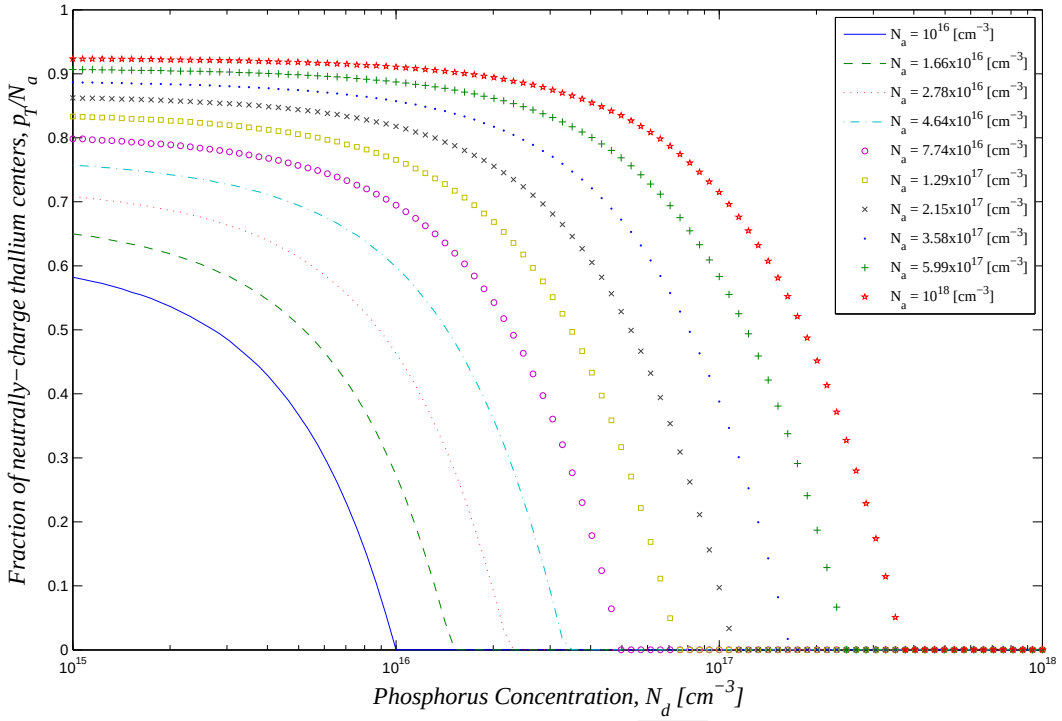

Figure 3.5: **Fraction of neutrally-charged thallium centres, p_T/N_a as a function of phosphorus background doping, N_d, without optical excitation.**

varying p_T, should be possible. For example, this effect can be potentially useful for optical modulation in silicon waveguide geometry. In order to explain this application further, we consider a waveguide structure doped with thallium with a concentration much higher than the shallow donor background doping concentration ($N_a \gg N_d$). From the top-left area of Fig. 3.5, one observes a high density of neutrally-charged centres which implies a high optical absorption, α_d. If a reverse bias is applied to the waveguide, it induces a depletion effect with the result that holes would be emitted from the thallium centres (*i.e.* capture of electrons from the valence band). This hole emission decreases both p_T and α_d to minimum values. On the other hand, if the background doping concentration is comparable or higher than that of thallium

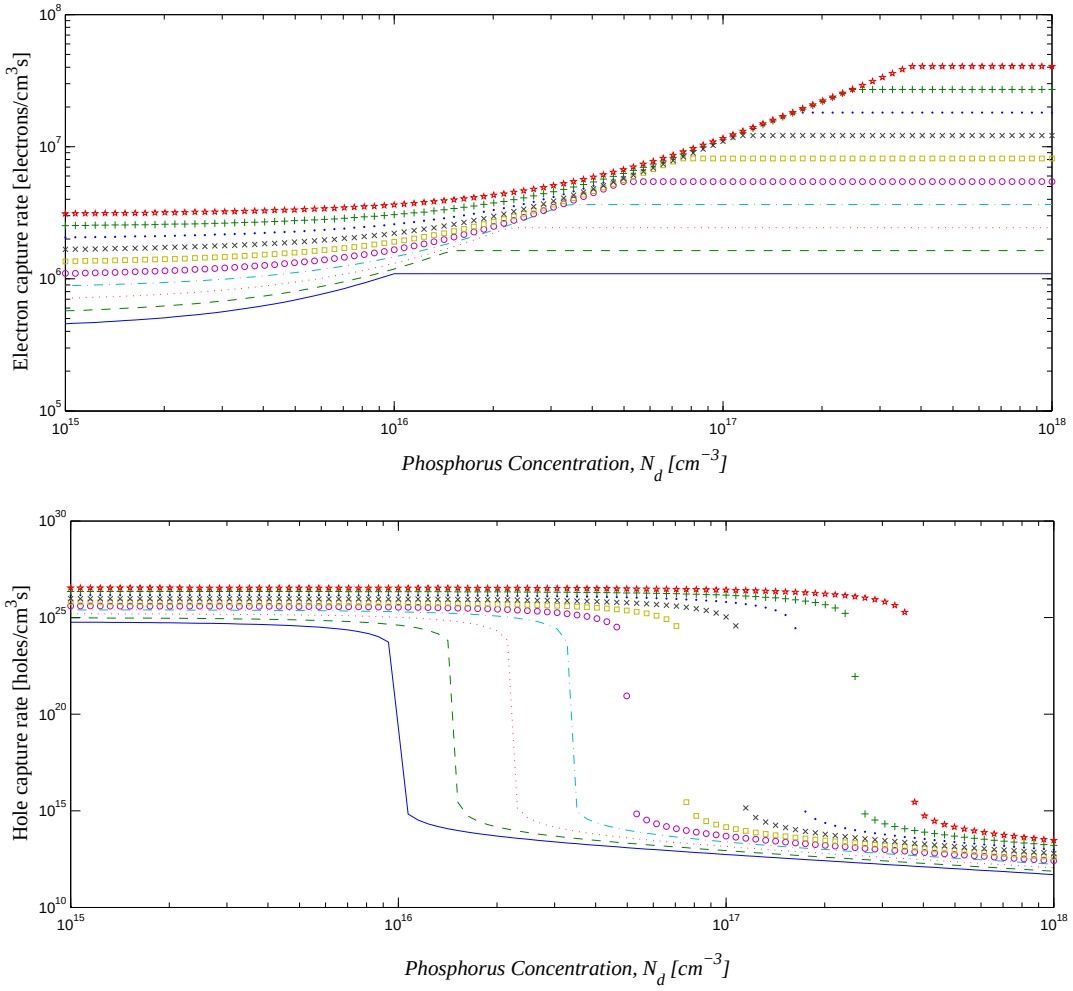

Figure 3.6: **Capture rate for electrons and holes for ten different concentration of thallium (as in Fig. 3.5) as function of phosphorus background doping without optical excitation.**

(bottom-right part of Fig. 3.5), all the thallium centres will be completely compensated ($N_a^- \approx N_a$). Hence, minimum absorption results. If a forward bias field is applied to the waveguide structure, it causes p_T to increase and enhances absorption. This behavior is possible because optical absorption by a deep-impurity level is proportional to the neutrally-charged centres which is largely dependent on the

capture rates for electrons and holes, eq.(3.10). For example, in Figure 3.6 when the thallium concentration is higher than the phosphorus concentration, the hole capture rate is ∼18 orders of magnitude higher than the electron capture rate. When the phosphorus concentration matches and/or exceeds that of thallium, the hole capture rate drops drastically but it is still higher than the capture rate for electrons. Therefore, for thallium centres the injected holes will be preferentially captured over the electrons in a bipolar device [40, 99].

Change in the fraction of neutrally-charged thallium centres induced by light propagating trough a waveguide structure was calculated using eq.(3.10) and corresponding results are reported in Fig. 3.7. For the calculation of the fraction of neutrally-charged centres, in steady state, two conditions were assumed: first, there is no optical transition from the trapping level to the conduction band, *i.e.* $\sigma_n^{opt}(\lambda = 1550nm) = 0$ due to $(E_c - E_T) > E(\lambda = 1550nm)$; second, each photon absorbed will excite an electron from the valence band to the thallium centre. Modeling was performed for a waveguide with cross-sectional area of $10\mu\text{m}^2$.

It is noted from Fig.3.7 that the greater the number of photons propagating trough the waveguide the greater the change in the fraction of neutrally-charged thallium centres, p_T/N_a. This small change (decrease) in the fraction of neutrally-charged centres was expected from eq.(3.10) and it is more evident for low concentrations of both thallium and phosphorus (left-hand-side on Fig.3.7*a*). It is noteworthy that the fraction of neutrally-charged thallium centres is highly affected by the ratio between the hole capture cross-section and the hole optical cross-section, *i.e.* since the hole capture-cross section is ∼900 larger than the optical absorption cross-section for holes, after a photon excites an electron to the trapping level, it is more likely that the centre will re-trap a hole. Thus, even for high concentration of photons propa-

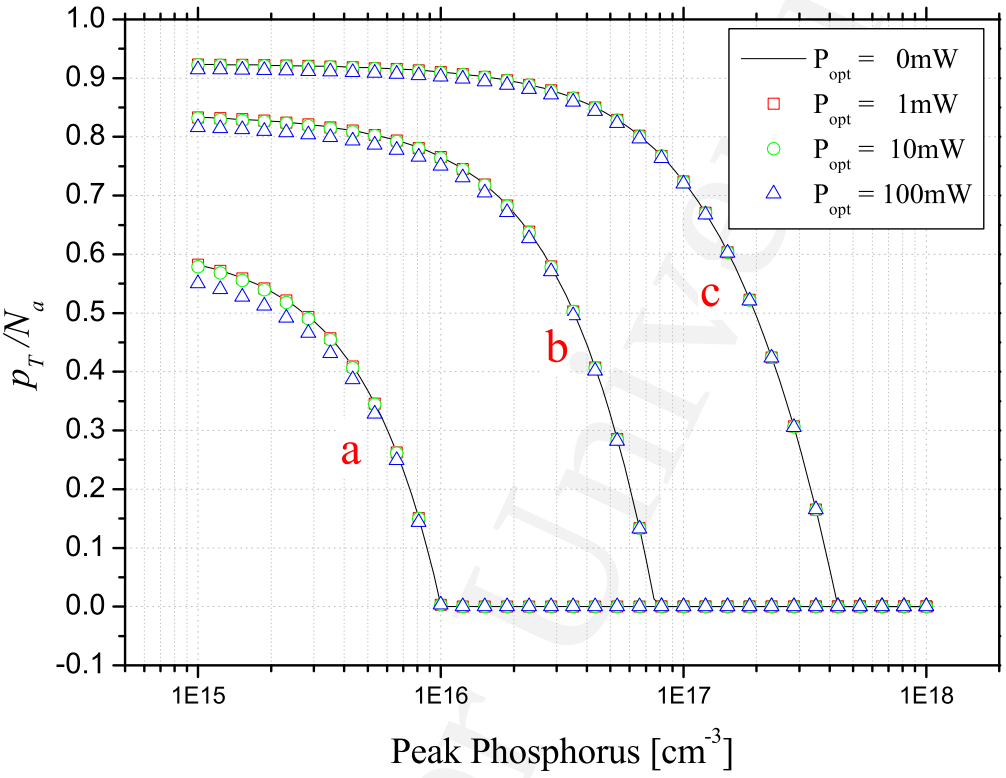

Figure 3.7: **Fraction of neutrally-charged thallium centres, p_T/N_a as a function of phosphorus background doping with optical excitation for: (a) $N_a = 1 \times 10^{16}\mathbf{cm}^{-3}$, (b) $N_a = 7.43 \times 10^{16}\mathbf{cm}^{-3}$ and (c) $N_a = 3.7 \times 10^{17}\mathbf{cm}^{-3}$.**

gating through the doped region, there is no considerable change, and practically no change when both thallium and phosphorus concentrations are similar to the fraction of neutrally-charged thallium centres induced by an optical transition. If the difference between cross-sections were smaller, or the quantity of photons propagating through were comparable to the thallium concentration, the change in occupancy fraction would be quite evident up to the point that almost all thallium centres may

be occupied.

3.3 Experimental Determination of Thallium Induced Optical Absorption in a Silicon Waveguide

In the following sections, sample fabrication procedure is discussed together with the numerical model developed in order to obtain the absorption coefficient due to thallium centres in a silicon waveguide.

3.3.1 Sample Fabrication

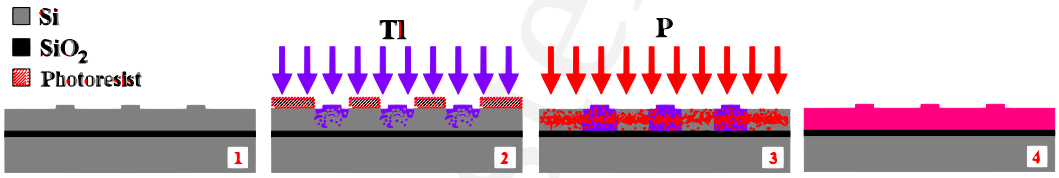

Figure 3.8: **Summary of sample fabrication. Step 1, waveguide structure. Step 2, thallium implantation into waveguides and thermal annealing,. Step 3, phosphorus implantation and a second thermal annealing, and step 4, sample ready for optical characterization.**

In order to design a process flow for the fabrication of thallium doped rib waveguide, a number of issues were considered: (1), thallium is a heavy mass ion with a relatively low diffusion constant [100]; (2), the waveguide thickness was 2.5μm;

McMaster University

(3), ideally a homogeneous concentration of thallium and phosphorus throughout the waveguide cross-section is desired. These three issues produced limitation for the implantation and annealing conditions used in fabrication.

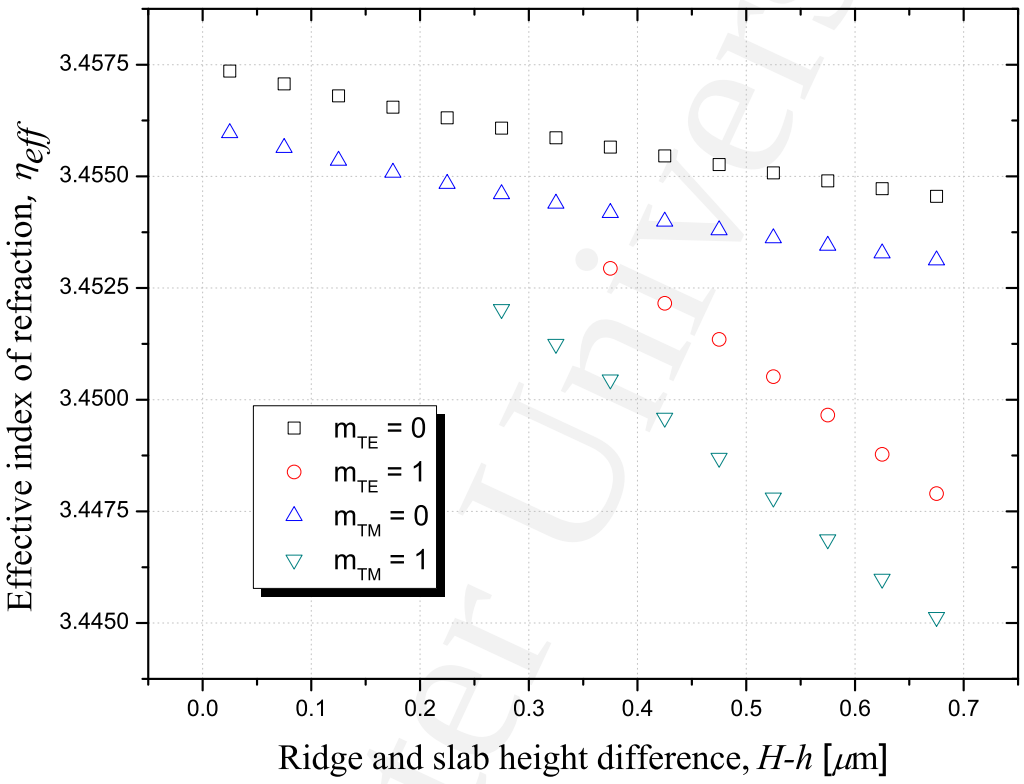

Figure 3.9: **Higher order modes are observed in a 4μm width waveguide, when the etching depth is more than 0.25μm and 0.35μm for TM and TE polarization respectively. Waveguide dimensions based on Fig. 2.8.**

Silicon rib waveguides were fabricated using a SOI wafer with a guiding layer of 2.5μm on a 0.375μm thick buried oxide (BOX). Eight samples of approximately 2×2 cm^2 were cleaved, and then cleaned using the RCA cleaning procedure [101,102]. The samples were annealed in a dry-oxygen environment for 30 minutes to grow ∼100nm thick oxide on the silicon over layer. Prior to the *Shipley 1808* photoresist (PR)

deposition the samples were heated at 110°C for five minutes to remove moisture. The samples were subjected to standard photolithography so that a waveguide pattern could be transferred to the PR, and etched into the oxide using a 10% buffered-HF. After the PR was removed, the waveguide pattern was transferred to the silicon via wet etching (using a 40% KOH + IPA solution, see Appendix A), where the thermal oxide layer was used as an etching mask (Fig. 3.8-1). The etching depth in silicon was chosen to ensure single-mode propagation (according to section 2.5), corroborated with the simulation results obtained with the commercial software *RSoft Software*. For a waveguide width of 4μm, no more than 0.25μm etching depth is required to ensure single mode propagation (Fig. 3.9). The single mode profile and intensity distribution along x and y are shown in Figure 3.10.

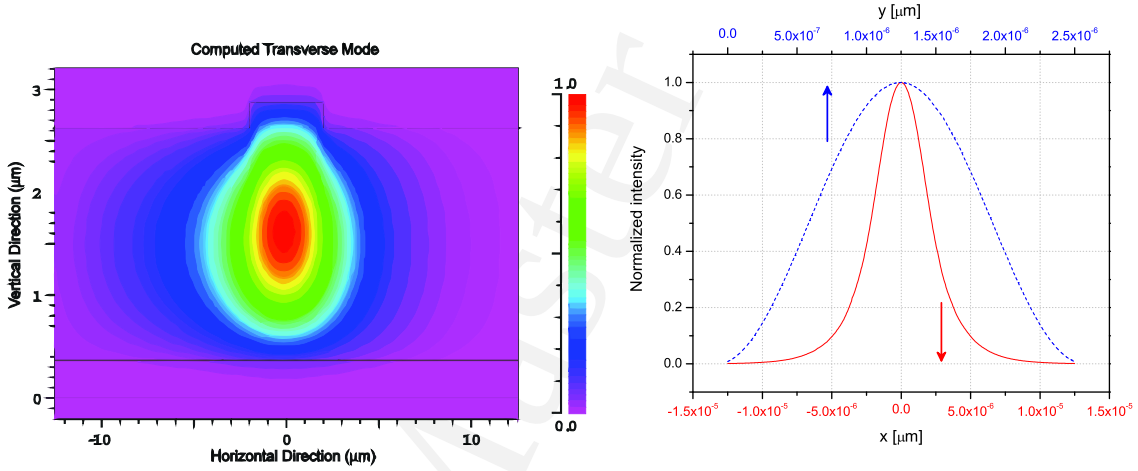

(a) (b)

Figure 3.10: **Single mode for a waveguide whose dimensions are H = 2.5μm, h = 2.25μm and W = 4μm, (a) Transversal profile and (b) Normalize intensity profiles for x and y direction.**

Windows of varying lengths centred on each waveguide, were defined subsequently

Table 3.1: **Summary of Tl and P implantation conditions for the SOI waveguides**

Thallium				Phosphorus			
		Annealing				Annealing	
Dose [cm^{-2}]	Energy [keV]	Temp. [°C]	Time [min]	Dose [cm^{-2}]	Energy [keV]	Temp. [°C]	Time [min]
7.4×10^{13}	1000	1100	90	-	-	1100	90
7.4×10^{13}				3.0×10^{12}	385		
7.4×10^{13}				6.0×10^{12}			
7.4×10^{13}				1.0×10^{13}			
7.4×10^{13}				2.0×10^{13}			
7.4×10^{13}				3.0×10^{13}			
7.4×10^{13}				7.0×10^{13}			
7.4×10^{13}				1.0×10^{14}			
1.2×10^{14}	1000	1100	90	-	-	1100	90
1.2×10^{14}				8.0×10^{12}	385		
1.2×10^{14}				1.0×10^{13}			
1.2×10^{14}				3.0×10^{13}			
1.2×10^{14}				5.0×10^{13}			
1.2×10^{14}				7.0×10^{13}			

McMaster University

using a 4μm thick PR, and used as a masking layer during ion implantation of thallium with an energy of 1MeV for a dose of 7.4×10^{13}cm^{-2} or 1.2×10^{14}cm^{-2} (Fig. 3.8-2). After the PR was removed from all the samples, they were annealed at 1100°C in a dry-oxygen environment for 90 minutes in order to diffuse and activate the implanted thallium. All samples but one were subjected to subsequent (unmasked) phosphorus implantation at an energy of 385 keV for doses ranging from 3×10^{12}cm^{-2} to 1×10^{14}cm^{-2} and all samples were further annealed at 1100°C in a dry-oxygen environment for 90 minutes (Fig. 3.8-4). This range of phosphorus doses provided co-doping of the thallium such that the thallium mediated optical absorption could be compared to the modeled results shown in Figure 3.5. The implantation conditions are summarized in Table 3.1. The implantation energies, annealing temperatures and annealing times were chosen in order to positioned the resulting thallium and phosphorus concentration profiles coincidentally. In addition, their peak concentration was required to be located as close to the waveguide centre as possible.

Phosphorus implantation contributes to free-carrier absorption along the whole waveguide length, while thallium centres contribute to the absorption only in the unmasked window. This simple design thus allows the separation of absorption due to free carriers and due to thallium mediated absorption.

The final sample preparation step was the definition of optical quality end-facets using a chip thinning and edge cleaving process.

3.3.2 Optical Loss Measurements

Using a 1550nm wavelength laser, optical absorption measurements were performed for all the waveguide on each sample. This was done by butt-coupling light into the rib waveguide through a tapered optical fiber. Light was collected by an

McMaster University

objective lens located at the opposite end of the waveguide. The collimated light was propagated through free space and measured using an InGaAs photodetector. Figure 3.11 depicts the optical set-up used for the measurements. Total measured loss, in dB, can be summarized by the following relationship;

$$\alpha_{Tot} = \alpha_d l_W + \alpha_i L + \zeta \tag{3.17}$$

where α_d is the absorption coefficient of thallium centres, in dB/cm, defined by eq.(3.1), l_W is the length of the thallium implantation window, α_i is the intrinsic absorption coefficient, which includes free-carriers absorption induced by phosphorus doping, L is the waveguide length and ζ is the coupling loss.

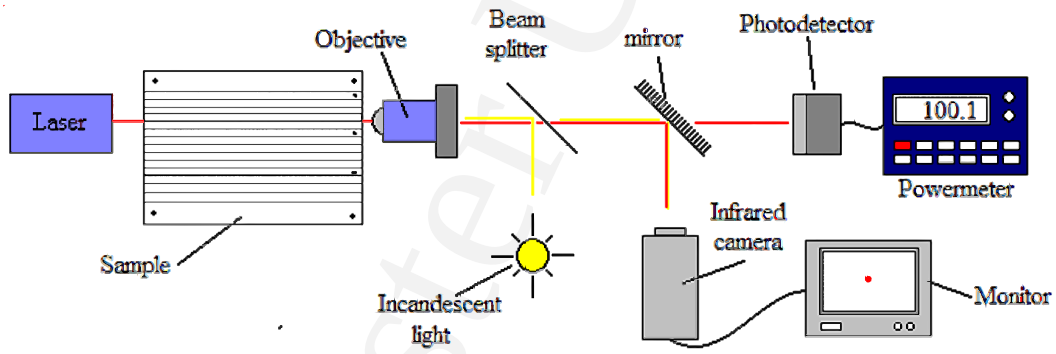

Figure 3.11: **Experimental set-up used for the optical measurements.**

The change in total loss value between waveguides, on the same sample, was dominated by the variation in l_W. In this case, free-carrier absorption and coupling loss were expected to be the same for all waveguides on the same sample. Hence, the last two terms in the right-hand side of eq.(3.17) can be considered to remain constant and the value of α_d can be extracted from a linear regression of α_{Tot} vs l_W. Figure 3.12 shows typical experimental data and corresponding linear fitting. It is noted that

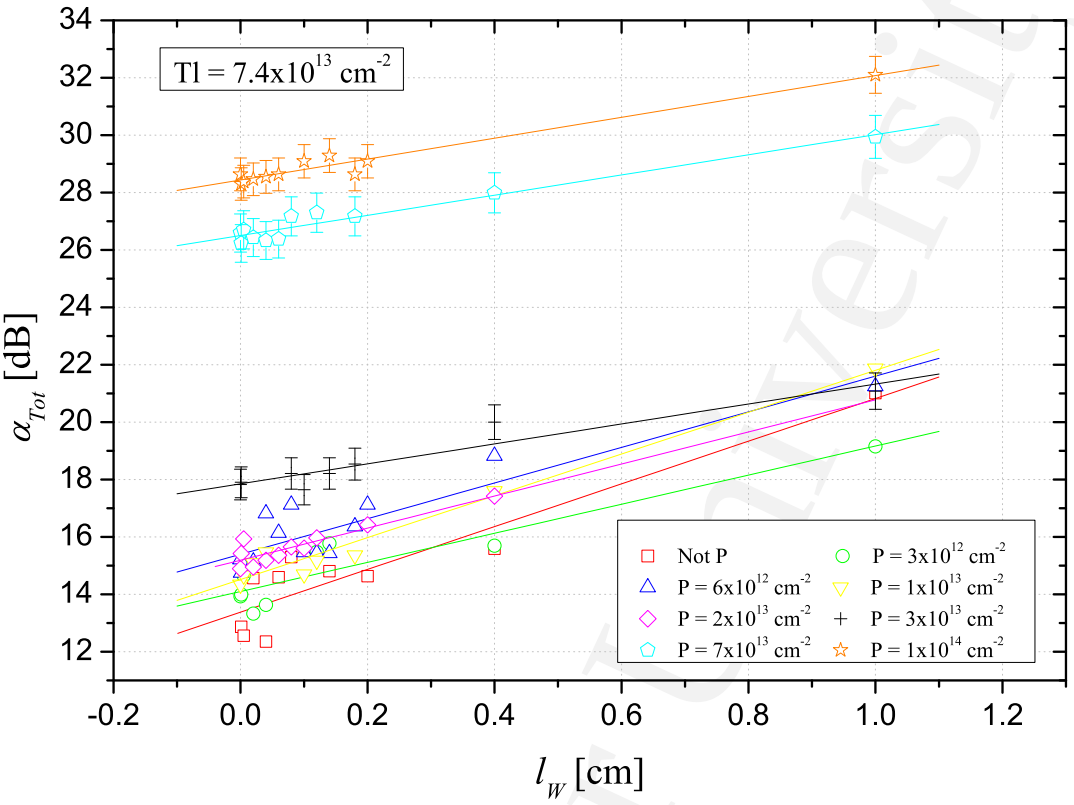

Figure 3.12: **Measurement results of optical loss vs thallium implantation window length, for a dose of Tl $= 7.4 \times 10^{13}$cm^{-2} and eight different phosphorus doses shown in figure. Error bars are similar for the rest of experimental data.**

the slope of the fitted curve decreases as phosphorus concentration increases, which is a result of thallium compensation. Recall that fewer neutrally-charged centres corresponds to less absorption. For high phosphorus concentration, full compensation of thallium centres is expected. However, even for the highest phosphorus doping concentration a slope in the fitted data is observed, which must be a consequence of residual neutrally-charged thallium centres. A possible explanation for this residual

absorption may be the conglomeration of thallium ions forming clusters that may not be compensated by phosphorus impurities, and therefore allowing optical absorption.

Table 3.2: **Thallium and phosphorus doses, peak concentration and α_d**

Thallium		Phosphorus		
Dose $[cm^{-2}]$	Peak Concentration $[cm^{-3}]$	Dose $[cm^{-2}]$	Peak Concentration $[cm^{-3}]$	α_d [dB/cm]
7.4×10^{13}	3.7×10^{17}	-	-	7.447±0.935
7.4×10^{13}		3.0×10^{12}	1.77×10^{16}	7.287±0.680
7.4×10^{13}		6.0×10^{12}	3.45×10^{16}	6.206±0.740
7.4×10^{13}		1.0×10^{13}	6.01×10^{16}	5.07±0.423
7.4×10^{13}		2.0×10^{13}	1.15×10^{17}	5.588±0.316
7.4×10^{13}		3.0×10^{13}	1.80×10^{17}	3.476±0.402
7.4×10^{13}		7.0×10^{13}	4.17×10^{17}	3.517±0.269
7.4×10^{13}		1.0×10^{13}	5.90×10^{17}	3.639±0.232
1.2×10^{14}	3.7×10^{17}	-	-	10.871±0.695
1.2×10^{14}		8.0×10^{12}	7.03×10^{16}	9.914±0.641
1.2×10^{14}		1.0×10^{13}	8.83×10^{16}	9.571±0.596
1.2×10^{14}		3.0×10^{13}	2.54×10^{17}	5.467±0.410
1.2×10^{14}		5.0×10^{13}	4.03×10^{17}	7.520±0.427
1.2×10^{14}		7.0×10^{13}	6.15×10^{17}	8.132±0.665

Another possible effect is *anomalous phosphorus diffusion*[5] [105–107] in silicon.

[5]Typically, Gaussian-shaped profiles will maintain its gaussian shape when broadening due to

For high phosphorus concentration, in an already implanted material with a heavy ion, and annealing in an oxidation environment phosphorus diffusion is enhanced and therefore a lower concentration of phosphorus (coincident with thallium) is induced. This implies that some of the thallium centres may not be compensated and absorption by thallium centres occurs. The values obtained for α_d are reported in Table 3.2.

3.3.3 Modeled Optical Loss

The modeled optical loss was obtained by solving eq.(3.1). In order to do so, the concentration profiles of thallium and phosphorus were calculated using the commercial software ATHENA© [108]. As an example, Figure 3.13(a) shows the active thallium in the waveguide cross-section after it was implanted with a thallium dose of 7.4×10^{13}ions/cm^2 and subsequently annealed for 90 minutes in dry O_2. Figure 3.13(b) shows the active phosphorus concentration profile after it was implanted with a phosphorus dose of 3×10^{12}ions/cm^2 and annealed for 90 minutes in dry O_2, and Figure 3.13(c) shows the net doping. ATHENA© does not support the modeling of thallium diffusion. However, the diffusivity coefficient of thallium is very close in value to that of indium. Therefore, by modifying the atomic mass and atomic number in the model for diffusion of indium to match the one for thallium, reasonable approximation for the thallium profile is obtained.

The concentration profiles for the implantation conditions summarized in Table 3.1 (only Tl dose 7.4×10^{13}cm^{-2}) are shown in Figure 3.14. It is noted that the maximum thallium concentration is limited by its solid solubility in silicon, represented by the

diffusion; however, phosphorus diffusion at high surface concentrations usually produces an electrical profile having a flat zone in the surface region, i.e., a zone where the electron concentration is constant, and is substantially lower than the phosphorus atomic concentration and exhibit a "kink" and "tail" for the lower-concentration part of the profile [103, 104].

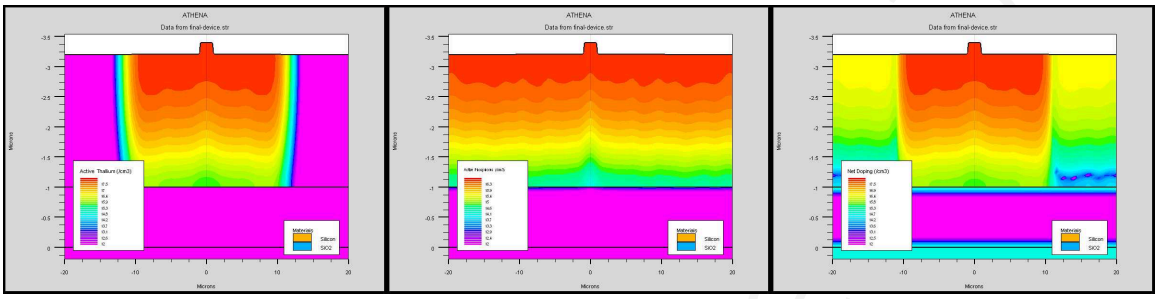

(a) (b) (c)

Figure 3.13: **Doping profiles obtained by ATHENA for (a) thallium dose of 7.4×10^{13}cm^{-2}, (b) phosphorus dose of 3×10^{12}cm^{-2} and (c) net doping.**

horizontal portion of the line indicating the thallium profile. All of the calculated profiles were exported into a Matlab© code to numerically solve eq.(3.10). The solution of this equation gives the Fermi energy level and the concentration of holes and electrons in their respective band. Introducing these results in equation (3.16) makes it possible to calculate the concentration of neutrally-charged thallium centres across the whole waveguide cross-section, required to solve the overlap integral in eq.(3.1). For example, Figure 3.15 shows the profiles of neutrally-charged thallium centres (continuous line) obtained for a thallium implantation dose of 7.4×10^{13}cm^{-2} and phosphorus dose of 10^{13}cm^{-2}. This concentration of neutrally-charged centres was calculated for the whole cross-section of the waveguide and overlapped with the corresponding waveguide mode of unit power.

Figure 3.16 shows the experimental data and its modeled absorption using the values of solid solubility and optical absorption cross-section. It is noted that a discrepancy exists between experimental and modeled absorption. However, if we consider solid solubility and optical absorption cross-section as fitting parameters, we observe that by increasing the value of the solid solubility there is a displacement of

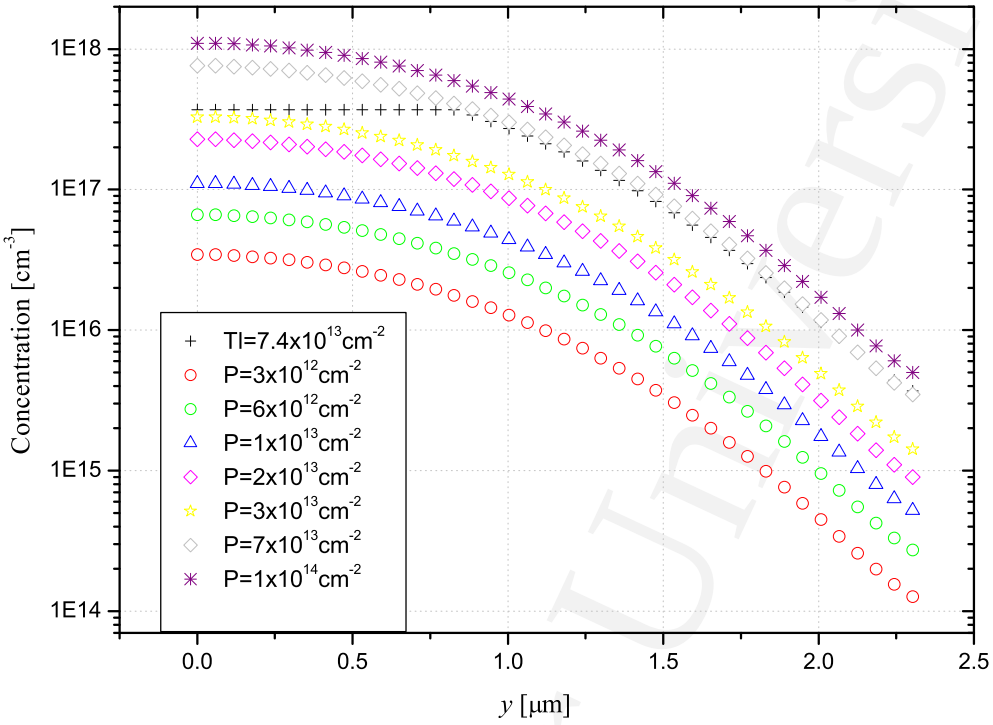

Figure 3.14: **Doping profiles for thallium and phosphorus for the data summarized in Table 3.1, obtained using the software ATHENA©.**

the thallium absorption-minimum to higher peak phosphorus concentration values. Alternatively, a change in absorption was observed when the optical absorption cross-section was allowed to vary as a fitting parameter. The value for the optical cross-section was increased meanwhile the solid solubility was kept constant. The best fitting value obtained for the optical absorption cross-section was $2.9\times10^{-17}\pm0.25\text{cm}^2$ for a thallium dose $7.4\times10^{-13}\text{cm}^{-2}$. Figure 3.17 reports the experimental data for thallium dose of $1.2\times10^{-14}\text{cm}^{-2}$ and the trend that the optical absorption would follow using the values of solid solubility and optical cross-section obtained from the

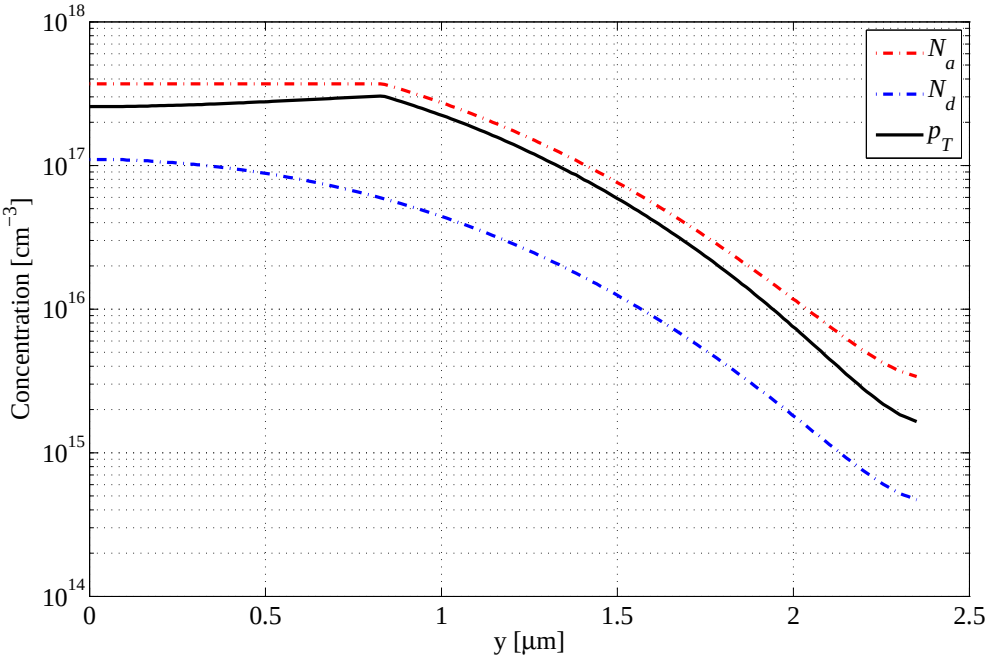

Figure 3.15: **Distribution of neutrally-charged centres, p_T, along the vertical direction as a function of the thallium concentration, N_a (dose 7.4×10^{13}cm^{-2}) and phosphorus concentration, N_d (dose 10^{13}cm^{-2}).**

literature, as well as the best fitting curve, whose optical cross-section is $3.2\times10^{-17}\pm 0.12$cm^2.

The modeling takes into account the free-carrier absorption within the implantation window as a consequence of the electrons and holes in each band. The free-carrier (FC) absorption was calculated by introducing the hole and electron concentrations in eq.(2.120) and using the result to calculate the overlapping integral of free-electrons and free-holes with the normalized optical waveguide mode. It is noted that free-carrier absorption is small for low phosphorus concentrations, and goes to its minimum when the concentrations are similar. However, it increases exponentially for concen-

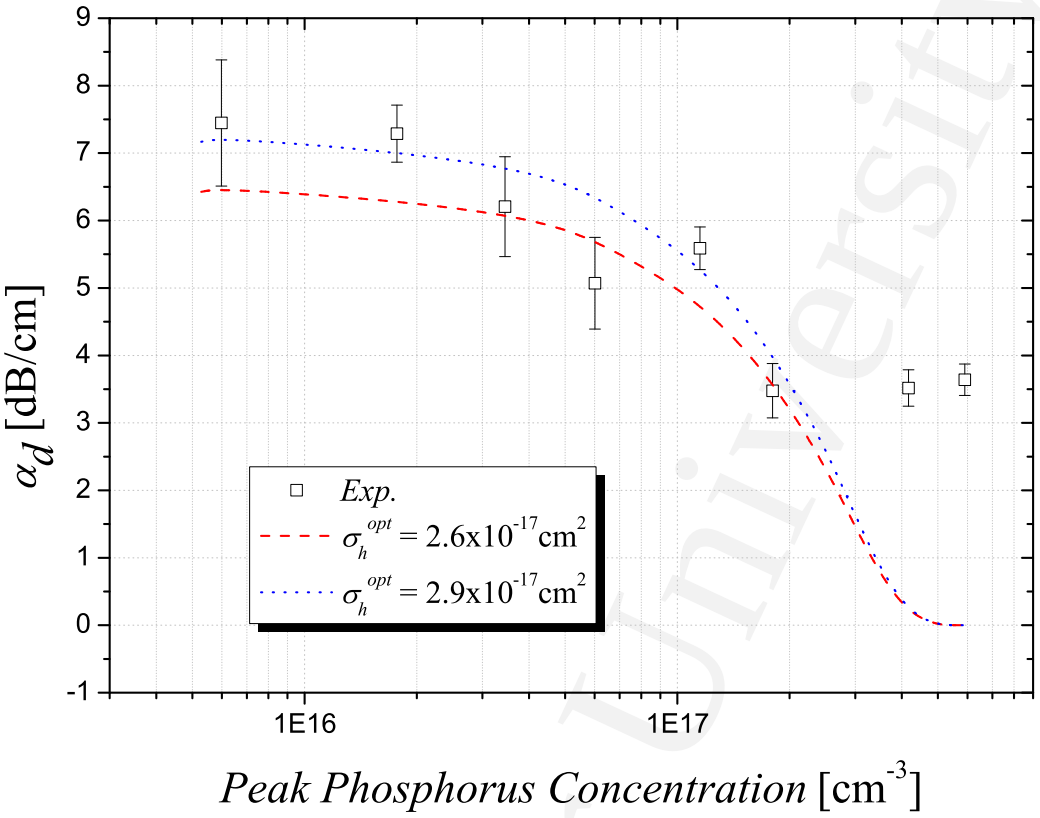

Figure 3.16: **Experimental and modeled absorption plotted as function of the peak phosphorus concentration for a thallium dose of 7.4×10^{13}cm^{-2}.**

trations that exceeds that of thallium. For low phosphorus concentration there is a small absorption and it is reduced to a minimum value when both concentrations are similar (compensation). However, free-carrier absorption increases exponentially for phosphorus concentration that exceed the concentration of thallium. It is noteworthy to mention that both thallium concentrations present the same "anomalous" behavior for the optical absorption for high phosphorus concentrations.

McMaster University

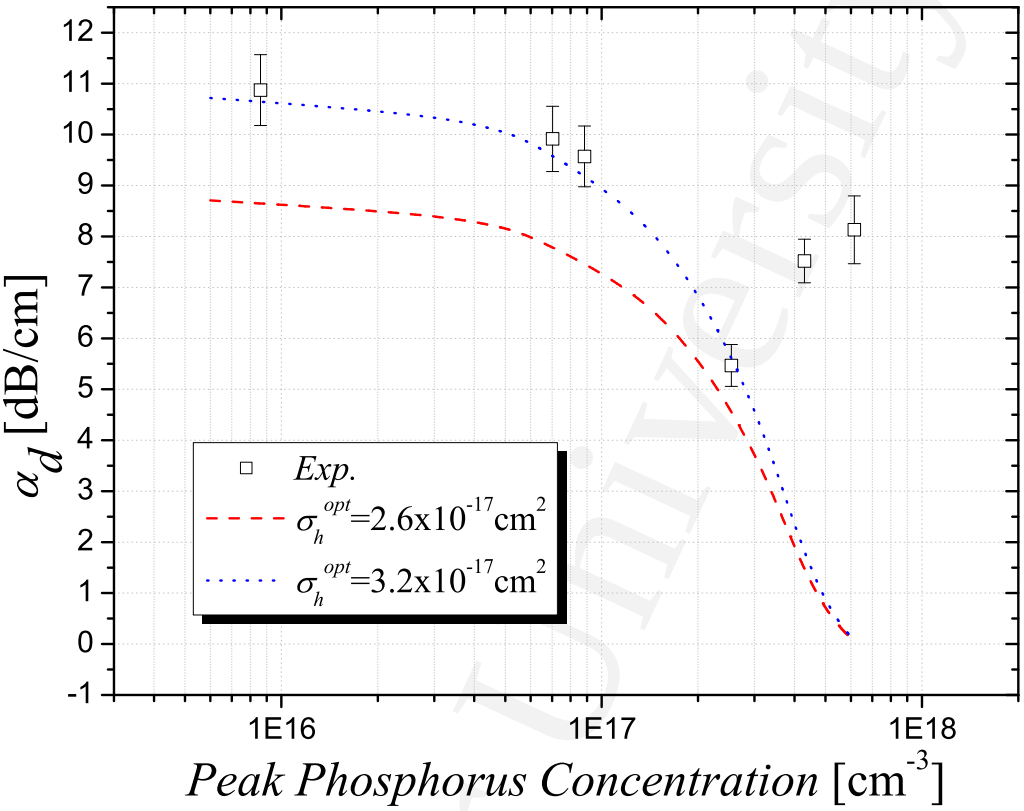

Figure 3.17: **Experimental and modeled absorption plotted as function of the peak phosphorus concentration for a thallium dose of 1.2×10^{14}cm^{-2}.**

3.4 Final Thoughts

In this chapter the effect of background doping type and concentration on the optical absorption of thallium centres (a deep level impurity) in silicon waveguides has been described theoretically and observed experimentally in order to discern its potential use in optical modulation in silicon waveguides. The relationship between the absorption strength of the thallium centres and their occupancy ratio was determined. Comparing the results here obtained with those ones reported using indium [40], it is know that indium is in fact a better candidate for optical modulation in silicon waveguides because it presents a higher absorption strength. The current model predicts

with high accuracy the behavior of the thallium centres for phosphorus concentrations that are smaller or equal to that of thallium. However, for higher phosphorus concentrations it may be necessary to consider the presence of other effects induced by high doping concentration in order to explain the residual absorption of thallium. Qualitatively, it is know that the diffusivity coefficient depends on the size of the impurity atom and on the concentration of the diffused impurity [105]. For example, the elastic interaction between a point defect and a dopant atom depends on the mismatch in size, so that a large dopant atom may prefer to migrate with a vacancy, while a small dopant atom may prefer to migrate with an interstitial [86]. Furthermore, it is known that phosphorus diffusion coefficient is enhanced when the surface of silicon is oxidized [103]. This implies that phosphorus prefers to diffuse with interstitials [86]. Following this idea, phosphorus diffusion is enhanced by injecting self-interstitials, resulting from the oxidation, which recombine with vacancies in the bulk, reducing the vacancy concentration and possibly retarding thallium diffusion. However, more studies are required to determine how well thallium incorporates in a silicon structure after a thermal process and the atomic interaction between thallium and phosphorus in a silicon substrate in order to determine the high absorption for phosphorus concentration exceed those for thallium concentration.

McMaster University

Chapter 4

Indium-Doped SOI Rib Waveguide Modulator

This chapter reports the design, simulation, fabrication and characterization of a single mode optical modulator based on the *charge state control of deep levels*[1] and the *plasma dispersion effect*. The device configuration discussed in this chapter is based on that proposed by *Li et.al.* [33] consisting of *pn-diode* structures perpendicular to the propagation direction of a SOI waveguide optical mode. Consistent with absorption results obtained for thallium doped silicon (Chapter 3) and the ones reported for indium doped silicon in *Logan et.al.* [40]. Indium was chosen to be used as the deep level impurity for the optical modulator. Periodic *pn-junctions* were made by implanting indium and phosphorus to form the *p-region* and *n-region* respectively. The device operates by injecting (forward-bias) or removing (reversed-bias) free-carriers in order to modulate the propagating signal. The presence of the deep levels and the configuration of the *pn*-junctions perpendicular to the propagation direction of the optical waveguide mode are intended to enhance the change in refractive index

[1] There is strong variation in absorption on 1550 nm wavelength via deep-level (indium, thallium) doping through the variation of background n-type doping

McMaster University

and absorption, and therefore the efficiency of the modulator compared to that of equivalent dimensions which rely on free carrier absorption effects alone.

4.1 Modulator Geometry

It is important to note that for all the configurations mentioned in section 1.3, the modulation efficiency depends greatly on how well the optical field and the carrier modulation region overlap. For this reason, great interest is focused on how the *pn*-junctions are arranged within the waveguide. Commonly, the *pn*-junctions are formed parallel to the beam propagation direction in such a way that the depletion region coincides with the maximum intensity of the waveguide mode, and the orientation of the *pn*-junction can be either horizontal or vertical with respect to the wafer plane. For example, in the carrier depletion modulator a vertically oriented *pn*-junction is employed, Fig. 1.2(b), where it is possible to recognize the partial overlap between intensity mode profile and the depletion region. A similar case exists for the carrier accumulation configuration, Fig. 1.2(c), where carriers accumulate on ether side for a vertically oriented oxide barrier, and only a portion of the intensity mode profile overlap with the accumulated charges. In order to increase the optical mode and the depletion region overlap, a new modulator structure has been proposed by Li *et.al* [33], Fig. 4.1a. In this structure the *pn*-junctions are periodically located along the waveguide, oriented perpendicular to the light propagation direction and vertically to the wafer plane, Fig. 4.1b. With this configuration the whole waveguide mode profile interacts with the depletion region instead of only a fraction of it, Fig. 4.1c. Since the optical mode passes through the successive depletion regions, the total optical modulation is calculated by multiplying the overlap ratio between the depletion region and optical waveguide mode, depletion region width and the total

McMaster University

number of *pn*-junctions along the waveguide.

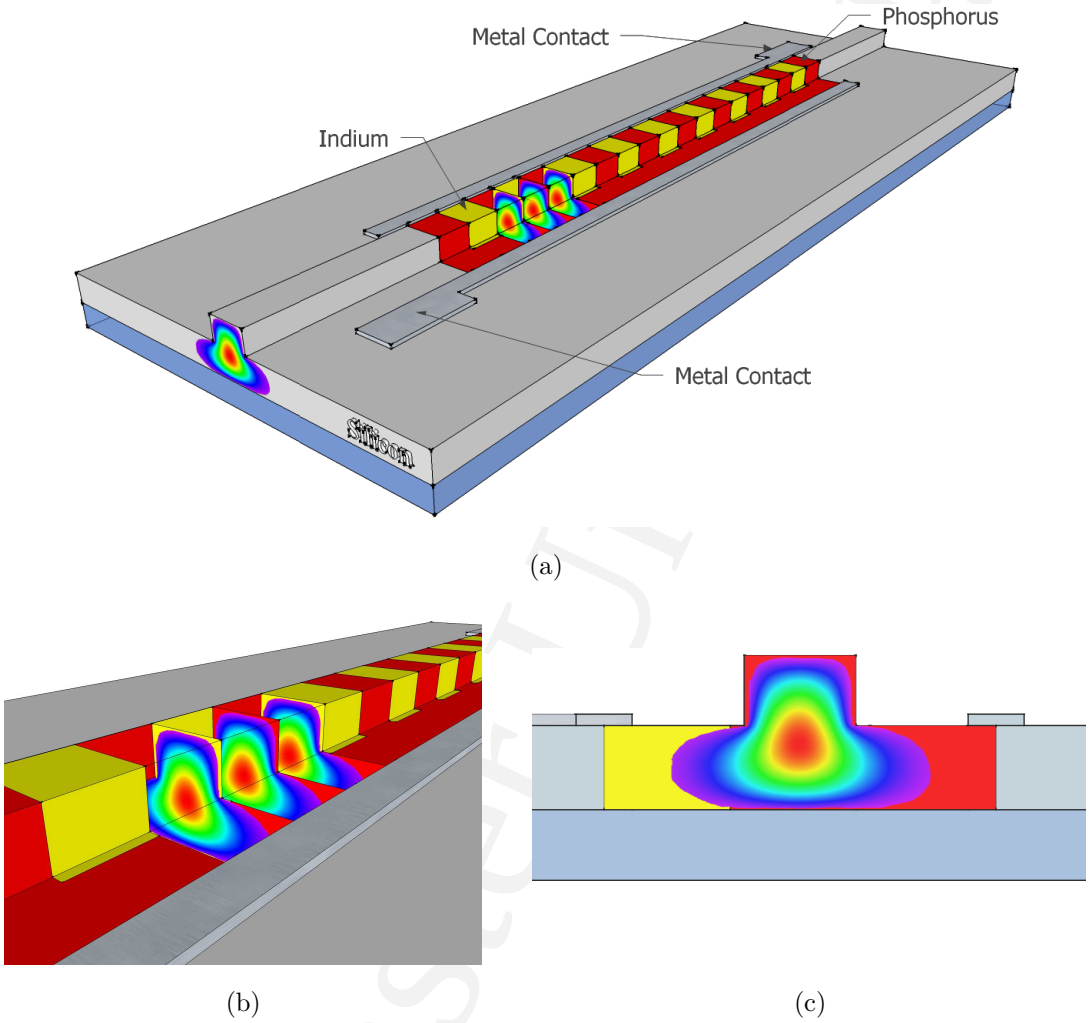

Figure 4.1: **Design of: (a) waveguide with periodic *pn*-junctions; (b) close-up of the interaction of the optical mode and the *pn*-junctions; and, (c) optical mode and *pn*-junction overlap.**

Indium is a group-III impurity, which makes it a p-type dopant in silicon with a single acceptor level at 0.157eV above the valence band [78, 109]. The optical excitation of an electron from the valence band to the neutrally-charged indium level has an optical cross-section, σ_p^{opt} of approximately $1.7{\times}10^{17}\text{cm}^2$ for a 1550nm wave-

length [40, 92]. For indium the capture cross-section for holes is approximately 8×10^{-15}cm^2 and for electrons 2×10^{-22}cm^2 [92]. The maximum indium doping that can be achieved is limited by its solid solubility in silicon which is approximately 1.5×10^{18}cm^{-3} [110] at room temperature.

The occupancy ratio for indium centres as a function of background phosphorus doping concentration is obtained by solving eq.(3.10)[2].

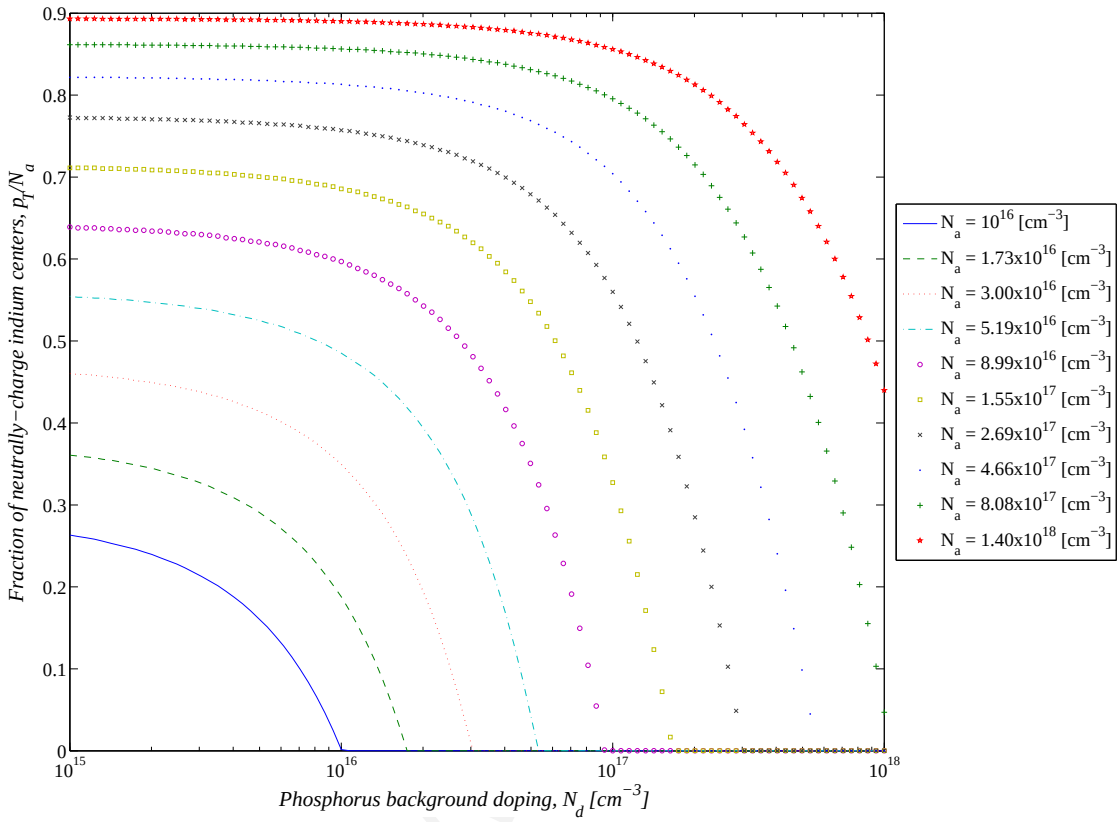

Figure 4.2: **Fraction neutrally-charged of indium centres, p_T/N_a as a function of phosphorus background doping without optical excitation.**

The fraction of neutrally-charged indium centres as a function of the phosphorus

[2]For simplicity in the calculations described in this chapter, I follow the same notation used in chapter 3 with the only difference that indium is the deep level

background doping concentration is plotted in figure 4.2. Comparing these results with the ones obtained for thallium (Fig. 3.5) at room temperature and for comparatively low concentrations of indium and phosphorus, relatively more centres are ionized (approximately 75% are occupied) with respect to thallium co-doped with phosphorus (approximately >40% are occupied). This difference in occupancy is assumed to be influenced by the proximity of the indium level to the valence band (more electrons are able to thermally make a transition from the valence band to the deep-level) and to the difference in hole capture cross-section which for thallium is approximately 10 time bigger than that of indium. Another observation is the maximum amount of neutral-charge centres for high concentrations of deep-levels as a function of low to medium phosphorus concentration. Whereas thallium shows >90% of centres neutrally-charged, indium has approximately <90% of neutrally-charged centres. These results may suggest that thallium is a better option for optical absorption in waveguide structures. However, experimental results of absorption measurements [40] tend to suggest the contrary. It is unclear why is this so but may be related to inaccurate reporting of optical cross section or second order effects such as doping cluster dynamics. Indium was thus chosen as the deep-level impurity in the modulator structures described here.

Figure 4.3 shows the capture rate for electrons and holes by the indium deep-level. The hole capture rate can be drastically changed by adjusting the phosphorus background concentration, for example from something around 10^{25} holes/cm^{3}s, for phosphorus concentration lower than the indium concentration, to less than 10^{15} holes/cm^{3}s for phosphorus concentration than exceeds that of indium.

The theory described in section 3.1.1 and section 3.2 is now applied to indium and is used to describe a modulation effect in silicon waveguides. Two mechanisms

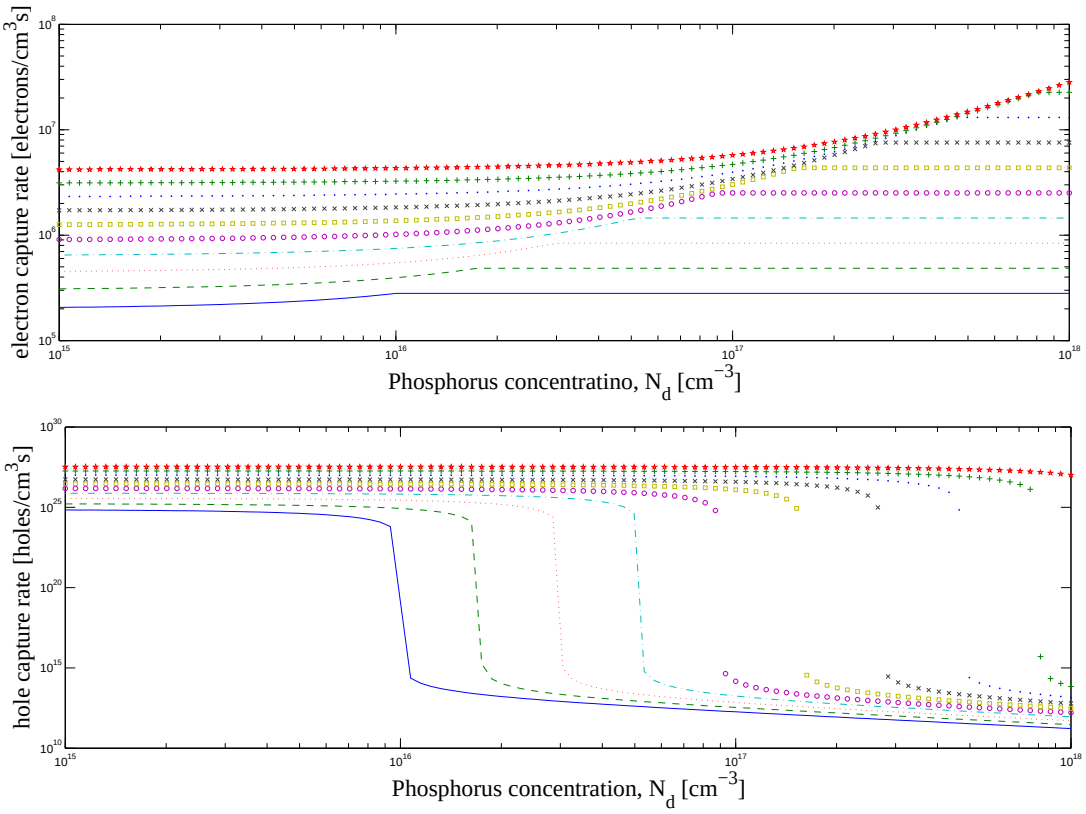

Figure 4.3: **Capture rate for electrons and holes for ten different concentration of indium (as in Fig. 4.2) as function of phosphorus background doping without optical excitation.**

are envisioned to produce optical modulation by varying p_T (neutrally-charged indium centres) over a large range to vary α_d (optical absorption by the deep-level), as described in eq.(3.1), known as *the depletion method* and *the injection method*.

4.1.1 Depletion Method

If a concentration of indium centres, N_a, is introduced into a silicon waveguide structure with a negligible background n-type doping, N_d (such as obtained via phos-

phorus doping[3]) such that $N_a \gg N_d$, eq.(3.13) implies that N_a^- shall be a small fraction of N_a (depending of how many indium centres are electrically activated) and α_d will be at a maximum. If a reversed bias is applied to the diode structure integrated with the waveguide, a depletion effect will be induced with the result that holes will be emitted from the indium centres, increasing N_a^- and decreasing the absorption coefficient to a minimum. Despite the fact that higher doping concentrations increase the change in the refractive index in the depletion region, a contrary effect is the reduction in the thickness of the depletion region for a given voltage. Thus, the overlapping length between the optical mode and the depletion region is decreased resulting in a modulator efficiency reduction. Therefore, this method is expected to be limited to relatively low doping concentrations ($\sim 10^{17}$ cm^{-3}).

4.1.2 Injection Method

If N_a indium centres are introduced into a silicon waveguide structure which is co-doped with shallow n-type donors to a concentration N_d, such as $N_d \geq N_a$, the indium centres would be fully compensated (as in the case (c) of Figure 3.2) with the result that $N_a^- = N_a$ so that minimum optical absorption occurs. Applying an electric field in forward bias (implying an excess of carriers) to the waveguide structure causes N_a^- to decrease due to the high difference between the capture rates[4] for electrons and holes and therefore enhances optical absorption. In this structure, in contrast to the typical *pin*-diode there is no intrinsic region; thus, the propagating optical mode would suffer more passive absorption due to the presence of deep-levels and free-carriers. However, "ideally" if both indium and phosphorus are equally distributed and have almost the same concentration ($N_d \cong N_a$) along the waveguide cross-section, indium centres should be fully compensated by the shallow donors and therefore

[3]In this research work we only used phosphorus as n-type doping
[4]For indium there is a high capture rate of holes.

optical absorption should be reduced to a minimum in an off-state[5]. Therefore, even for high doping concentration, there could be, in principle, a good optical intensity transmission as a result of the indium compensation by the phosphorus background doping. The practical challenge however with engineering a situation where $N_d = N_a$ is considerable.

4.2 Modulator Design

When designing an optical modulator there is a set of parameters that characterize the modulator and should be always considered depending on specification of operation. These are modulation speed (bandwidth), extinction ratio (modulation depth), device size (footprint), insertion loss, optical bandwidth and power consumption [24, 34]. Ideally, a silicon optical modulator should have high modulation speed and modulation depth, small footprint, low losses, large optical bandwidths, low power consumption and must also be CMOS-compatible. However, these requirements may impose contradictory requirements on the device design and compromises are often sought.

The structure here designed is based on a p^+pnn^+ diode on a silicon rib waveguide structure of width W, Fig.4.4(b)[6]. Periodically arranged pn-junctions are formed on the rib waveguide by implanting indium as the p-type and phosphorus as the n-type dopant. The implantation doses used in this study are reported in Table 4.2. Indium was implanted along the entire modulator length, L, on the waveguide structure and

[5]This means (without electric field), that there would not be indium levels available for optical absorption since some of (if not all) the free-carriers, introduced by the shallow donors, compensated this centres; while at the same time those compensating-carriers reduce the free-carrier concentration and therefore absorption to a minimum.

[6]Three widths were used; however, only the results obtained for 4μm width waveguides are reported. The rib waveguide etch depth is based on the single mode condition, shown in Figure 3.10.

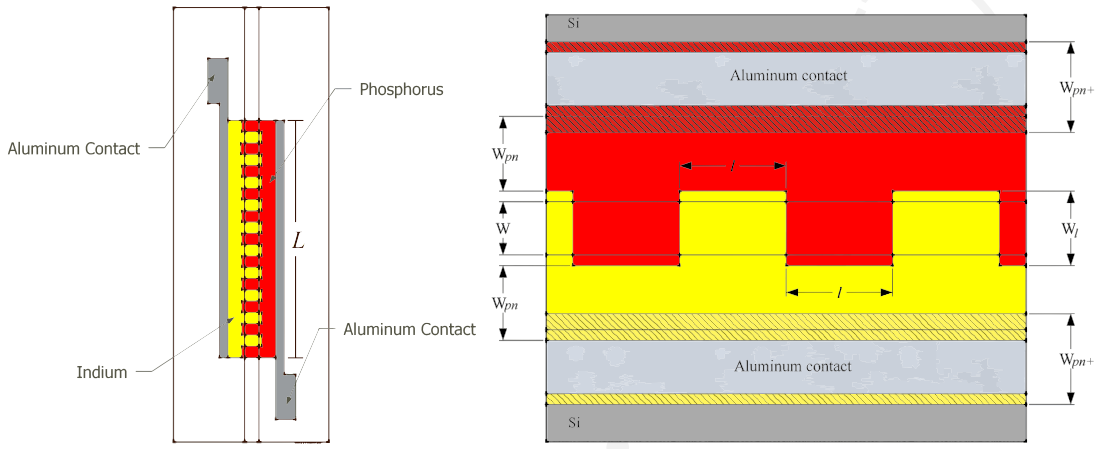

Figure 4.4: **Optical modulator diagram showing the periodically located pn-junctions with dimensions, (a) full device top view and (b) close-up view of the *pn*-junctions dimensions.**

phosphorus was subsequently introduced via a masked implantation, forming a comb shape on the rib waveguide, where its notches, of length l (duty cycle) and width W_l, overlapped with the region previously implanted with indium, Fig.4.4(b). The modulator lengths ranged from 0.25 mm up to 14 mm and the duty cycle length, l, was 1 μm, 2 μm, 3 μm or 4 μm. The use of these dimensions are more a choice due to the limitations of the photolithography system used for the fabrication rather than the optimal dimensions proposed by Li [33]. In that case, the authors chose the dimension of the duty cycle length as a function of the maximum depletion width obtained for a given dopant concentration and maximum bias voltage. In this study, the optimal dimension for W_l (Figure 4.4(b)) is approximately the one that matches the width of the waveguide mode. This work seeks to create *pn*-junctions, hence the phosphorus concentration is required to exceed the concentration of indium for

the co-doped regions[7]. Highly doped n^+ and p^+ regions of width W_{pn+} (introduced via ion implantation to doses of 10^{15}cm^{-2} that produce volume concentrations of $> 5 \times 10^{18}\text{cm}^{-3}$), are separated from the rib by a distance of W_{pn}, that contain the same doping concentration used for the p- and n-regions. This separation is to avoid excess loss as a result of the overlap between the optical waveguide mode and the highly doped regions. Boron was used as a dopant for the p^+ region. The metal contacts (made of aluminum) overlap with the p^+ and n^+ regions. Figure 4.4(a), shows the top view of the modulator where the pn-junctions on the waveguide, the $p-$, $n-$, p^+ and n^+ regions and the aluminum contacts are identified. The modulator dimensions are summarized in Table 4.1 and its layout on the photolithography mask is shown in appendix B.

4.3 Device Simulation

The electrical and optical performance of the optical modulator were modeled by using a two dimensional device simulator obtained from SILVACO [108] (in particular *Athena*© and *Atlas*© modules) and the optical simulator BeamPROP© from RSoft [111], respectively. The use of the software *Athena*© from SILVACO is based on the necessity to find the fabrication conditions to obtain a homogeneous doping along the waveguide cross-section in order to ensure a complete overlap between waveguide mode and doping profiles. With the fabrication conditions established (implantation doses, annealing temperatures and annealing times), the concentration profiles were calculated for all the samples. For example, Fig.(4.5) shows the concentration profile obtained for a sample doped with an indium dose of $5\times10^{13}\text{ions/cm}^2$, and in particular the concentration profile along $y(x = 0)$ and $x(y = 0.75\mu m)$. These concentration

[7]In order to have a higher concentration, phosphorus dose was chosen to be three times higher than indium.

McMaster University

Table 4.1: **Dimensions for the Indium modulators that correspond to the PL-mask shown in appendix B**

...	W [μm]	W$_{pn}$ [μm]	W$_{pn+}$ [μm]	l [μm]	W$_l$ [μm]	L [μm]	...	W [μm]	W$_{pn}$ [μm]	W$_{pn+}$ [μm]	l [μm]	W$_l$ [μm]	L [μm]
1	4	-	-	-	-	-	21	4	7		1	6	12000
2	3	8		1	5	10000	22	4	7		1	6	10000
3	2	8		1	4	10000	23	4	7		1	6	8000
4	4	8		3	7	13000	24	4	7		1	6	6000
5	4	8		3	7	9000	25	4	7		1	6	4000
6	4	8		3	7	5000	26	4	7		1	6	2000
7	4	8		3	7	3000	27	4	7		1	6	1000
8	4	8		3	7	1500	28	4	7		1	6	500
9	4	8		3	7	800	29	4	7		1	6	250
10	4	8		3	7	600	30	4	7	20	1	7	600
11	4	7	20	2	7	250	31	4	8		4	7	800
12	4	7		2	7	500	32	4	8		4	7	1500
13	4	7		2	7	1000	33	4	8		4	7	3000
14	4	7		2	7	2000	34	4	8		4	7	5000
15	4	7		2	7	4000	35	4	8		4	7	9000
16	4	7		2	7	6000	36	4	8		4	7	13000
17	4	7		2	7	8000	37	2	8		2	4	10000
18	4	7		2	7	10000	38	3	8		2	5	10000
19	4	7		2	7	12000	39	4	-	-	-	-	-
20	4	7		1	7	14000	-	-	-	-	-	-	-

McMaster University

profiles are used to analyze the modulator performance by employing the parameters that describe (section 2.10) the change in refractive index and absorption coefficient in silicon, induced by the free electron and hole concentrations.

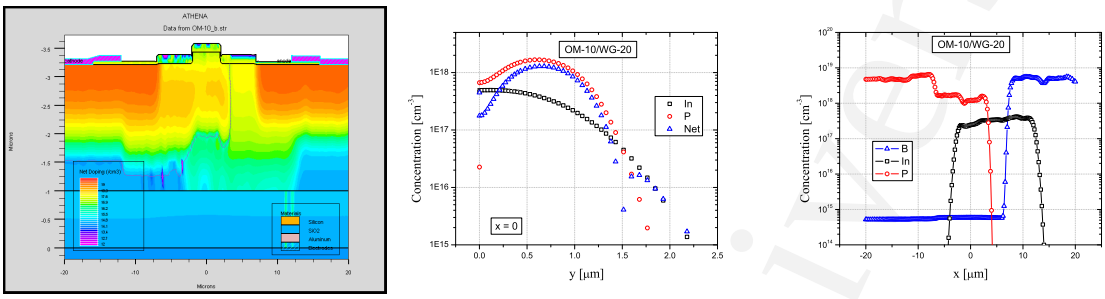

(a) (b) (c)

Figure 4.5: **Doping profiles obtained with ATHENA© for (a) for the sample OM-10, (b) doping concentration profiles along $y(x = 0)$ and (c) doping concentration profiles along $x(y = 0.75\mu m)$.**

Figure 4.6 shows the *current-voltage* characteristic obtained from the simulation package ATLAS©, from SILVACO, in forward and reverse bias for all the doping concentrations used. From the plots the rectifying effect associated with a diode structure is established.

The calculation of the local variation of the effective index of refraction $\Delta n_{eff}(z)$ and absorption coefficient $\Delta\alpha_{eff}(z)$ can be deduced by using the overlap integral between the optical mode and the refractive index and the absorption coefficient, eq.(4.1) and eq.(4.2) respectively:

$$\Delta n = -8.8 \times 10^{-22} (\Delta N_e) - 8.5 \times 10^{-18} (\Delta N_h)^{0.8} \tag{4.1}$$

$$\Delta\alpha = 8.5 \times 10^{-18} (\Delta N_e) + 6.0 \times 10^{-18} (\Delta N_h) \tag{4.2}$$

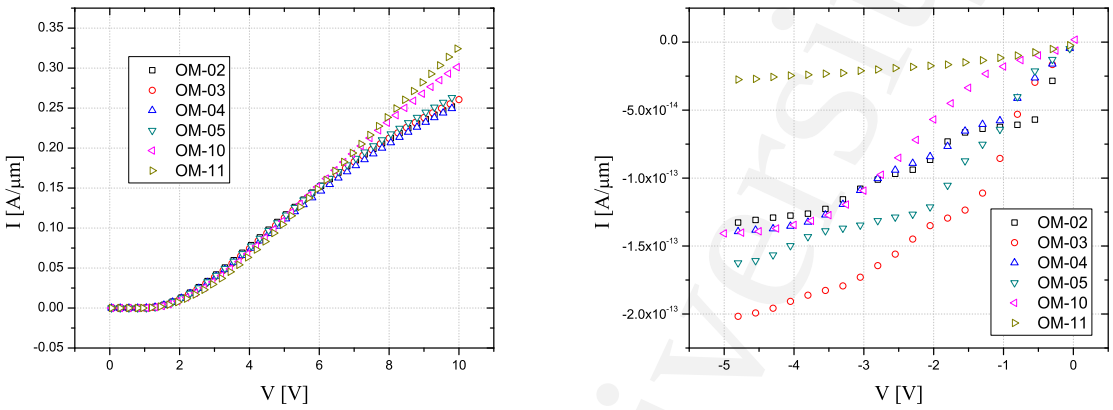

(a) Forward Bias (b) Reverse Bias

Figure 4.6: **I-V curves simulated with Silvaco for all devices summarized in Table 4.2 in (a) Forward bias and (b) Reversed bias.**

such that

$$\Delta n_{eff}(z) = \iint_{x,y} \Phi(x,y)\Delta n \, \mathrm{d}x \, \mathrm{d}y \tag{4.3}$$

$$\Delta \alpha_{eff}(z) = \iint_{x,y} \Phi(x,y)\Delta \alpha \, \mathrm{d}x \, \mathrm{d}y \tag{4.4}$$

where x and y are the coordinates in the waveguide cross-section and $\Phi(x,y)$ is the normalized (unit power) optical waveguide mode profile. The phase shift per unit length $\Delta\phi\,[\pi/cm]$ and the free carrier absorption loss $\Delta\alpha_{fc}\,[dB/cm]$ can be calculated by integrating over a length $2l$ of the periodic pn-junction configuration.

$$\Delta\phi = \frac{2\pi}{2l\lambda} \int_0^{2l} \Delta n_{eff}(z) \, \mathrm{d}z \tag{4.5}$$

$$\Delta\alpha_{fc} = \frac{4.343}{2l}\int_{0}^{2l}\Delta\alpha_{eff}(z)\,\mathrm{d}z \tag{4.6}$$

The p-region, in the periodically arranged pn-junctions, was formed by only implanting indium, hence free charge-carriers (free-holes) and neutrally-charged concentration of deep-levels are responsible for the optical absorption in that particular region. The n-region was formed by masked implantation of phosphorus in the regions already doped with indium so that the phosphorus over-compensates the indium. Therefore, the optical absorption in the n-region will be proportional to the availability of neutrally-charged deep-levels (which for this region is always negligible) and the free-charge carrier concentration (the dominant effect). The calculation of the concentration of free-carriers and the concentration of neutrally-charged deep-levels was done by using equations described in sections 3.2.2. Figure 4.7(a) shows the concentration profile simulated with the software Athena© for sample a sample doped with an indium dose of 5×10^{12}ions/cm^2, where the phosphorus doping was implanted every $1\mu m$ in windows of $1\mu m$ width. Since the indium concentration can be considered constant along z and the phosphorus concentration varies along z, Figure 4.7(b), the concentration of neutrally-charged deep-levels and the concentration of free-carriers in a xy-plane, perpendicular to the propagation direction, for specific z-position in a $2l$ distance, as a function of the indium and phosphorus concentration was calculated.

The refractive index variation was determined by calculating the concentration of free-carriers, as a function of phosphorus concentration, indium fraction and occupancy concentration of deep-levels.

Figure 4.8(a) shows the optical absorption by neutrally-charged indium centres,

McMaster University

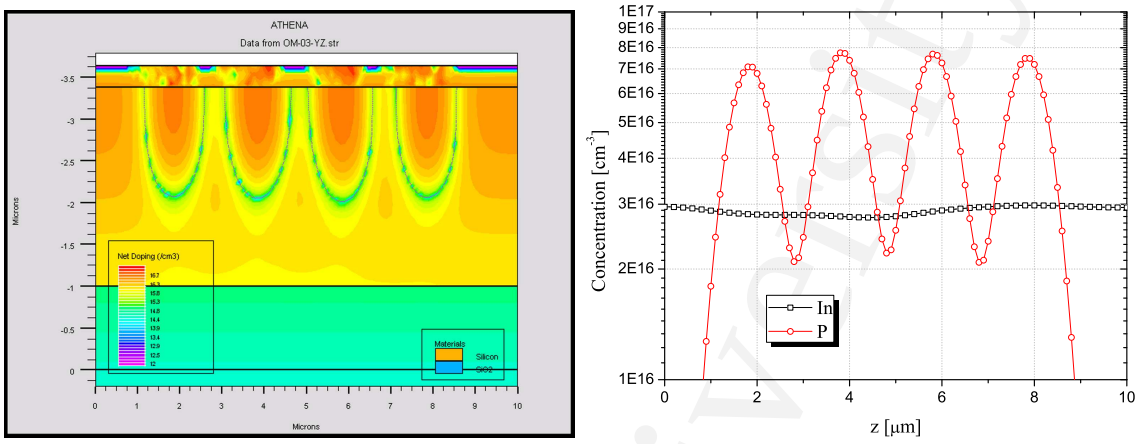

(a) Simulated profile

(b) Concentration profile

Figure 4.7: **(a) Cross-section of the doping concentration simulated with Athena© along plane *yz* for the sample OM-03, showing the periodicity of the *pn*-junctions as a result of phosphorus doping of selective regions (every 1μm) on the waveguide; (b) phosphorus and indium concentration profiles.**

α_d, along z. The six different indium implantation doses[8] used for the simulations are specified in each plot, and the corresponding phosphorus implantation doses were three times those for indium, for example for an indium implantation dose of 3×10^{12}ions/cm^2 a phosphorus implantation dose of 9×10^{12}ions/cm^2 was used. This absorption was calculated using eq.(3.1), and its higher calculated value corresponds to the region where there is no phosphorus concentration, and therefore there is the highest concentration of neutrally-charged centres. Figure 4.8(b) shows the optical absorption by free-carriers. It is known that the presence of phosphorus will compensate the indium deep-levels. Therefore, when the concentration of phosphorus begins to increase with respect to the indium concentration, the optical absorption by

[8]These doses are the same used in the fabricated samples, which are summarized in Table 4.2.

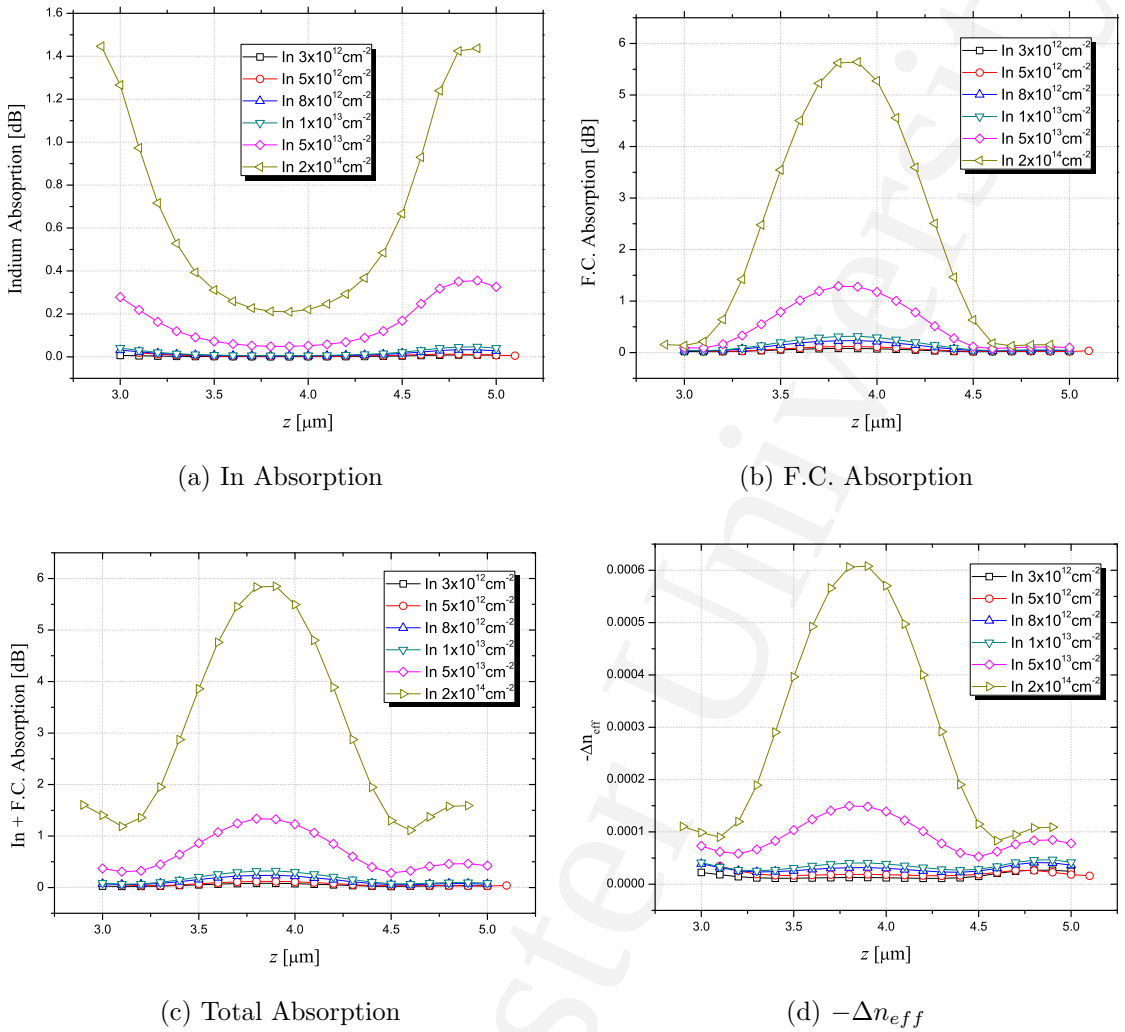

(a) In Absorption

(b) F.C. Absorption

(c) Total Absorption

(d) $-\Delta n_{eff}$

Figure 4.8: **Simulation results for $1\mu m$ duty cycle, (a) optical absorption by neutrally-charged indium deep-levels; (b) optical absorption by free charge carriers; (c) total optical absorption and (d) change in the effective refractive index.**

indium deep-levels begins to be suppressed until a minimum value for α_d is reached when the phosphorus concentration exceeds, by far, that of indium, Fig. 4.8(a). The dominant optical absorption is then by free-charge carriers, since virtually all of the indium deep-levels will be compensated; however, there will always be a residual

absorption by indium deep-levels, as evidenced by the results of simulations, in particular the results obtained for an indium implantation dose of $2 \times 10^{14}\text{cm}^{-2}$. The total optical absorption is due to the contribution of both types and can be represented by $\alpha_{tot}(z) = \alpha_d + \Delta\alpha_{eff}$, this expression replace the term $\Delta\alpha_{eff}$ in eq.(4.6) in order to calculate the total change in absorption along a $2l$ distance, eq.(4.7).

$$\Delta\alpha_{tot} = \frac{4.343}{2l} \int_0^{2l} \alpha_{tot}(z)\, \mathrm{d}z \tag{4.7}$$

Figure 4.8(d) shows the change in refractive index as a function of the free-charge carriers concentration, the maximum reduction in index of refraction corresponds to the maximum phosphorus concentration, as it was expected. All these results are calculated for the optical modulator in an off-state.

The effect of the duty cycle length on the total optical absorption was analyzed and the simulated results, in particular for an indium dose of $5 \times 10^{13}\text{ions/cm}^2$, are presented in Figure 4.9. The simulation results suggest that the optical absorption per unit length is dependant of the implantation windows duty cycle (l). This means that a waveguide modulator with longer duty cycle length presents higher optical absorption in an off-state, as can be observed in the Figure 4.9. The explanation for a reduction in absorption for the smaller duty cycle length is due to *the shadowing effects*, introduced by the thick photoresist used as a masking layer. In the simulations (and in the fabrication) the photoresist used was $4\mu m$ thick and the implantation beam was tilted at 7° respect to the surface normal[9], Figure 4.10(c). This implies that for narrow implantation windows the shadowing effect by the photoresist is higher, and therefore limits the amount of ions that are implanted into the silicon. This shadowing loss produced by the photoresist could in future be reduced by rotating

[9] On a yz-plane.

McMaster University

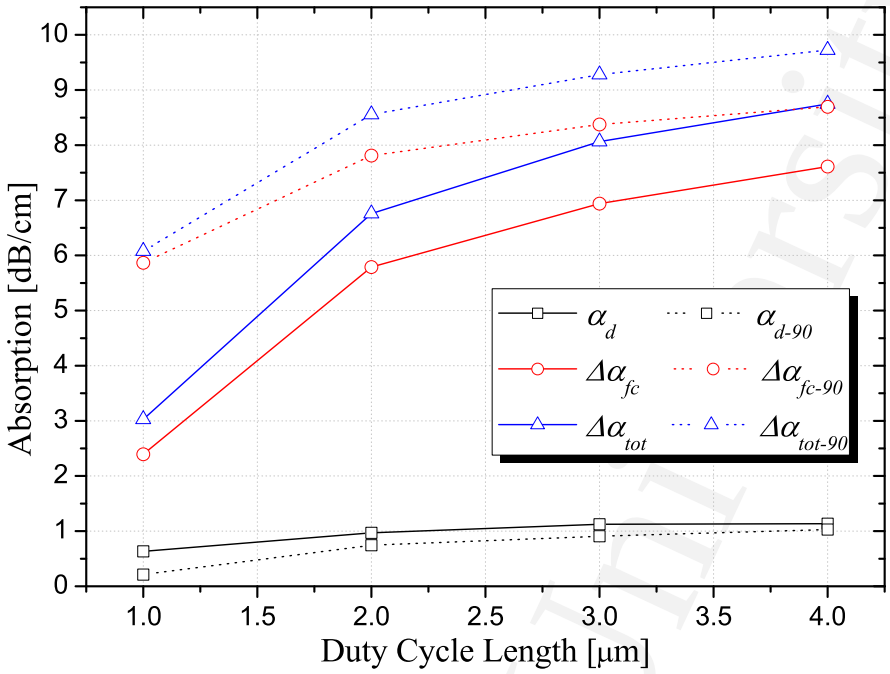

Figure 4.9: **Optical absorption for an indium dose of 5×10^{13}ions/cm^2 as a function of the duty cycle length with shadowing loss (solid line) and when the shadowing loss is minimized (dotted line).**

the sample such as that the ion beam is parallel to the photoresist walls of the ion implantation windows (on a *xy*-plane, Figure 4.10(d)).

Figure 4.9 (dotted line), shows the simulated results obtained for a modulator that is rotated such as the shadow effect is removed. It is noted that the absorption by free-carriers is greatly increased for the modulators with the smallest duty cycle length. This suggest that the shadowing effect by the masking photoresist is minimized. In contrast the absorption by deep-levels is reduced, in part due to the presence of more phosphorus ions but at the same time by the lateral diffusion of phosphorus during thermal annealing, which narrows the regions which contains only indium,

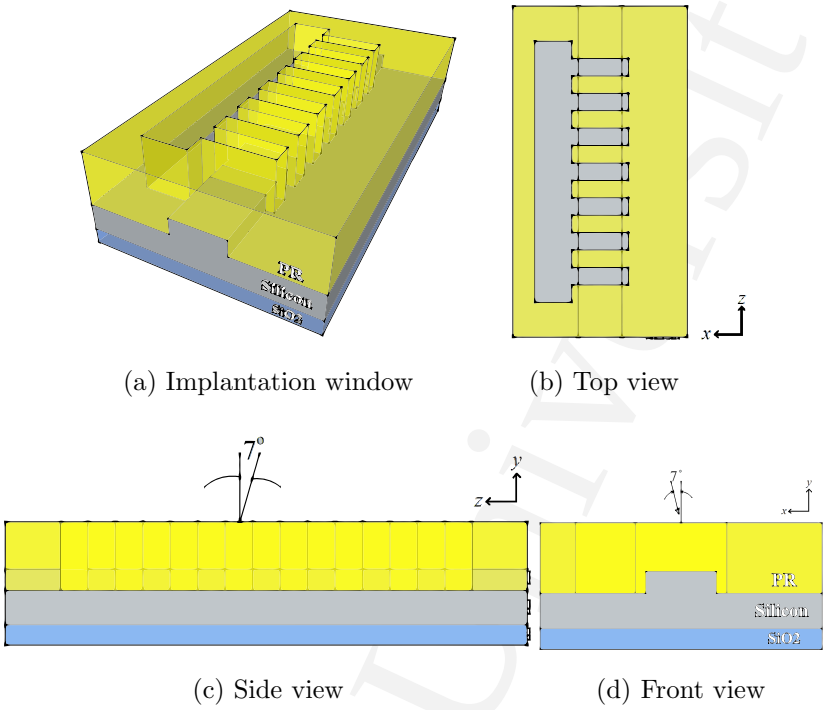

(a) Implantation window (b) Top view

(c) Side view (d) Front view

Figure 4.10: **Illustration of the phosphorus implantation window (a).**

and therefore the absorption by deep-levels.

4.4 Fabrication

Devices were fabricated in a Silicon-On-Insulator wafer with a 2.5μm thick silicon overlayer with a 0.375μm thick buried oxide (BOX). Samples of 2×2cm^2 were cleaved and cleaned using the RCA cleaning procedure, in order to ensure a clean surface before the fabrication process, step 1 in Fig.4.11. A 100μm thick thermal-oxide layer was grown, in an oxygen environment at 1100°C for 30 minutes [73], step 2 Fig.4.11. *Shipley photoresist 1808* was spun at 4200rpm for 30 seconds and *soft-baked* on the hot-plate at 110°C for 2 minutes, Fig.4.11 step 3. Samples were transferred to the mask-aligner equipment and exposed using standard photolithography. They were

developed in a solution 5:1 of deionized water (DI-H_2O) and Developer 351 for ∼30 seconds or until the transferred pattern is completely developed. Optical inspection with an optical microscope was necessary in order to check the integrity of the pattern, Fig.4.11 step 4. If the pattern was deemed satisfactory, the samples were *hard-baked* on the hot-plate at 130°C for two minutes. The PR pattern was transferred to the oxide by submerging the sample (previously placed in a teflon basket) in a 10% BHF solution and gently stirring the teflon basket for ∼1 minute continuously, or until the uncovered oxide was etched, and rinsed in DI-H_2O for ∼5 minutes to ensure that all the BHF was washed away. Samples were dried using a N_2 gun, and the PR mask was removed, Fig.4.11 step 6. Samples were rinsed in DI-H_2O and dried, and placed under the optical microscope to check the quality of the oxide pattern. The oxide pattern was used as an etching mask to transfer the waveguide shape to the silicon overlayer. This was done by using *Potassium hydroxide* (KOH) wet etching technique [112–114]. Before etching silicon, the oxide mask thickness was measured in each corner and the centre of the sample to enable its use as a reference for the silicon etch depth. A 40% KOH-IPA solution was prepared and heated to 75°C, where an etching ratio of ∼10.7nm/s was expected, Appendix A. The etching set-up was prepared by heating water in a glass container (water-bath) to the desired temperature and bringing in a smaller beaker with the 40% KOH-IPA solution in it. When the KOH-IPA solution reached the water-bath temperature, samples in a teflon basket were introduced for the time required to achieve etching of the rib waveguide. Samples were removed from KOH solution, rinsed in DI-H_2O and dried with N_2, Fig.4.11 step 7. Samples were transferred to an alpha-stepper and the amount of silicon etched was measured. If the specified silicon etch depth was reached, the oxide mask was etched away with the help of BHF, step 8. When all oxide were removed, samples were rinsed in DI-H_2O and dried in N_2. All samples were inspected under the optical microscope and

McMaster University

classified according to their quality.

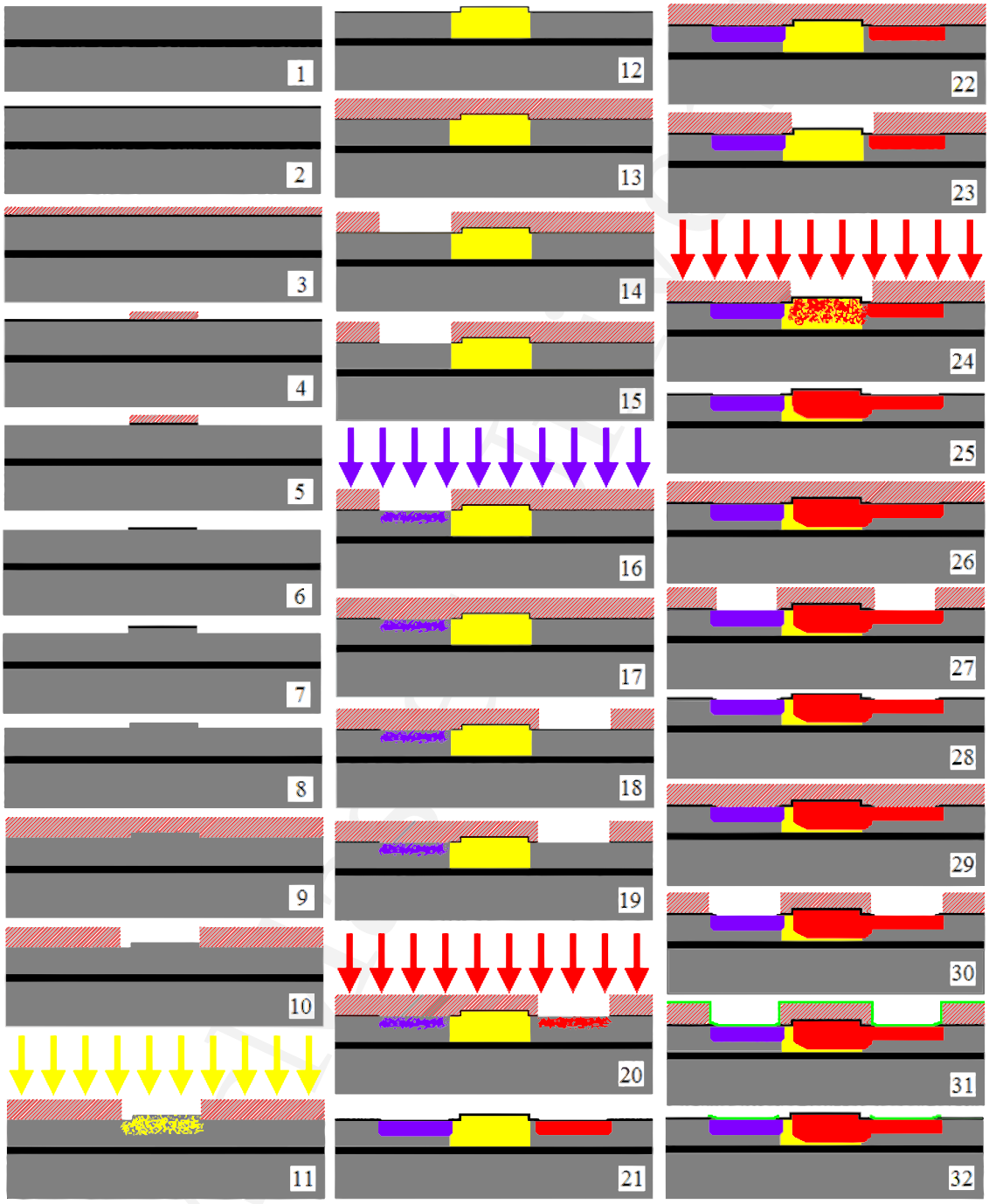

Figure 4.11: **Fabrication steps for the indium modulator, explained in text.**

A *Shipley photoresist 1827* (thick PR) was spun on top of samples at 2200rpm for 30 seconds which produced a $\sim 4\mu$m thick PR. Samples were soft-baked at 100°C on a hot-plate for two minutes, Fig.4.11 step 9. They were exposed with the implantation windows aligned with respect to the waveguides, developed for ∼30 seconds rinsed and dried. The quality of implantation windows was inspected with the optical microscope, Fig.4.11 step 10. The samples were hard-baked at 120°C for two minutes and transferred to the *Tandetron Accelerator System* (in University of Western Ontario) for indium implantation. Indium was implanted with an energy of 1MeV which produced a projected range of ∼440nm [115] and doses were summarized in Table 4.2, Fig.4.11 step 11. After implantation, PR was removed using acetone in a ultrasonic bath until all PR peeled off. They were rinsed in IPA, followed by DI-H_2O and dried. Since indium is a heavy ion and it does not diffuse easily in silicon, high temperature and long annealing time were required in order to diffuse the ions as deep as possible to produce a homogeneous concentration along the waveguide cross-section. Therefore, samples were annealed for 90 minutes at 1100°C in an oxygen environment, Fig. 4.11 step 12.

Again *PR S-1827* was deposited, exposed and developed to define the boron implantation windows that corresponded to the p^+ contact, step 14. The distance between implantation window and waveguide was chosen in order to avoid an overlap between the optical mode and the highly-doped contact region. Low energy (shallow) implantation was performed using the *McMaster University implanter* for the electrical contacts. These regions require a high-concentration of boron (corresponding to an implantation dose of 10^{15}cm^{-2}), step 16 in Fig.4.11. Before implanting boron, care was taken to remove all oxide from the implantation window. After boron implantation was carried out, PR was removed, and the samples cleaned. *Photoresist S-1827* was deposited, exposed and developed (using the same conditions described

Table 4.2: **Summary of In and P implantation conditions for the SOI waveguide modulator**

	Indium				Phosphorus			
			Annealing				Annealing	
Sample	Dose [cm^{-2}]	Energy [keV]	Temp. [°C]	Time [min]	Dose [cm^{-2}]	Energy [keV]	Temp. [°C]	Time [min]
OM-02	3.0×10^{12}	1000	1100	90	2.25×10^{12}	350	1100	10
OM-03	5.0×10^{12}				3.70×10^{12}			
OM-04	8.0×10^{12}				6.0×10^{12}	550		
OM-05	1.0×10^{13}				7.50×10^{12}	750		
OM-10	5.0×10^{13}				3.75×10^{13}	1000		
OM-11	2.0×10^{14}				1.50×10^{14}			

before) to define the phosphorus implantation windows that corresponded to the n^+ contacts, step 20. Again all oxide was removed in order to ensure that all the ions were implanted in silicon. Shallow phosphorus implantation was performed using the *McMaster University implanter* with an energy of 30keV and dose of $10^{15}cm^{-2}$. After implantation, all the PR were removed and samples cleaned. Then, all samples were thermally annealed using a Rapid Thermal Annealer (RTA) for 10 minutes at 1100°C in an oxygen environment, Fig. 4.11 step 21.

Looking for a benchmark against which to compare the indium modulator, some of the samples were implanted with a more traditional p-type impurity, boron. The fabrication procedure is essentially the same as described previously with the exception of a difference of the implantation energies and annealing temperatures and

McMaster University

times. Fabrication conditions are summarized in Table 4.3.

Table 4.3: **Summary of B and P implantation conditions for the SOI waveguide modulator**

	Boron				Phosphorus			
			Annealing				Annealing	
Sample	Dose [cm^{-2}]	Energy [keV]	Temp. [°C]	Time [min]	Dose [cm^{-2}]	Energy [keV]	Temp. [°C]	Time [min]
OM-01	7.5×10^{12}	30	1050	90	5.0×10^{12}	350 550	1050	10
OM-06	1.75×10^{13}				1.30×10^{13}			
OM-08	2.5×10^{13}				1.88×10^{13}	750 1000		

For the implantation of phosphorus within the waveguide *Photoresist S-1827* was used as a masking layer in a manner identical to that used for the indium implantation. Using the *Tandetron Accelerator System*, samples were implanted with phosphorus with energies and doses summarized in Table 4.2, step 24. This implantation window has a comb-type shape, where the notches overlap with the waveguide region previously implanted with indium such that multiple *pn-junctions* are defined along the rib, described schematically in Fig. 4.4. Four different energies were used in a multiple energy process, in order to obtain a homogeneous concentration through the waveguide cross-section, step 24. Photoresist was removed from the samples with acetone in an ultra-sonic bath. They were then rinsed, dried and thermally annealed using the RTA for 10 minutes at 1100°C in an oxygen environment, Figure 4.11 step 25.

After the electrical activation of the dopants, *PR S-1827* was deposited in order

McMaster University

to define the *via* windows. These are small openings in the insulating oxide layer that allow a conductive connection between the heavily doped regions and metal layer that defines the electrical contacts, step 27. Photoresist was removed from the sample and cleaned to prevent possible particles that could affect subsequent deposition of *PR S-1827*. The PR was exposed and developed in order to define the metal contact region. An aluminum layer of ∼150nm was deposited on top of the samples by a metal sputtering system and a *lift-off* process followed, defining the metal contact pattern, steps 31-32.

Contact anneal[10] at 475°C for 10 minutes in a N_2 environment was required to reduce contact resistance at the aluminum-silicon interface [117]. Care was taken not to exceed 580°C because at this temperature the *Al* softens and consumes some of the silicon below forming a silicide [79].

The final step in the sample preparation was the definition of optical quality end-facets using a chip thinning and edge cleaving process.

4.5 Experimental Results and Discussion

Optical, electrical and transient measurements were performed using the set-up shown in Figure 4.12. Current-Voltage (I-V) curves were measured using a HP4145A Semiconductor Parameter Analyzer (SPA) and the electrical contact probes, model 7x from Micromanipulator Company. The transient measurements were performed using the HP54600A Oscilloscope with a maximum bandwidth of 100MHz, connected to an InGaAs photodetector from Thorlabs with a maximum bandwidth of 17Mhz (for 0 dB setting). The electrical signal fed to the modulator was generated by

[10] At elevated temperatures, aluminum will "take" the oxygen away from the SiO_2 at the interface to form Al_2O_3. This aluminum oxide is then incorporated into the bulk of the aluminum, leaving the interface free of oxide [116].

McMaster University

the HP8082A Pulse Generator. Optical measurements were carried out following a similar procedure as the one specified in section 3.3.2.

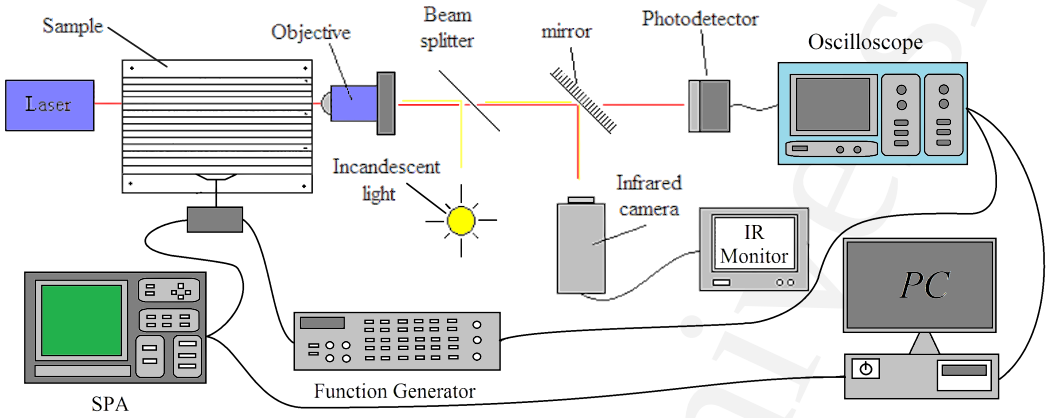

Figure 4.12: **Experimental set-up used for the optical and electrical measurements and transient response of the modulator.**

Optical power transmission measurements were performed for every waveguide in each sample. A representative fraction of the results are reported in figure 4.13 as optical power versus modulator length. A linear fitting is presented with the simple intention to make evident the previous comments regarding compensation of indium by phosphorus background doping. Sample OM-02 (the sample with the lowest doping concentration in our study, not shown here) was damaged during fabrication, such that the modulators with the shortest length were the only ones possible to measure. The linear fitting corresponding to these values presents a positive value (implying optical gain); however, this behavior-should be viewed sceptically due to the small amount of data. Samples with medium to high doping concentration present a linear fitting with small negative slopes. This slope implies that the indium levels are compensated by phosphorus, reducing the availability of neutrally-charged indium centres and free electrons to absorb light. Therefore, the absorption losses induced

by doping impurities in the optical modulator are reduced in an "off-state". Samples with higher doping concentration present a linear fitting with a more severe negative slope with the extreme case of sample OM-11, for which light transmission was only possible for modulators with the shortest length.

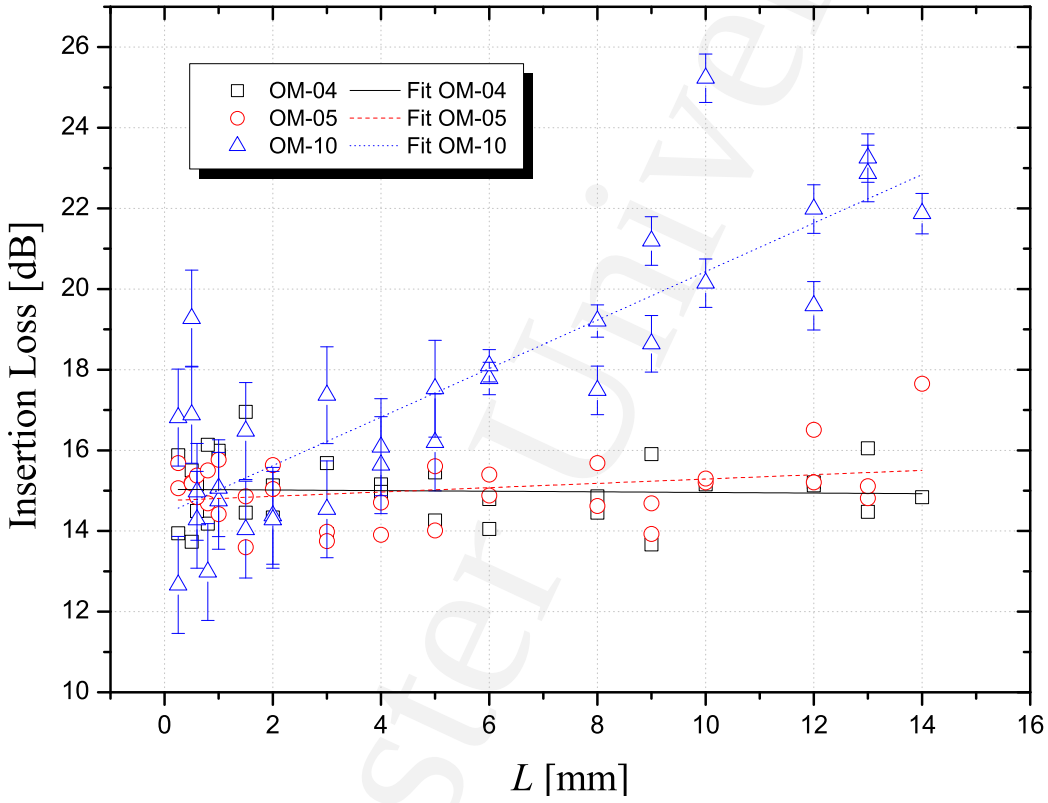

Figure 4.13: **Optical power loss measurements and linear fitting for three samples. Errors bars are similar for the rest of the data.**

All waveguides in the six samples were electrically characterized using the SPA. Figures 4.14 and 4.15 shows the I-V curves measured for sample OM-10 in froward bias (a and c) and in reverse bias (b and d). Figures 4.14a and 4.14b correspond to a duty cycle length of $3\mu m$, figures 4.14c and 4.14d to $2\mu m$ duty cycle length, figures 4.15a and 4.15b to a duty cycle length of $1\mu m$ and figures 4.15c and 4.15d to $l =$

$4\mu m$. All figures confirm the rectifying behavior characteristic of a *pn* junction. From the forward bias plots it is noted that the resistance associated with the modulator is inversely proportional to the modulator length; in other words, the longer the modulator, the higher the modulator resistance (smaller the I-V curve slope). This was observed to be independent of the duty cycle length. For reverse bias, the amount of leakage current is small[11]. The smallest leakage current is observed for sample with a $2\mu m$ duty cycle length. It is possible that this behavior is the result of a better photolithography process during fabrication and therefore a better *pn*-junction. When the samples were electrically characterized, it was observed that the microscope light intensity affected the I-V curves, in particular for sample OM-10 where an appreciable photocurrent was measured. A thorough analysis of photodetection for visible wavelengths is presented in section 4.6.

Optical power transmission measurements under different bias conditions were carried out in order to identify the amount of modulation as a function of the voltage applied. Reported here are results for the shortest and longest modulators on each sample. These measurements are focused on the *DC* absorption strength rather than the transient response, which will be dealt with in a later section. Figure 4.16 shows the results obtained for the transmission of light for sample OM-10/WG-20[12]. From figure 4.16a (in forward bias) it is clear that there is a reduction in the light intensity transmitted as the voltage applied is increased. However, it is noted that as the intensity is reduced there is a ripple behavior associated with it. Further measurements in forward bias were carried out for more samples and this "ripple" behavior was always observed. In the reverse bias configuration, similar ripples were

[11]It is small when currents of the order of tenths of nano-amperes or less are measured and when the variation on current is $(I_2 - I_1)/(V_2 - V_1) < I_2/10$ where $V_2 - V_1 = 1$[V].

[12]The nomenclature here used corresponds to: sample number (OM-♯)/waveguide number (WG-♯) according to Tables 4.2 and 4.1 respectively.

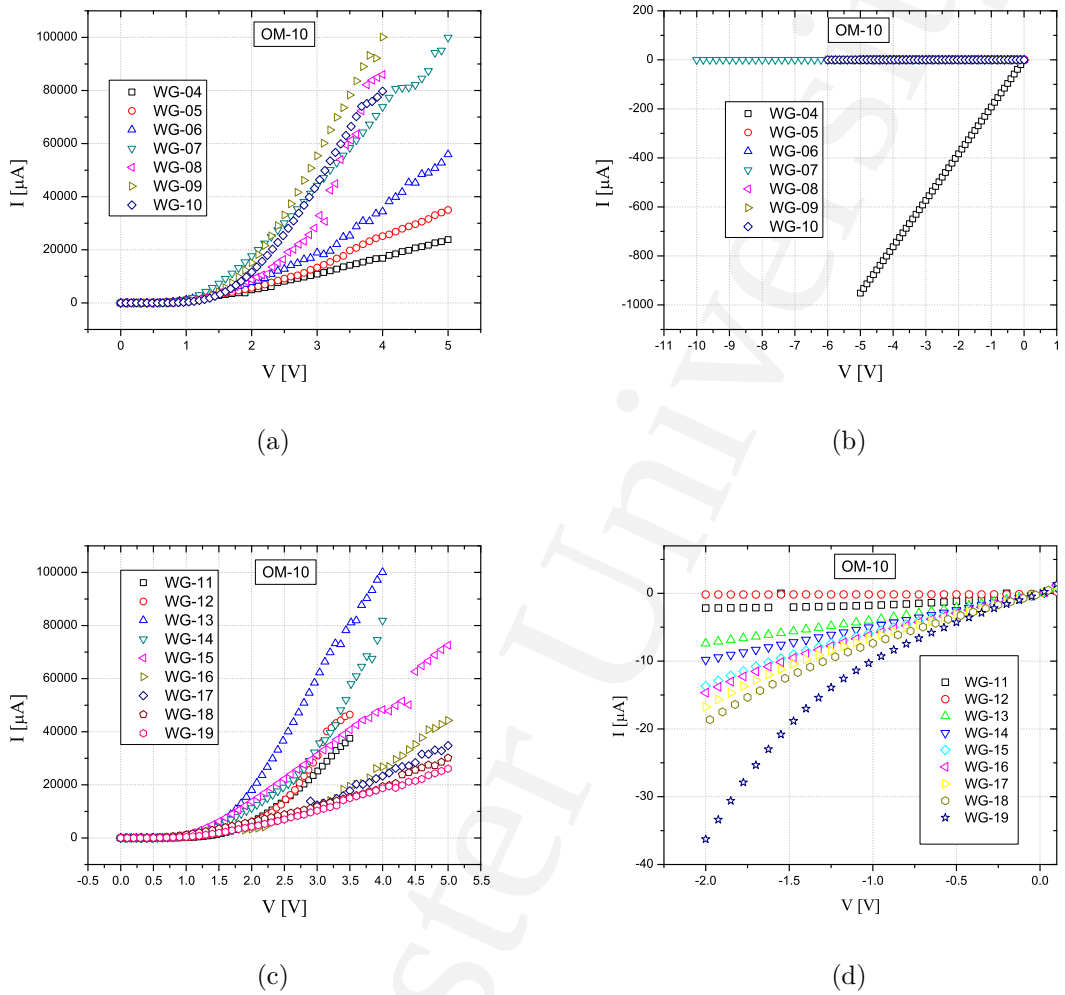

Figure 4.14: ***I-V* curves for sample OM-10 in: (a) forward bias for waveguide 04 to 10; (b) reverse bias for waveguide 04 to 10; (c) forward bias for waveguide 11 to 19; and, (d) reverse bias for waveguide 11 to 19;**

observed when the breakdown current was approached, figure 4.16b.

The signal ripple on the intensity transmission was postulated to be associated with Joule heating. In order to confirm this, optical intensity was plotted against the I^2 since the heat (power) dissipated by the modulator is proportional to the square of

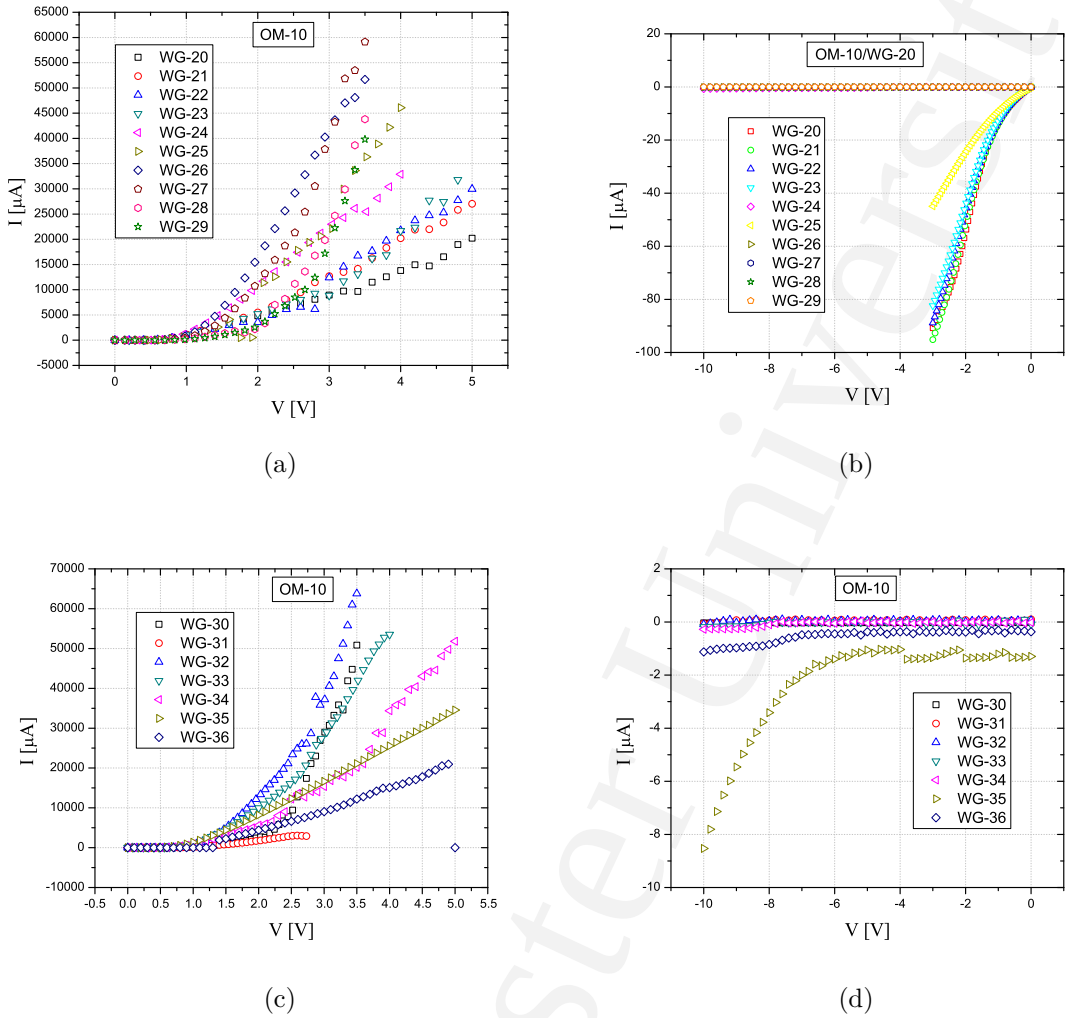

Figure 4.15: ***I-V* curves for sample OM-10 in: (a) forward bias for waveguide 20 to 29; (b) reverse bias for waveguide 20 to 29; (c) forward bias for waveguide 30 to 36; and, (d) reverse bias for waveguide 30 to 36;**

the current through it (obtained from the I-V curve) and its resistance; this provides a representation of optical intensity against power dissipated. If the optical intensity plotted as a function of I^2 follows the same trend as $O.P.$ *vs* V, it is possible to associate the variation in intensity to a heating effect. The result obtained, Figure 4.17, showed a similar profile to that measured for optical intensity against voltage

applied, and therefore strongly supports the notion of Joule heating dominating the "ripple" effect.

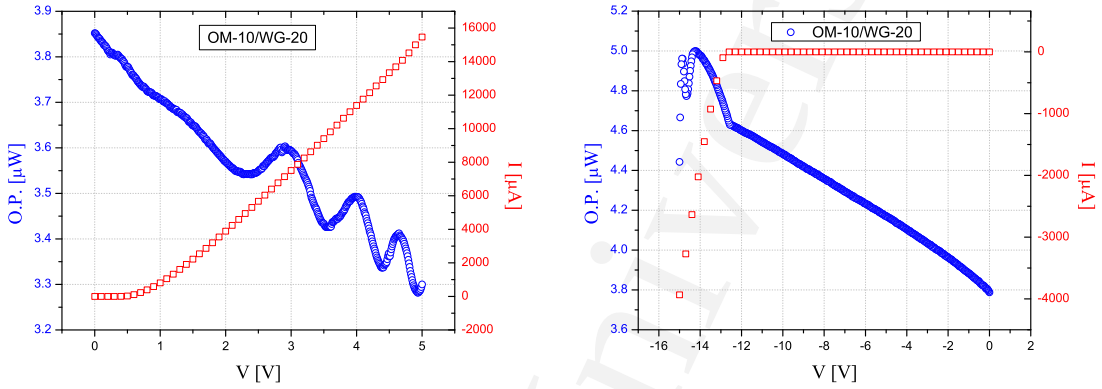

(a) Forward bias (b) Reversed bias

Figure 4.16: **Optical power intensity as function of the voltage applied (a) in forward bias and (b) in reversed bias. Measurements for device OM-10/WG-20.**

Strength of modulation as function of the forward applied bias for each modulator was measured, and from the experimental results it was identified that the modulators with a longer length were able to sustains larger voltages, which implies a higher modulation ratio. The modulation values varied from -1.5dB for 5V up to -7dB for 8V. However, the smallest length device showed modulation of the order of -1.5dB for relatively low voltages (2.5V).

With the modulators connected in reverse bias the modulation in optical intensity was relatively low, for example, from 0.05dB to 1.2dB (depending on device length) for voltages <-10V. From the values measured in reverse bias it was noted that the modulator with the longest length presented better response than the ones with the

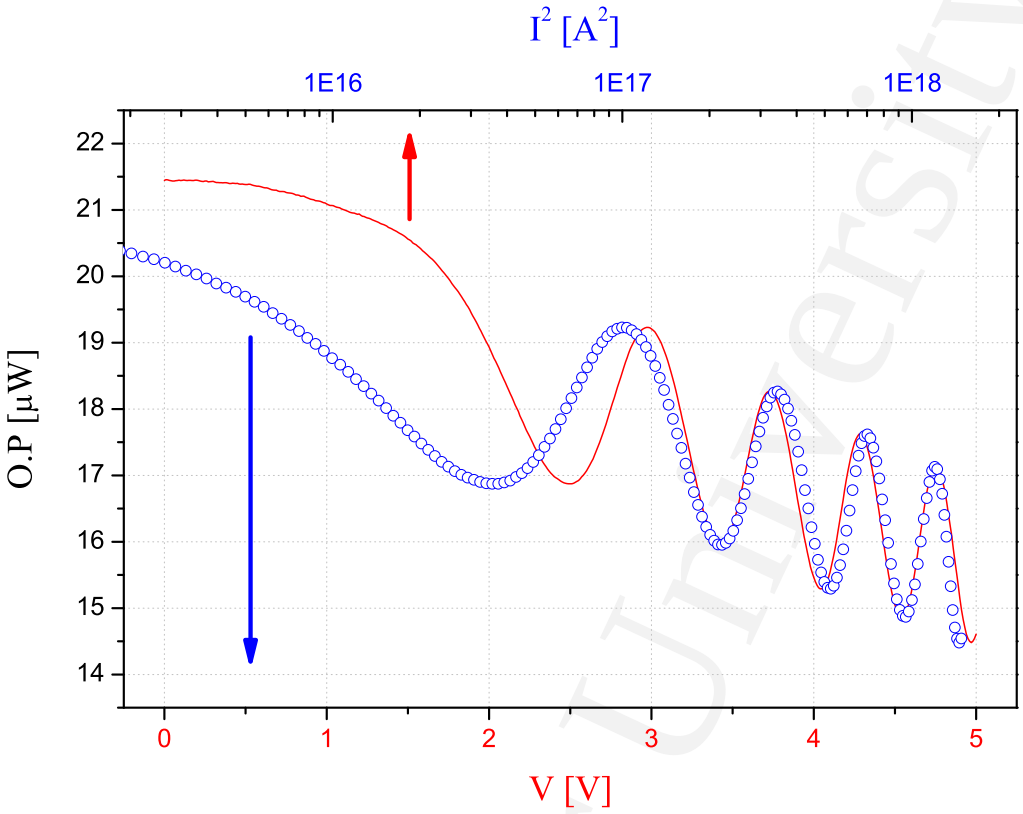

Figure 4.17: **Optical power vs Voltage (solid line) and optical power vs square current (circles), plot suggesting the effect of heating on the optical intensity measured. Measurements for device OM-10/WG-20.**

shorter length. The highest intensity modulation was observed in the sample with medium doping concentration (OM-05/WG-04).

Using the Fabry-Perot resonant method [17,118,119], it was intended to quantify the change in the real part of the refractive index as a function of the voltage applied either in forward or reversed bias. In order to do so, the measurements were done using the optical set-up, described in figure 4.12, with the addition of an electrical source of variable voltage and the replacement of the single wavelength (1550nm) laser with one tunable in the range 1550.0nm-1550.1nm.

Figure 4.18 shows the intensity spectrum as a function of the wavelength for the sample OM-04/WG-20 in forward bias. The wavelength scan was from 1550.0 nm to 1550.1 nm with a 0.001 nm step. Spectral sweeps were carried out every 0.1V from 0.1V up to 0.9V. Figure 4.18a shows the intensity spectrum for 0 and 0.9 volts and Figure 4.18b shows the intensity spectrum from 0.9V up to 1.4V (Shown separately for clarity). From figure 4.18a a small displacement to shorter wavelength and a reduction in intensity is noted. This direction of displacement was in agreement with expectation according to the resonance condition, expressed by eq.(4.8). In other words, it is known that the presence of free carriers reduces the index of refraction and thus according to eq.(4.8), a displacement to shorter resonant wavelengths was expected. For a bias up to 0.9V, the modulation is thus primarily associated with carrier dispersion. As the voltage was further increased, the intensity spectrum started to displace to the opposite direction, indicating an increase in refractive index. This behavior is associated with the *Joule effect*[13]. It is thus the Joule effect that dominates for voltages higher than 0.9V. Further increases in voltage showed a greater effect on the intensity of the spectrum rather than a continuing displacement of the spectrum (change in the refractive index). Similar behavior was observed for the other modulators of similar dimension on all chips.

The resonance condition for constructive interference is defined as

$$n2L = m\lambda \tag{4.8}$$

and the definition of free spectral range (FSR) for a Fabry-Perot interferometer is

[13]Heat generated as a result of a flowing electric current

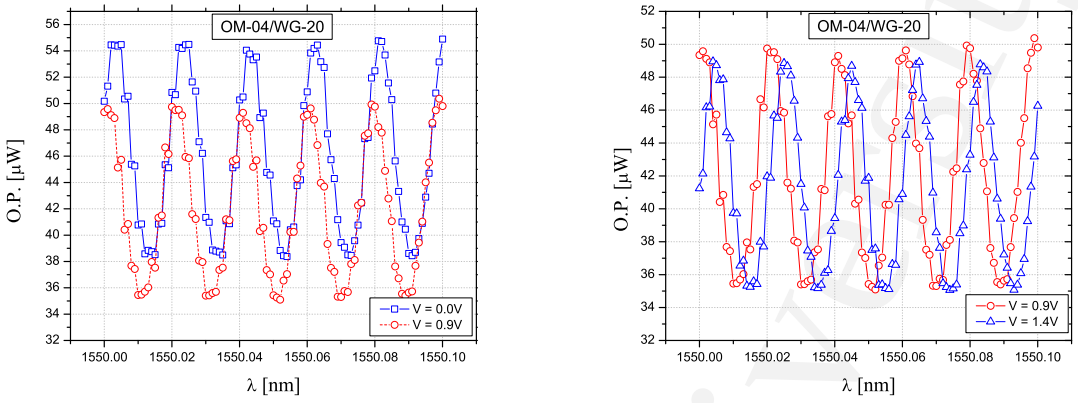

(a) (b)

Figure 4.18: **Fabry-Perot in forward bias: (a) from 0.0V to 0.9V for every 0.1V; and, (b) from 0.9V to 1.4V for every 0.1V;**

$$\Delta\lambda = \frac{\lambda_0^2}{2nL_{WG}cos\theta + \lambda_0^2} \approx \frac{\lambda_0^2}{2nL_{WG}cos\theta} \tag{4.9}$$

where λ_0 is the central wavelength of the nearest transmission peak, n is the index of refraction, θ is the angle of incidence (which is assumed to be 0) and L_{WG} is the "thickness" of the cavity (in this case, the waveguide length). Using the measured value for FSR it was possible to calculate the total optical length of the sample which resulted to be 17.98mm and from the resonance condition a change in refractive index of 4.31×10^{-5} corresponded to the shift in the spectrum by one fringe. By comparing this change in refractive index to the thermo-optical effect, it is equivalent to a reduction in the temperature of the sample of 0.239°C. From the experimental results it is calculated that a reduction in the refractive index (by the injection of free-carriers) for a $\Delta V = 0.9V$ is 4.53×10^{-6}.

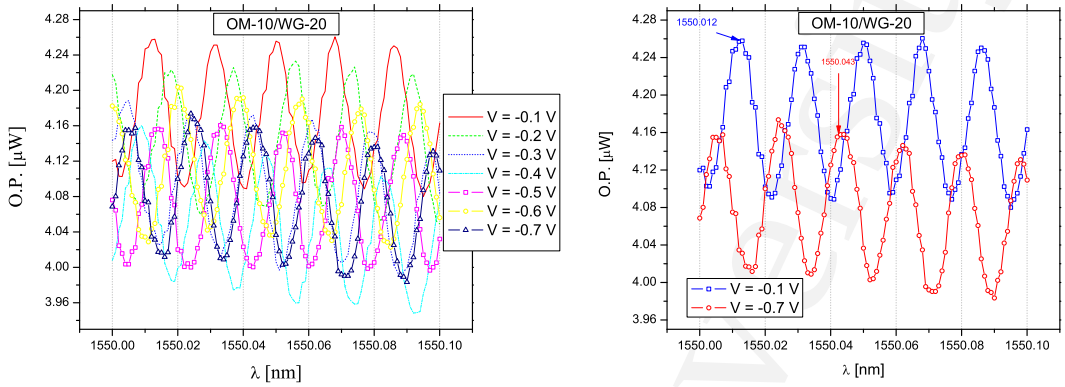

(a) (b)

Figure 4.19: **Optical power intensity as function of the voltage applied: (a) in reversed bias from -0.1V to -0.7V; and, (b) displacement of the FP spectral from -0.1V to -0.7V.**

Similar measurement where done for OM-10/WG-20 but this time in reverse bias. The voltage was varied every -0.1V from -0.1V to -0.7V. Figure 4.19a shows the optical intensity versus voltage for seven wavelengths. It is possible to distinguish a displacement to longer wavelengths, or in other words an increase in refractive index with applied bias. Figure 4.19b summarizes the total displacement. The change in refractive index calculated from this experimental result is equivalent to 9.61×10^{-5} for ΔV = -0.6V.

Additional measurements were done in order to identify the sensitivity of the modulators to the wavelength change and the voltage variation. Figure 4.20 shows the intensity change as a function of the voltage applied in forward and reverse bias. Additional to the change in intensity associated with the voltage variation, a strong resonant effect was noted.

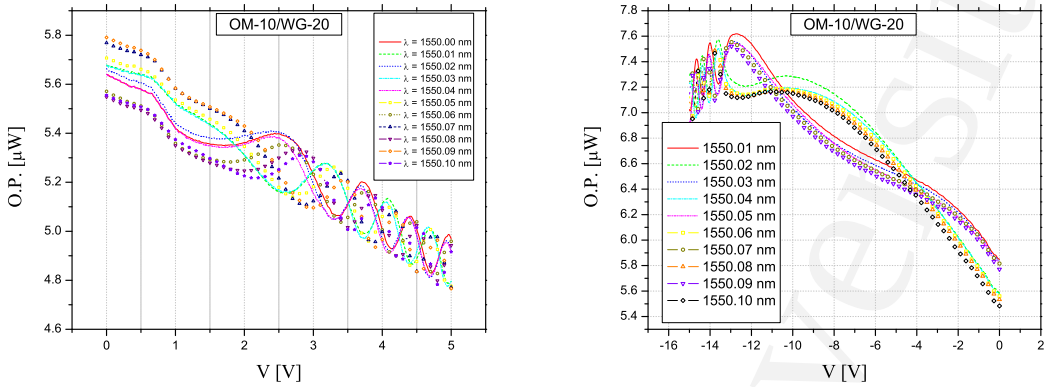

(a) Forward bias

(b) Reversed bias

Figure 4.20: **Optical power intensity as function of the voltage applied: (a) in forward bias from $\lambda = 1550.0$nm to $\lambda = 1550.1$nm; and, (b) in reversed bias from $\lambda = 1550.0$nm to $\lambda = 1550.1$nm.**

In order to measure the transient response of the modulators a square pulse of 2μs width was generated using the Pulse generator HP8082A, with a rising and falling time of 2ns, for forward and reverse bias. Figure 4.21 shows, for several samples, the optical response for the carrier injection (forward bias configuration) of the modulator labeled as WG-11. By injecting carries it was expected that the modulators would increase absorption, resulting in a reduction of intensity. Ideally, the shape of the modulated signal would be a mirror image (with respect to the horizontal axis) of the shape of the pulse applied. In order to estimate the influence of the indium levels on the optical modulation (depth of modulation and time response), these modulators were compared with some that contained boron instead of indium for the p-region.

The results shown in figure 4.21 correspond to a modulator length of 250μm, the smallest length used, with a duty cycle of 2μm. The data is presented such as the scale on the left-hand-side axis corresponds to the modulating signal (input square

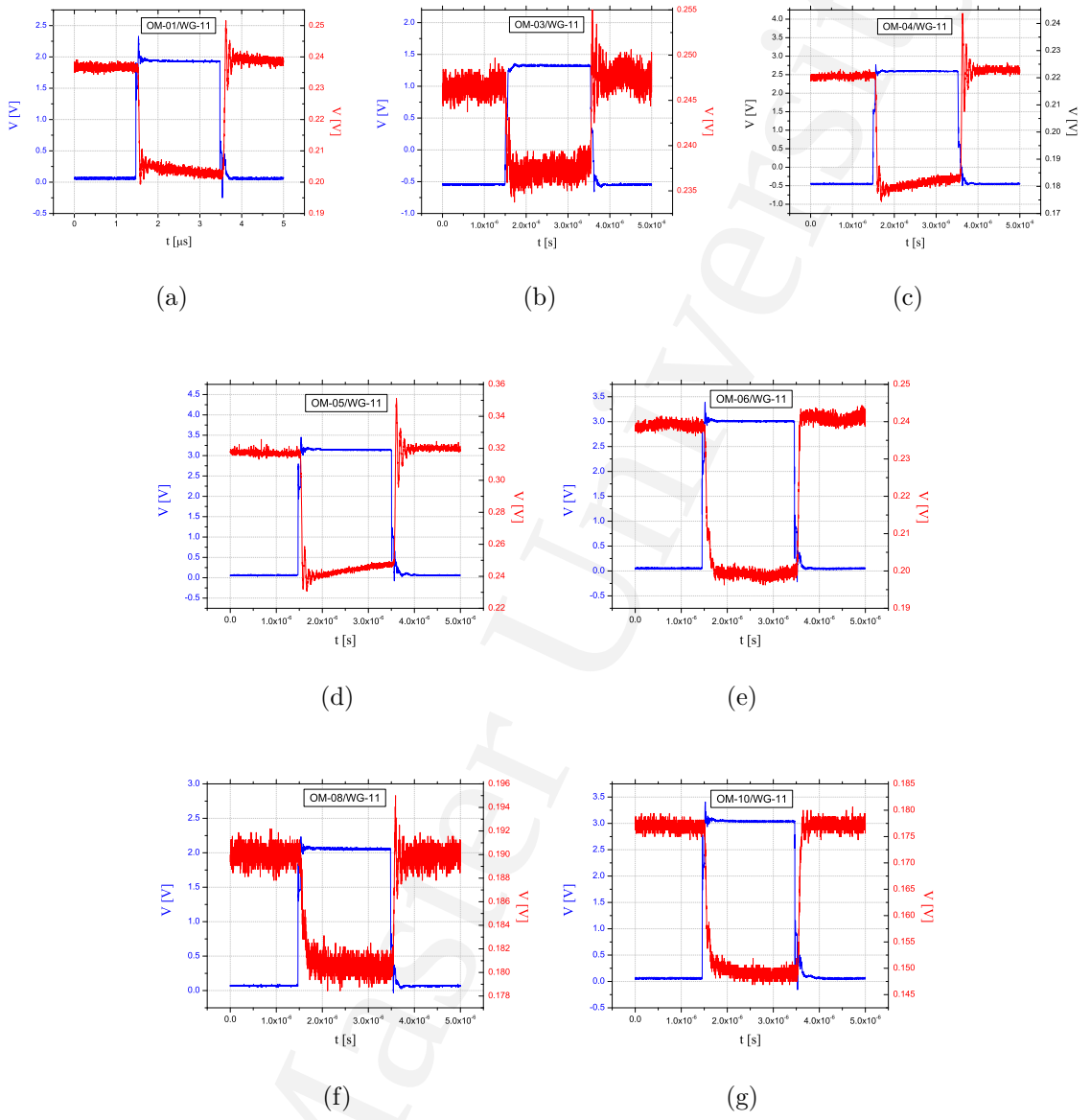

Figure 4.21: **Transient response in: (a) forward bias for OM-01/WG-11; (b) forward bias for OM-03/WG-11; (c) forward bias for OM-04/WG-11; (d) forward bias for OM-05/WG-11; (e) forward bias for OM-06/WG-11; (f) forward bias for OM-08/WG-11; and, (g) forward bias for OM-10/WG-11;**

McMaster University

signal) and the scale on the right-hand-side axis is for the modulated signal (optical intensity transmission change). The measurements were done using a Wideband Amplified InGaAs detector from Thorlabs (PDA-10CS) with a 17MHz bandwidth. The calculation of the modulated signal bandwidth is based on the definition of *analog* bandwidth[14] described as:

$$f_{max} = \frac{0.35}{t_{r,f}} \tag{4.10}$$

where $t_{r,f}$ are the rising and falling times respectively, defined as the 10%-90% transition interval. From the figures, the falling time is measured from the point where voltage of the modulated signal (representing optical intensity) starts to decrease as the input signal (modulating signal) voltage increases, up to the point where modulated signal reaches the maximum modulation value (minimum voltage), corresponding to the maximum input signal voltage. The rising time is measured in the modulated signal from the minimum voltage measured to the point it reaches its initial value after the input signal was stopped.

Extracted from Figure 4.21a are values of $t_f = 56$ns and $t_r = 64$ns, and using eq.(4.10) a bandwidth of 5.5MHz was calculated, defining the slowest response time (hading values in the tables represent samples doped with boron instead of indium).

It is necessary to mention the signal noise observed in the modulated signal after it reaches the maximum modulation point (minimum intensity) and after the input signal was reduced to zero. In order to identify its origin time periods between the first and the second minimum and between the second and the third minimum (of the ripple) were measured, resulting in a period of 79ns, and 85ns respectively.

[14]For more information about the definition of analog bandwidth, refer to chapter "Optical interconnects" pg. 131 from reference [14]

Table 4.4: **Values measured for WG-11 for samples shown in Figure 4.21.**

Sample	t_f [ns]	f_f $[MHz]$	t_r [ns]	f_r $[MHz]$	Modulation [dB/V]
OM-01	56	6.25	64	5.4	0.40
OM-03	40	8.75	44	7.95	0.14
OM-04	36	10.00	32	11.25	0.30
OM-05	48	7.3	49	7.0	0.40
OM-06	120	2.9	72	4.8	0.26
OM-08	125	2.8	64	5.4	0.13
OM-10	120	2.9	100	3.5	0.27

From the tail of the modulated signal the time period between the first and second maximum was 88ns and between the second and the third maximum was 82ns. Due to the speed of oscillation this cannot be a thermal effect which is a rather slow phenomena (of the order of hundreds of μs). It is believed that this oscillation is a result of electronic noise introduced by the electric setup which is not optimal for fast bandwidth measurements. There is also the probability that this phenomenon is influenced by periodicity of the *pn* junctions by the cyclic change in index of refraction inducing an appreciable interference effect.

The rising and falling times and modulation strength for the modulators shown in Figure 4.21 are reported in Table 4.4[15]. From these values, the recovery time[16] tends to be longer except for the OM-04/WG-11 which shows the fastest response

[15]Data in gray color corresponds to modulators with boron and phosphorus only.

[16]For forward bias, t_f is initial response time and t_r is the recovering time. For reversed bias, t_r is initial response time and t_f is the recovering time.

time, and therefore the highest bandwidth. On average, falling and rising times are slow in samples containing boron and phosphorus compute to those containing indium and phosphorus. Samples OM-01/WG-11 and OM-05/WG-11 showed higher modulation per volt; however, this feature is highly fabrication-quality dependant, where a well defined *pn* junction and homogeneous dopant concentrations along the waveguide cross-section may enhance this modulation.

Similar transient analysis were carried out on the same chip but on modulator WG-29. The main difference with respect to the previously characterized modulator is the duty cycle length, which in the case of WG-29 is 1μm. In order to identify a possible effect of the duty cycle on modulation, the transient responses were measured, and the shape of modulation is presented in figure 4.22. Table 4.5 summarized the results[17].

Table 4.5: **Values measured for WG-29 for samples shown in Figure 4.22**

Sample	t_f [ns]	f_f [MHz]	t_r [ns]	f_r [MHz]	Modulation [dB/V]
OM-01	44	7.95	48	7.3	0.18
OM-03	48	7.3	48	7.3	0.48
OM-04	48	7.3	48	7.3	0.30
OM-05	64	5.1	40	8.75	0.21
OM-06	120	2.9	40	8.75	0.21
OM-08	127	2.75	64	5.1	0.22
OM-10	175	2.0	44	7.95	0.12

[17]Data in gray color corresponds to modulators with boron and phosphorus only.

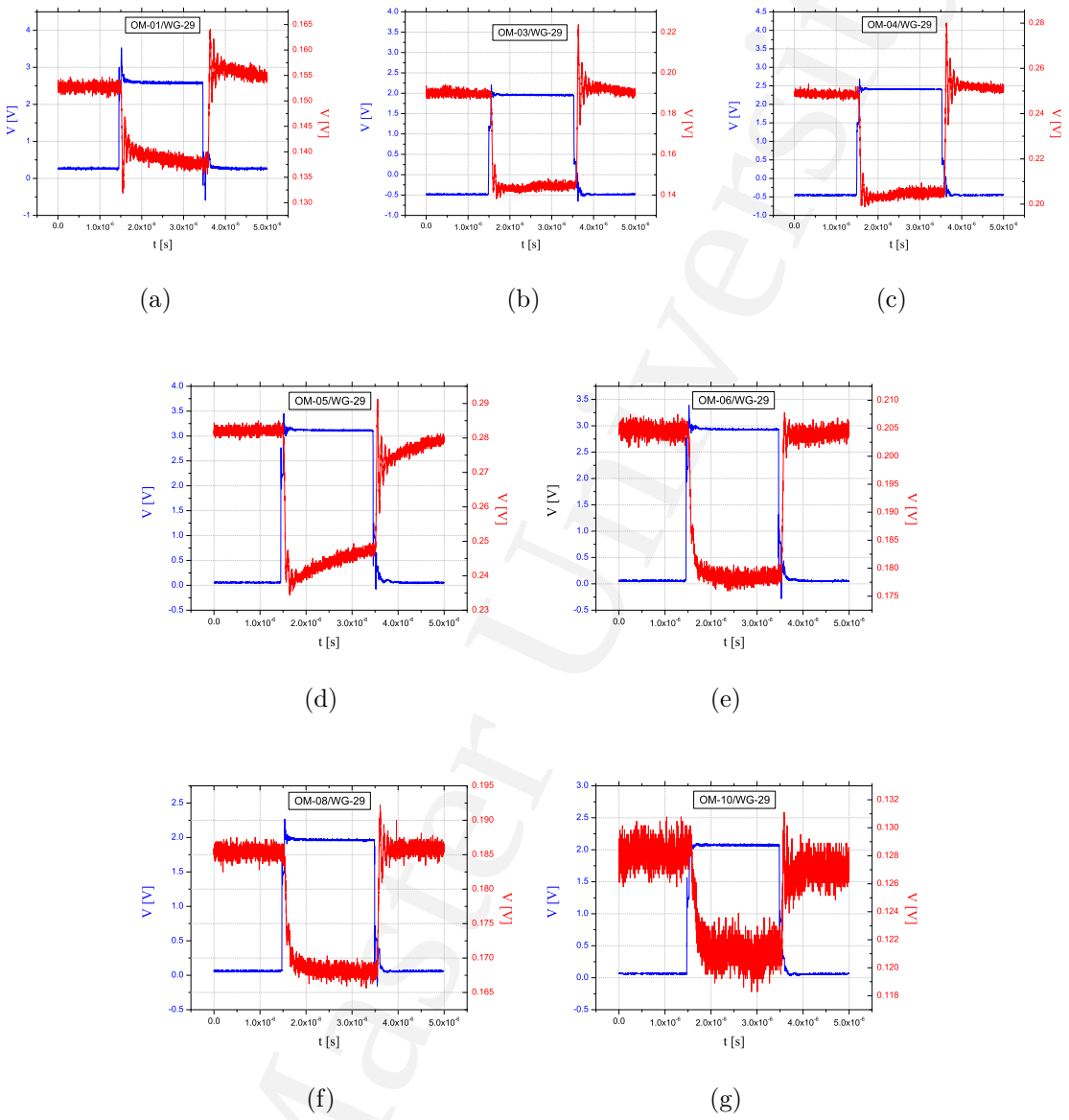

(a) (b) (c)

(d) (e)

(f) (g)

Figure 4.22: **Transient response in: (a) forward bias for OM-01/WG-29; (b) forward bias for OM-03/WG-29; (c) forward bias for OM-04/WG-29; (d) forward bias for OM-05/WG-29; (e) forward bias for OM-06/WG-29; (g) forward bias for OM-08/WG-29; and, (g) forward bias for OM-10/WG-29;**

McMaster University

Values of t_f and t_r measured for WG-29 are similar to the ones obtained for WG-11. However, the response time for modulator OM-10/WG-29 is the slowest of all of those measured. It was expected (due to the duty cycle length of 1μm) that this group[18] of modulators may show a higher modulation strength, compare to the ones in Table 4.4; however, the opposite was observed, except for OM-03.

Transient modulation in reverse bias was observed in all samples doped with indium. The ones that showed the highest modulation were those with the longest length. For samples implanted with boron (in the waveguide region), only modulators with a small length presented a rectifying behavior, characteristic of a diode. No modulation, in either reverse or forward bias, was observed for the boron-phosphorus devices with long dimensions. For the reversed bias modulation in samples with indium, again a square pulse was electrically applied to the modulator. The purpose was to remove free-charge carriers from the modulator, and therefore reduce absorption which translates to an increment of optical intensity transmission.

Figure 4.23 shows modulation in forward bias and in reversed bias, one beside the other, for WG-20 for a portion of the modulators. The versatility of these modulators is noteworthy in that they can modulate light in both configurations. It is obvious that there is a higher modulation of intensity when they are working in forward bias than in reverse bias and the modulation tends to degrade as doping concentration increases. Table 4.6 summarizes the values of t_f, t_r and modulation strength for the modulators shown in figure 4.23. The "F" at the front of the sample number represent forward configuration and "R" reversed configuration.

The fact that only modulators with a long dimension (WG-20 has a length of

[18]Each sample has four groups of modulators, and each group is defined by the length of the duty cycle which are four.

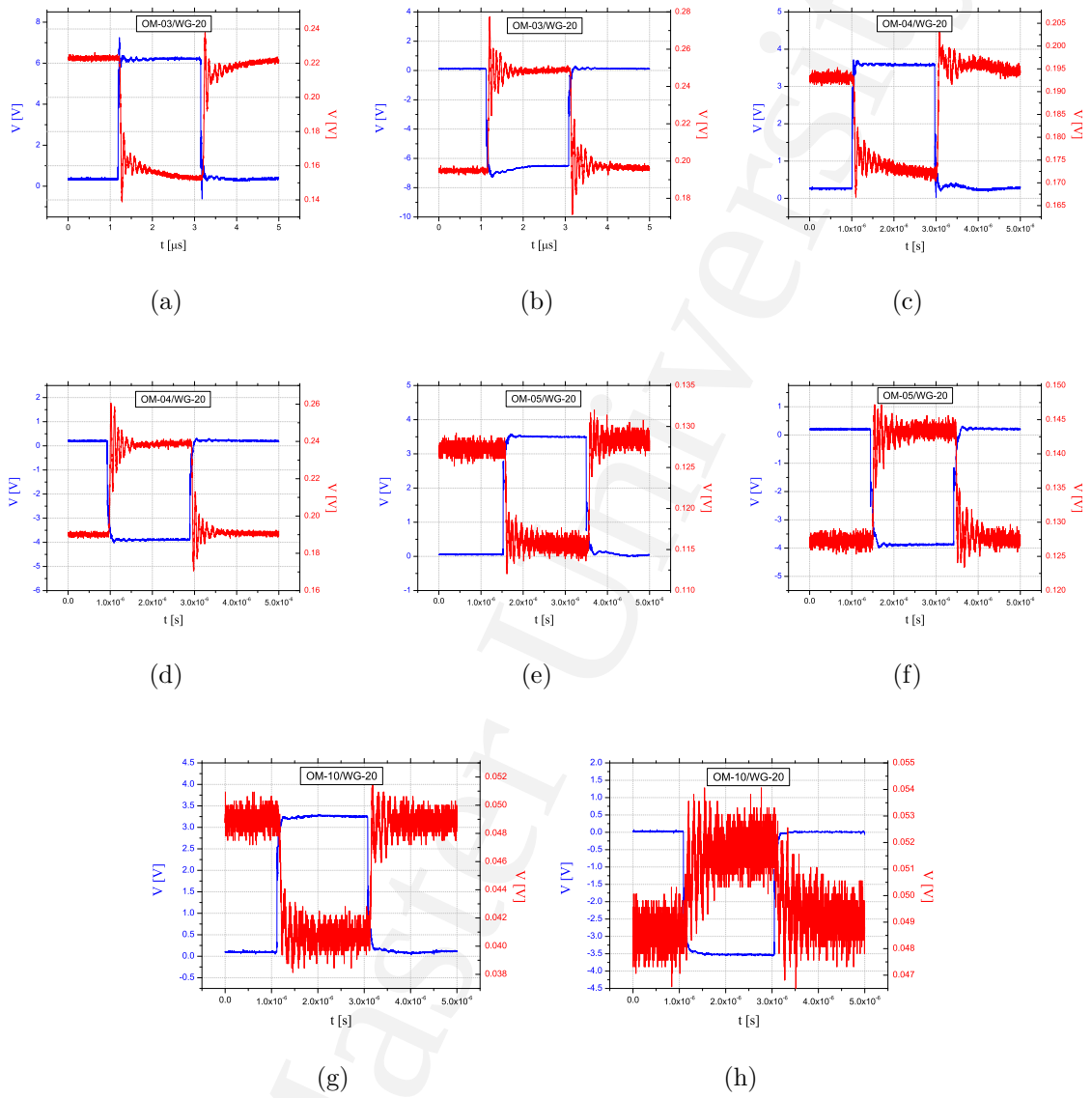

Figure 4.23: **Transient response in: (a) forward bias for OM-03/WG-20; (b) reverse bias for OM-03/WG-20; (c) forward bias for OM-04/WG-20; (d) reverse bias for OM-04/WG-20; (e) forward bias for OM-05/WG-20; (f) reverse bias for OM-05/WG-20; (g) forward bias for OM-10/WG-20; and, (h) reverse bias for OM-10/WG-20;**

McMaster University

Table 4.6: **Values measured for WG-20 for samples shown in Figure 4.23**

Sample	t_f [ns]	f_f $[MHz]$	t_r [ns]	f_r $[MHz]$	Modulation [dB/V]
F OM-03	56	6.25	50	7.0	0.27
R OM-03	48	7.3	44	7.95	0.16
F OM-04	48	7.3	48	7.3	0.14
R OM-04	48	7.3	48	7.3	0.25
F OM-05	40	8.75	40	8.75	0.13
R OM-05	48	7.3	48	7.3	0.13
F OM-10	68	5.15	60	5.8	0.23
R OM-10	60	5.8	60	5.8	0.07

14 mm) showed an appreciable modulation in reverse bias is an indication of a small change in depletion width, with the modulators that showed the highest change being OM-04/WG-20. From all the experimental results, it is noted that samples with indium concentration smaller than $3\times10^{17}\text{cm}^{-3}$ (implantation doses $\leq 5\times10^{15}\text{cm}^{-2}$) showed the best modulation in the reverse bias mode.

4.6 Impurity Photovoltaic Effect

An interesting result was observed when measuring the I-V curves for each modulator. The light of the optical microscope, used for waveguide-fiber alignment and electrical probing, generated a photocurrent whose strength showed a dependency on the intensity of the light incident on top of the sample. This phenomenon was observed in all samples co-doped with indium and phosphorus, but not in samples

McMaster University

co-doped with boron and phosphorous. Sample OM-10 showed the highest photocurrent. Photovoltaic efficiency was measured using a system specialized in solar cell characterization. The values obtained are reported in the present section, Table 4.7, as well as a brief description of the phenomenon involved in the carrier generation via impurities known as the *Impurity Photovoltaic Effect* (IPV) [92, 97, 120–123].

The IPV is a two-step process that consists of the generation of electron-hole pairs by the absorption of two low-energy photons through a deep-impurity level introduced in the silicon bandgap. In other words, electrons in the valence band are optically excited to the deep-impurity level by the absorption of a photon of energy $E_T < h\nu_1 < E_g$ and then from the deep-impurity level to the conduction band by the absorption of a photon with energy $E_g - E_T < h\nu_2 < E_g$. Therefore, enhancing the sub-band gap wavelength absorption of the solar cell [122].

The introduction of a midgap level in the silicon bandgap was initially thought to improve the efficiency of a solar cell by allowing carrier generation via the impurity level, and therefore increasing the current output. However, Shockley and Queisser argued that an increase in efficiency is unlikely because these same midgap states also act as recombination centres [124] and hence reduce the V_{oc}. A study from $Würfel$ [125] supported the conclusion that midgap levels do not improve the efficiency in a solar cell. However, there have been some theoretical studies more recently that suggest that if the energy level is carefully chosen far from the gap centre, where the optimal position occurs when E_T is located at one-third or two-third of E_g [126, 127], the IPV effect can contribute to an improvement in the solar cell efficiency [128, 129]. Keevers and Green [92] presented a theoretical study of the IPV effect where indium is the deep-impurity level in the silicon bandgap. They presented a modified *SRH* model in which electrons and holes can be optically excited to and from the impurity

McMaster University

level in addition to the thermal capture and excitation from it, as the diagram shown in Figure 3.3. They mention that the incorporation of indium leads to a significant I_{sc} increase due to the subgap wavelength absorption. However, it reduces the V_{oc}. Schmeits and Mani [121] suggested that this reduction in V_{oc} is related to the fact that when the indium concentration approaches the value of the background doping concentration (shallow n-type dopant) the effective doping concentration of the junction is reduced and, as a consequence, the built-in voltage V_{bi} of the junction decrease. In addition, the free-carrier concentration is reduced, which leads to an increase of the resistance in series.

Keevers and Green computed an increase of efficiency due to the IPV effect of only 1-2% . They suggested that the limiting process in the IPV effect is the electron photoemission from the indium level, which competes with the hole photoemission from the indium level and the intrinsic band-to-band absorption[19], which reduce the available photon flux. They suggested that in order to provide a better IPV effect, and therefore an increase of current output, it is better to keep the indium levels fully occupied, thus suppressing competing effects such as the hole photoemission process. This can be done by maintaining the n-type phosphorus dopant concentration higher than the indium concentration.

Since the solar cell is a single-junction diode, its performance can be derived from the I-V characteristic which is measured under standard test conditions (STC, Air Mass 1.5—AM1.5—, 1000 W/m^2 irradiation and 25°C). Four important parameters are extracted form this curve [130–132]: open circuit voltage V_{oc}, short-circuit current I_{sc}, fill factor FF and energy conversion efficiency η. The efficiency is calculated using

[19]In all the theoretical model they assume that the two photoemission process from the indium level are only induced by sub-band gap wavelength photons. However, it does not necessarily mean that photoemission from the indium level may not be induced by photons with energy higher than the bandgap.

McMaster University

the expression

$$\eta = \frac{P_{max}}{AP_{in}} = \frac{V_{mpp}I_{mpp}}{AP_{in}} = \frac{V_{oc}I_{sc}FF}{AP_{in}} \tag{4.11}$$

where P_{max} is the maximum generated power, A is the area of the cell, P_{in} is the incident power which is 1000 W/cm^2 at STC and $P_{max} = V_{mpp}I_{mpp}$, where V_{mpp} and I_{mpp} are the voltage and current at the maximum power point respectively. The fill factor is defined as

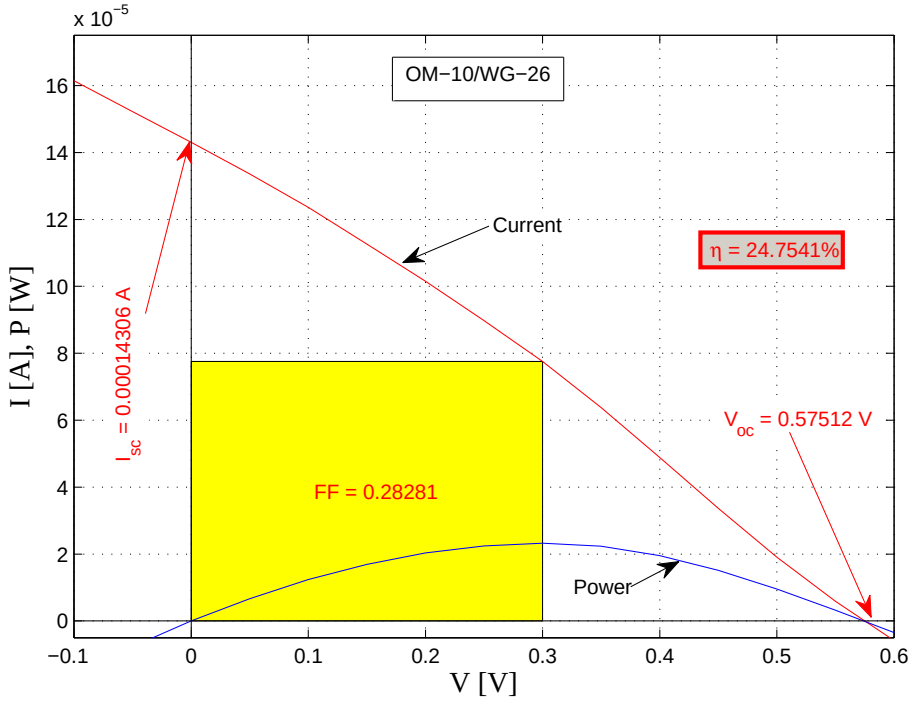

Figure 4.24: **I-V characteristics of a** $47 \times 10^{-4} \times 0.2cm^2$ **indium doped solar cell measure at STC. The** $I_{sc} = 143.06\ \mu A$**;** $V_{oc} = 0.5751$**V, and** $\eta = 24.7\%$**.**

$$FF = \frac{V_{mpp}I_{mpp}}{V_{oc}I_{sc}} \tag{4.12}$$

which is a measure of the 'squareness' of the I-V curve. The sign convention for current in photovoltaics is such that the photocurrent is positive, contrary to the usual convention.

In the present case, before carrying out any measurement the sample was covered, except for the area of interest, to ensure that the current output is only generated by electron-hole pairs formed in the active region. Figure 4.24 shows the typical diagram for photocurrent, and the parameters extracted from the current-voltage characteristics for sample OM-10/WG-26. The area used for the calculation is derived from the dimensions of the modulator reported in Table 4.1, which are the length of the modulator L and the separation distance between the p^{++} and n^{--} terminals, Figure 4.4. Figure 4.25a shows the dark current and the photocurrent obtained for OM-10/WG-20 for a sweep of -2V to 2V. Figure 4.25b is a close-up of the same curves, where is possible to distinguish the increment of photo-carriers and identify its V_{oc} and I_{sc}.

Table 4.7 summarizes the important parameters extracted from Figure 4.26. The data are presented starting form the longest device to the shortest one. It is clear that the V_{oc} is almost constant but the I_{sc} decreases as the length of the modulator is reduced from $373.7\mu A$ to just $9.7\mu A$. In spite of a 56 times reduction in area, the I_{sc} only decreases 41 times. An interesting observation of this I-V curve is the shape, which is noticeably different from that for a conventional PV cell. Deviation from the typical shape is the result of power dissipation through the resistance of the contacts and through leakage currents around the sides of the device. These two effects are electrically equivalent to connecting a resistor to a solar cell in series (R_s) and connecting a resistor to a solar cell in parallel (R_{sh}), respectively. Ideally,

McMaster University

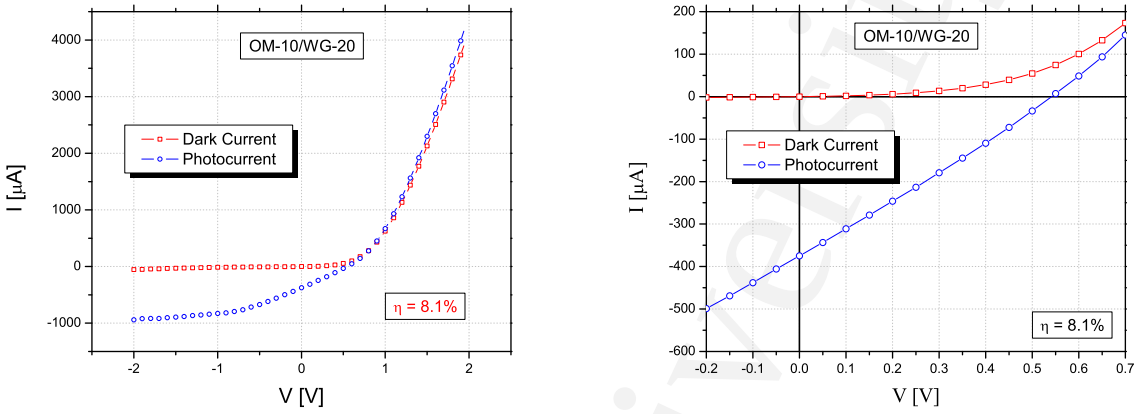

(a) (b)

Figure 4.25: **Current vs Voltage measured for sample OM-10/WG-20: (a) when there is no illumination, dark current, and with illumination, photocurrent; and, (b) a close-up view of both curves near origin.**

it is always preferable that R_s to be as small and R_{sh} to be as large as possible. Otherwise, FF is reduced and therefore, so is the efficiency. From the measurements reported here, as the length of the devices reduces, the FF marginally increases and thus therefore, the efficiency. However, maximum efficiency is not achieved for the smallest device but for one that is almost ten times longer.

A rectifying behavior (typical I-V curve of a diode) is associated with a high value of R_{sh}, an indication of low leakage current. From figure 4.25a, the I-V curve showed a rectifying behavior and the dark current values for a negative voltage between 0 and -2V are smaller than -50μA, which suggest a relatively low leakage current. Therefore, the atypical shape of the I-V curves, figure 4.26, is not so much attributed to the resistance connected in parallel. The other factor affecting the shape of the I-V curves is the resistance connected in series. By deduction, the shape of this I-V

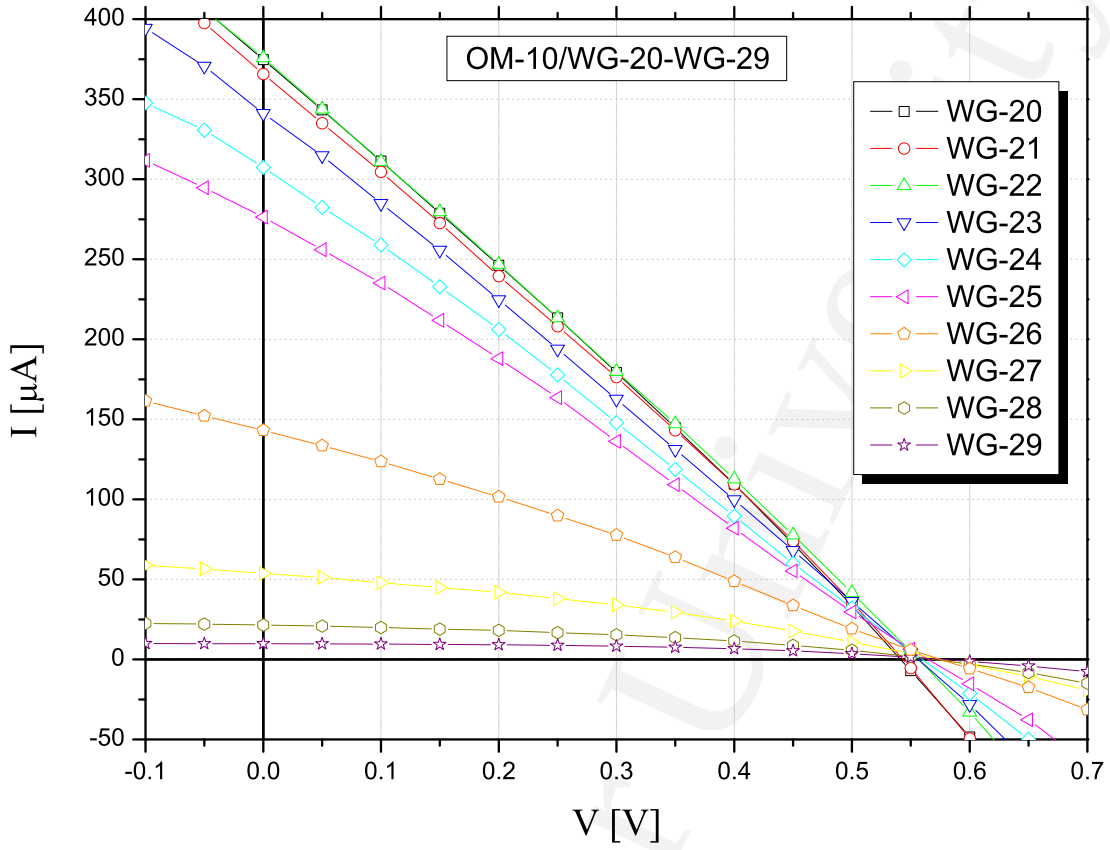

Figure 4.26: ***I-V* characteristics for waveguide 20 to waveguide 29, for Sample OM-10.**

curve is assumed to be a result of high resistance in series, an indication of opposition to current flow through the material and thin metal contacts.

It is accepted that an increase in I_{sc} (above that seen for typical solar cells) is associated with the absorption of sub-bandgap wavelengths. At the same time I_{sc} is directly proportional to the photon flux, which explains why in the experimental results the samples with the bigger area show higher current. The efficiency related to FF which at the same time depends on the V_{oc}. Therefore, a reduction in V_{oc} indicates a reduction in efficiency.

Table 4.7: **Values measured and efficiency calculated for Solar cells doped with indium**

Sample	V_{oc} [V]	I_{sc} [μA]	FF	η [%]
OM-10/WG-20	0.541	373.76	0.226	8.1
OM-10/WG-21	0.543	365.75	0.266	9.3
OM-10/WG-22	0.556	375.79	0.258	11.5
OM-10/WG-23	0.556	341.11	0.258	13.0
OM-10/WG-24	0.559	307.31	0.260	15.8
OM-10/WG-25	0.564	276.25	0.264	21.9
OM-10/WG-26	0.575	143.06	0.282	24.7
OM-10/WG-27	0.576	53.71	0.333	21.9
OM-10/WG-28	0.568	21.44	0.390	20.7
OM-10/WG-29	0.575	9.79	0.473	22.7

Two possible contributing factors to the high I_{sc} may be the doped area under illumination, which consists of two doped regions, and the structure configuration. In the first doped region, indium levels are fully compensated, since the concentration of shallow donors (phosphorus) is approximately three time higher than that of indium. Therefore, this region may predominantly absorb photons with energy $> E_g - E_t$. For the second doped region, there are no n-type shallow donors, hence only a fraction of the indium level is occupied as a result of a hole thermal emission. This availability of neutrally-charged states allows the possibility of hole photoemission induced by the absorption of photons with energy $> E_t$. This process can only contribute to

McMaster University

the output current if this electron is eventually promoted to the conduction band by an electron photoemission process. In order to have an efficient solar cell not only electron-hole pair creation is thus considered but at the same time how the charge is separated and collected. Here is where the structure configuration plays an important role. Experimental results reported by Kasai and Matsumura [133] showed that the incorporation of indium in silicon thin films ($< 10\mu$m) increases the absorption coefficient in the infrared and visible region of the solar spectrum. This is a result of the absorption of not only photon energy smaller than E_g, but at the same time photon energy larger than E_g [134] (a result of a large cross-section for photon/indium interaction). Unlike conventional cell designs, where a thicker ($> 10\mu$m) silicon layer is usually employed to ensure complete absorption of the solar spectrum photons with energy higher than the band gap, we assume that our approximately 2.5μm thick silicon layer absorbs a large fraction of light due to indium level excitation. Additionally, the position of the *pn*-junction in the first micron or so in the silicon layer is oriented parallel to the light propagation[20], changing to a perpendicular orientation to the light propagation direction, see figure 4.5a as a reference. At the same time the buried oxide from the SOI structure confines the electron-hole pair in a small volume, where, if they do not recombine[21], they diffuse either to one of the contacts where the corresponding charge is easily collected, or to the depletion region where the electron-hole pair is separated to their respective charge type by the built-in electric field. Assuming that there is no recombination in the depletion region, each charge is forced to move to their respective charge region where they can freely move and be easily collected. More measurements were performed in order to determine the influence of the duty cycle on the solar cell efficiency and FF, results are reported on Figure 4.27 and 4.28b respectively.

[20] See Figure 4.5a for the orientation of the *pn*-junction in a *xy*-plane

[21] Which depends of the diffusion length of the minority carrier.

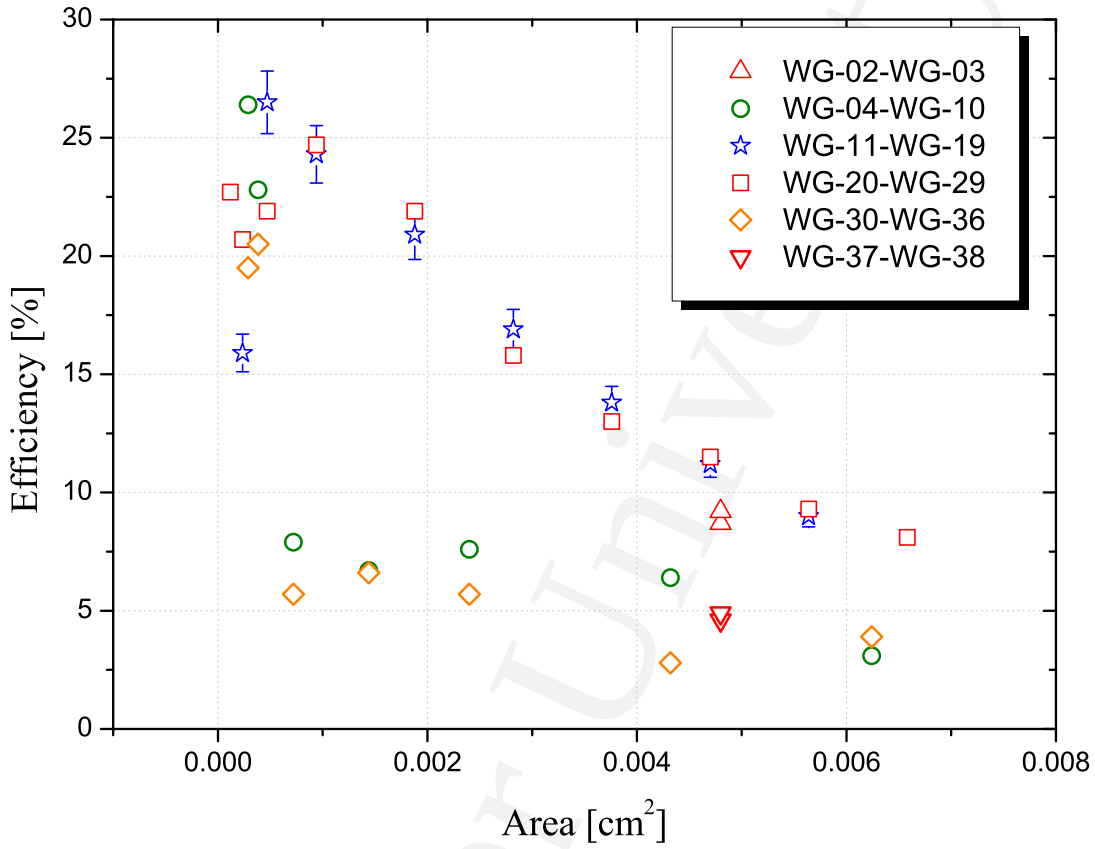

Figure 4.27: **Solar cell efficiency vs area for sample OM-10 as a function of duty cycle dimensions.**

Figure 4.27 shows that cells with smaller duty cycle length, in general, present better efficiency for all four configurations, and from the plot there is an obvious trend for increasing efficiency as the dimension (in particular the total length, L) of the cell is reduced. Cells with duty cycle of 1μm and 2μm showed similar efficiency when the total area of the cells are comparable or equal, reaching a maximum efficiency when the length, L, of the cell was ~2mm. This result suggests that for two adjacent *pn*-junctions, the depletion regions width extend[22] such as they may

[22]In a *pn*-junction with a high different in concentrations for each region, it is expected that the depletion extend more in the region with lower doping concentration, which is the *p*-type region, and

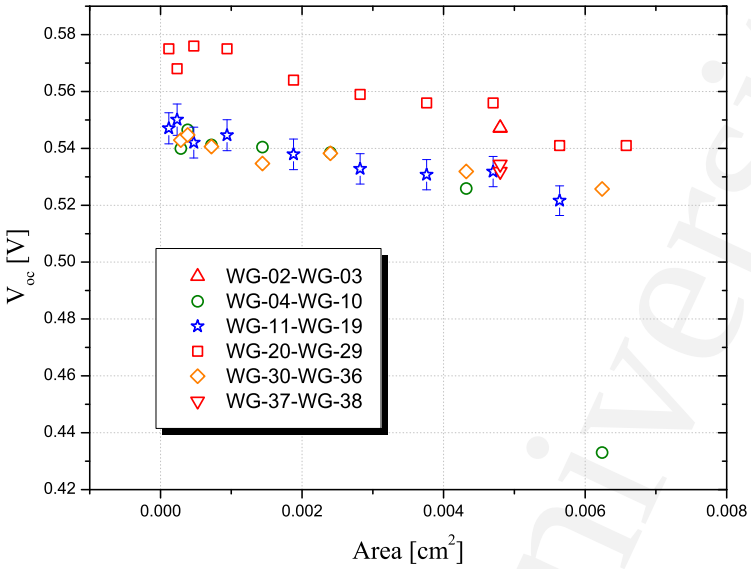

(a) V_{oc}

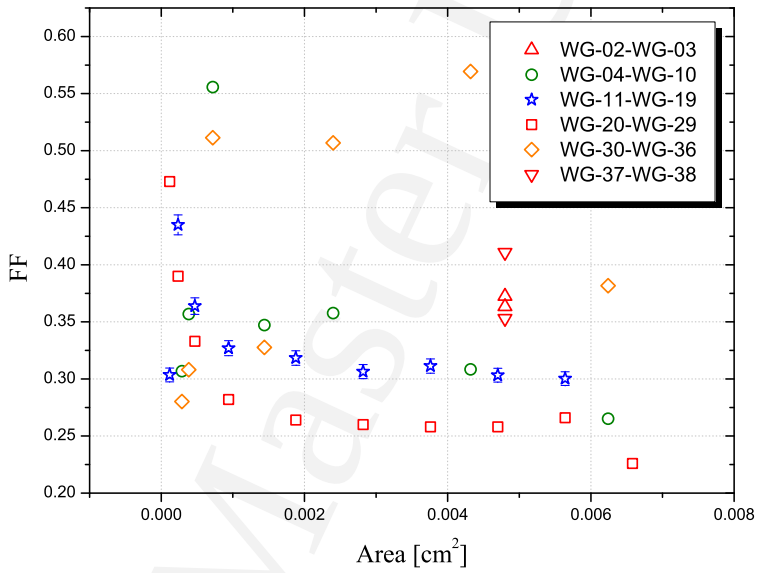

(b) FF

Figure 4.28: **Effect of duty cycle length on: (a) V_{oc} vs area, error bars are similar for the rest of experimental data; and, (b) Fill Factor vs area.**

therefore when we refer to two adjacent *pn*-junctions are the ones facing each other on the *p*-type region.

McMaster University

overlap, explaining why duty cycles of 1μm and 2μm have similar result. When the duty cycle length increases (3μm and 4μm) the efficiency drops, suggesting that the proximity and/or overlap of adjacent depletion regions is reduced proportionally to the increase of separation of the *pn*-junctions or with the diffusion length of minority carriers. Careful choice is thus required to ensure the doping concentration and the spacing of the *pn*-junctions are arranged in a comb-type structure with a continuous proximity and/or overlapping of adjacent depletion regions. This configuration increases the area/volume[23] where the carriers generated by the absorption of light are effectively collected and separated resulting in the outstanding value of photocurrent. Fill Factor is an implicit function of V_{oc} [124] but is greatly affected by the series and shunt resistance [80]. It is noted that V_{oc} is almost the same for all the cells, with equal indium and phosphorus concentrations, independent of the dimension of the cell and the duty cycle length, Figure 4.28a. However, the FF values reported in Figure 4.28b, imply that the cells are greatly affected by the series and shunt resistance.

More investigation is planed to be performed regarding the effects of indium in solar cells, and in particular the concentration ratios of indium and phosphorus, to more efficiently take advantage of this phenomenon based on the experimental results here reported.

4.7 Final Thoughts

In the present chapter the implementation and characterization of an optical modulator based on a novel *pn*-junction configuration proposed by *Li et. al.* was described. The main difference between the current modulator and that proposed by *Li et. al.* was the use of indium as the *p*-type dopant. The use of indium was based

[23]Possibly from a couple of hundred nanometers up to micrometer size

McMaster University

on previous knowledge of possible optical modulation by controlling the charge state of the deep-level impurity. In the present work the successful demonstration of indium mediated optical modulation was described, while optical absorption by indium can be adjusted by changing the concentration of the n-type shallow impurity used as background doping in a fully compatible CMOS process. An additional characteristic is that the use of phosphorus as the background dopant compensates the indium levels resulting in a reduction of the net doping concentration. This compensation is translated to higher optical transmission due to the fact that each indium level compensated by the shallow n-type impurity is not available for optical absorption of 1550nm wavelength and at the same time the absorption by free-carries is reduced.

It was observed that all modulators functioned in forward bias with a frequency bandwidth of the order of MHz. However, the modulators with long lengths were the only ones that showed an appreciable intensity modulation in reversed bias. This may suggest that the interaction between the optical waveguide-mode and depletion region may not be optimal. However, the recovery of intensity plus the frequency bandwidth measured are promising results and with smaller dimensions and tighter fabrication conditions better modulation may be achieved.

The outstanding values of photocurrent obtained from the samples doped with indium open the possibility of a real efficiency enhancement in silicon solar cell by exploiting the IPV effect. The periodic and vertically-oriented pn-junction configuration suggests a highly efficient way to collect and separate photo-carries. This motivates the further investigation to fully understand the origins of these effects in addition to the possibility of a new approach in the photovoltaic field on the pn-junction configuration for efficiency enhancement of solar cells.

McMaster University

Chapter 5

Conclusions And Suggestions For Further Work

In this thesis a model has been developed that calculates the occupancy fraction and the resulting optical absorption, for 1550nm wavelength, of a single deep-level impurity in the silicon bandgap, in particular the one introduced by indium or thallium. The model shows that optical absorption can be modulated by controlling the charge state of the deep impurity level. Experimental samples consisting of doped silicon waveguides were subsequently fabricated. These waveguides were implanted and annealed such that a uniform concentration of thallium was achieved. The waveguides were then co-doped with different doses of phosphorus in order to change the occupancy fraction of the thallium. The phosphorus compensated the thallium deep-level changing its charge state from neutral to negative, where the amount of light absorbed would be proportional to the number of deep-levels in a neutral state. Absorption values for a thallium dose of $7.4 \times 10^{13}\text{cm}^{-2}$ varied from 7.4dB/cm for a low background doping concentration to 3.2dB/cm for a background doping concentration similar to that of thallium. Values of optical absorption for the dose of

McMaster University

$1.2 \times 10^{13}\text{cm}^{-2}$ range from 10.8dB/cm for low phosphorus concentration, to a reduced value of 5.4dB/cm when the background concentration increases, matching that of thallium. The model predicted that the thallium deep-levels would be completely compensated when the concentration of phosphorus is in excess with respect to the thallium concentration. However, from the optical absorption measurements, Figure 3.12, a residual absorption was obtained. This residual absorption is assumed to be induced by thallium levels in a neutral state, first, as a result of not being compensated by a shallow donor or, second, due to its high capture rate for holes. For the first case it is suggested that this is an effect induced by high doping concentration that affect the diffusion of phosphorus, which translated in a partial compensation of the thallium centres. More studies on an atomic level are required in order to better understand the integration and electrical activation of thallium in silicon and the possible electrical interactions with phosphorus ions within the silicon lattice, which may contradict or in the best case scenario confirm what is suggested in this work.

Optical modulation was demonstrated by control of the charge state of deep impurity levels in silicon by implementing an indium-doped SOI rib waveguide optical modulator. Frequency bandwidth of the order of a few MHz were obtained. It is the author's understanding that this is the first report of the operation of an optical SOI rib waveguide modulator using the configuration proposed by *Li et.al.* where the addition of indium was to increase the modulation strength [33].

In terms of future work, the author suggest the implementation of 3D-2D numerical model to help in the determination of the optimal dimensions for specific doping concentrations and the reduction in dimensions of the devices where a better modulation strength and transient response can be achieved by a more homogeneous dopant distribution. Two groups of modulators should be study, one doped with boron

McMaster University

and phosphorus and the other group doped with indium and phosphorus, in order to quantify the influence of the deep-impurity level on optical modulation. Investigation at an atomic level should be carried out in order to corroborate the electrical activation on indium in silicon with the presence of phosphorus and its distribution along the waveguide cross-section.

During the electrical and optical characterization of the optical modulators an appreciable photocurrent was measured. This high photocurrent motivates the study of its origins, where the initial assumptions suggest that this photocurrent was the result of a two-steps photon absorption process induced by the indium level, in which two photons with energy smaller than the silicon energy bandgap were absorbed, generating an electron-hole pair that contributed to the increase in photocurrent. However, measurements of solar cell efficiency showed great dependency on the distance between *pn*-junctions. In other words, cells with smaller duty cycle length showed higher efficiency, which may be the result of a highly efficient separation and collection of carries generated by the absorption of light. Although, the shape of the IV curves and the FF values imply high losses induced by shunt and series resistance, these losses can be reduced by improving the photolithography process. In these samples, there is no surface texturization and by texturizing the surface, it is possible to enhance light trapping, which allows the possibilities for higher efficiency improvement of thin silicon solar cell. More studies are required to fully understand why a thin silicon layer doped with indium produced such high photocurrents and the influence of the *pn*-junction configuration. As future work, it is proposed to identify which photons are the ones producing this photocurrent, by using long-pass filters, and the amount of photons that are absorbed, to study the influence of indium concentration and indium/phosphorus concentration ratio on solar cell efficiency, to investigate the effect on efficiency by the orientation and configuration of

the *pn*-junctions, as well its position relative to the buried oxide, and to consider the possibility of increasing photocurrent by increasing the thickness of the silicon layer as a result of more absorption of light.

McMaster University

Appendix A

KOH Wet Etching

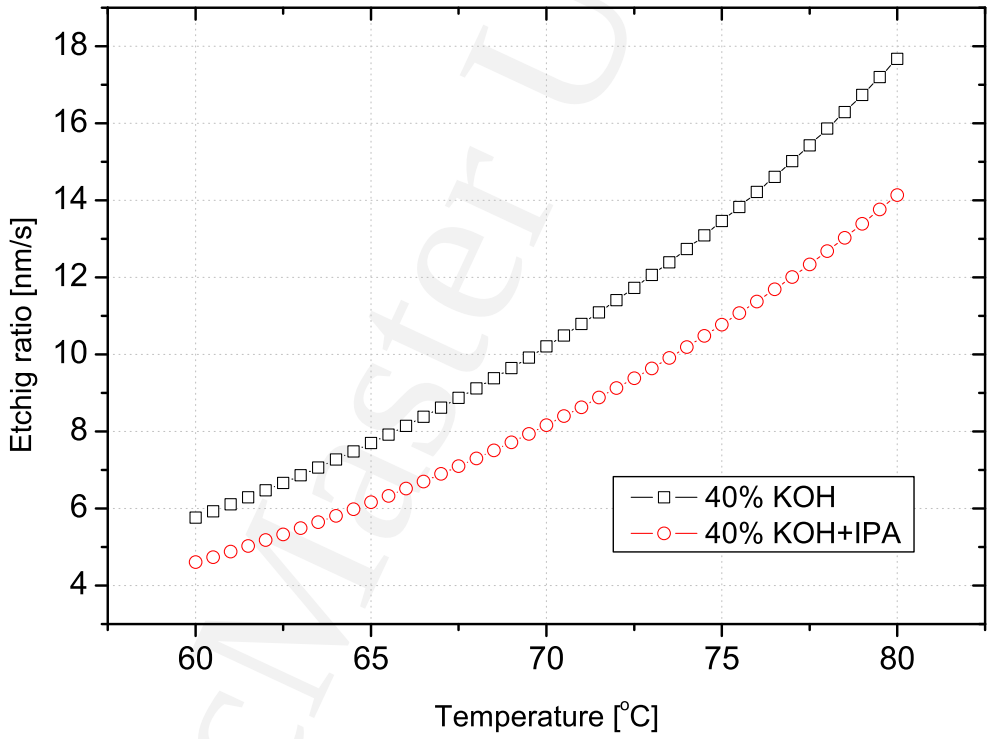

Figure A.1: **Etching ration vs Temperature for a 40% KOH and 40% KOH + IPA, extracted from [135] .**

McMaster University

Appendix B

PL Mask

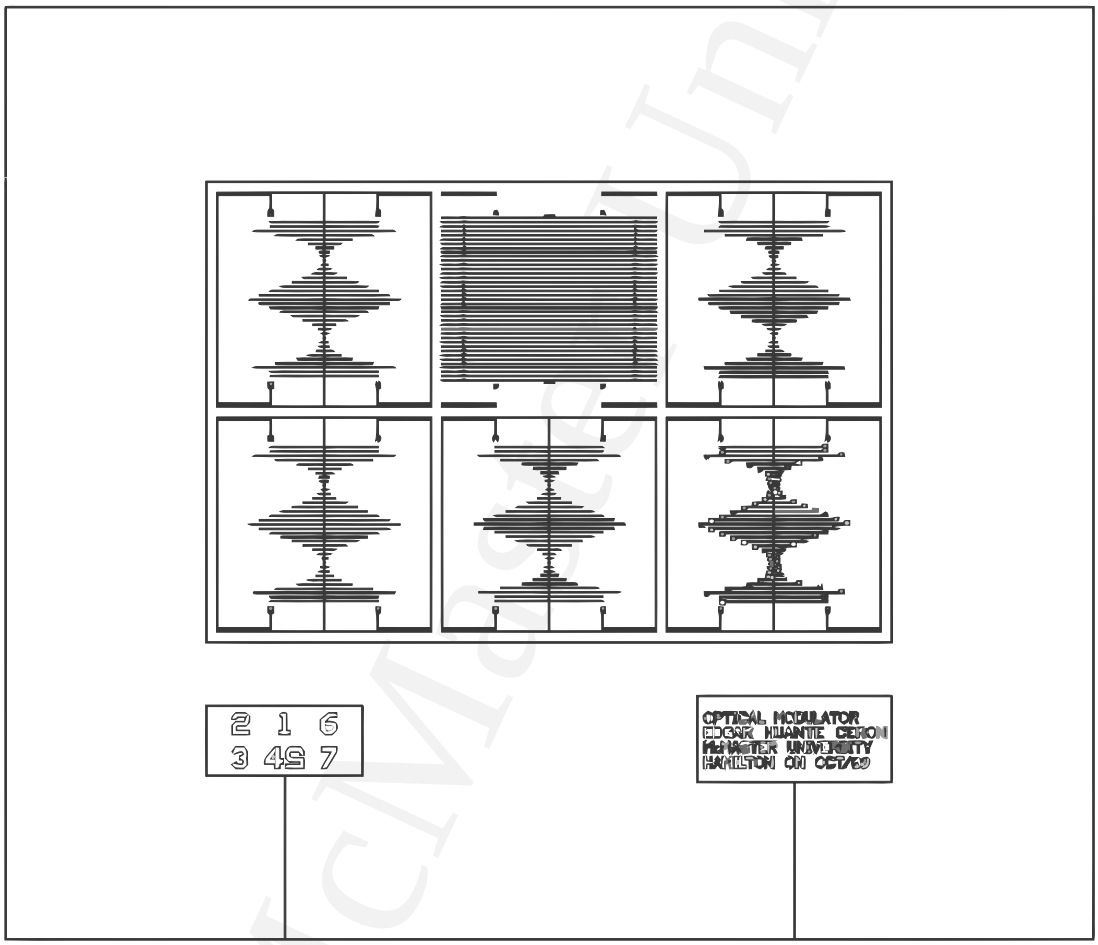

Figure B.1: **Photolithography mask for the fabrication of the indium modulator.**

McMaster University

Appendix C

Matlab Program

```
%Program used for the calculation of the amount of In or Thallium
 occupied states in Si
%See Martin A. Green, J. Appl. Phys. Vol. 67(6) March 1990, pg.2944-2954
%calculating the V_bi and depletion region
%
tic
clear
points=10000;%number of point
num=10;%number of concentration for acceptors, Na
num2=100;%number of concentration for donors, Nd
cm=1000000;
%- - - - - - - - - - - - - - - - - -
%- - - - - - - - - - - - - - - - - -
P_opt=000.0e-3;%power in Watts [J/s] - - -      <-----
%- - - - - - - - - - - - - - - - - -
%- - - - - - - - - - - - - - - - - -
Eg=1.1242;%band gap for Si at 300K.
E_T=0.157;%Impurity, energy level [eV]
g_t=4;%impurity-level degeneracy factor 4 for indium
%- - - - - - - - - - - - - - - - - -
% E_T = 0.074 for Gallium (Na)
% E_T = 0.157 for Indium (Na)
% E_T = 0.246 for Thallium (Na)
% E_T = 0.19  for Nitrogen (Nd)
% E_T = 0.25  for Carbon (Nd)
% a = acceptors, d = donors
%- - - - - - - - - - - - - - - - - -
lambda=1.55e-6;
k=8.617e-5;%Boltzman's constant [eV/K]
```


McMaster University

```
h=4.14e-15;%Plank's constant [eV-s]
T=300;%Temperature [K]
q=1;%electrical charge in [eV]
e_r=11.8;% relative dielectric constant for Si
e_0=8.85e-12;%[F/m]
m_0=9.11e-31;%electron mass [kg]
m_n=1.08*m_0;%Density-of-states effective mass for electrons
m_p=1.15*m_0;%Density-of-states effective mass for holes
mc_n=0.28*m_0;%electron conductivity effective mass
mc_p=0.41*m_0;%hole conductivity effective mass
Nc=2*(2*pi*m_n*k*T/h^2)^(3/2)/(1.6e-19)^(3/2);%Effective Density of
 states for Conduction Band
Nv=2*(2*pi*m_p*k*T/h^2)^(3/2)/(1.6e-19)^(3/2);%Effective Density of
 states for Valence Band
n_i=sqrt(Nc*Nv).*exp(-Eg/(2*k*T));%intrinsict charge carriers [m^-3]
E_i=Eg/2 + (k*T/2).*log(Nv/Nc);%Instrinsic energy level
%- # - # - # - # - # - # - # - # - # - # - # - # - # -
sig_n=2.0e-22;%electron capture cross section [cm^2]
sig_p=8e-15;%hole capture cross section [cm^2]
%- - - - - - - - - - - - - - - - - -
% sig_n(In) = 2.0e-22 [cm^2]
% sig_p(In) = 8e-15 [cm^2] or 5.07e-15
% sig_n(Tl) = 1e-22 [cm^2] review value
% sig_p(Tl) = 2.4e-14 [cm^2]
%- - - - - - - - - - - - - - - - - -
OpCross_p=(1.7e-17)/10000;%in [m^2]
OpCross_n=0/10000;
%- - - - - - - - - - - - - - - - - - - - - - - - - - - - - - - - - -
%OpCross_p=(2.6e-17)/10000;%in m^2 for Thallium data from paper      -
%OpCross_p=(1.7e-17)/10000;%in m^2 for Indium data from paper        -
%OpCross_n=0/10000;%in m^2 for Indium data from paper                -
%- - - - - - - - - - - - - - - - - - - - - - - - - - - - - - - - - -
WG_a=2.5e-6*4e-6;%pi*((2.5e-6)/2)*((4e-6)/2);%;%2.5e-6*4e-6;%;%WG cross
-section area [m^2]
Opt_flux=(P_opt/((1.60217646e-19*h*299792458/lambda)*WG_a));%Optical
 Flux [1/m^2 s]
OFn=OpCross_n*Opt_flux;
OFp=OpCross_p*Opt_flux;
Vth_n=sqrt(3*k*T*1.6e-19/mc_n);%electron thermal velocity [sqrt(J/kg)]=
[m/s]
Vth_p=sqrt(3*k*T*1.6e-19/mc_p);%hole thermal velocity [m/s]
c_n=(sig_n/10000)*Vth_n;%electron capture rate [m^3/s]
```


McMaster University

```
c_p=(sig_p/10000)*Vth_p;%hole capture rate
n_1=g_t*n_i.*exp((E_T-E_i)./(k*T));% in [m^-3]
p_1=(1/g_t)*n_i.*exp(-(E_T-E_i)./(k*T));% in [m^-3]
e_n=c_n*n_1;%electron emission rate
e_p=c_p*p_1;%hole emission rate
Na_max=24.146128;%Thallium is 23.5682,Indium is 24.146128
Na=logspace(22,Na_max,num);%number of implanted acceptors ions [m^-3]
Nd=logspace(21,24,num2);%number of implanted donors ions [m^-3]
A=(0:(Eg)/points:Eg);
%-------------------------------------------------------
%- - - - - - - - - - - - Inclomplet Ionization - - - - - - - - - - - -
N_b=6e24;%in [m^-3]
N_ref=2.2e24;%in [cm^-3]
c=2;
d=2.3;
g=0.5;
E_dop_0=45.5e-3;%[eV]
P_ion=zeros(length(Nd),length(T));
E_dop_P=zeros(length(Nd));
for m=1:length(T)
    for i=1:length(Nd)
        E_dop_P(i)=E_dop_0./(1+(Nd(i)./N_ref).^c);
        b=1/(1+(Nd(i)./N_b).^d);
        %Nc=2.86e25*(T(m)/300)^(1.58);
        n11=Nc*exp(-E_dop_P(i)/(k.*T(m)));
        g_d=b./(g+(1-b).*Nd(i)./n11);
        P_ion(i,m)=1/(1+g_d.*Nd(i)./n11);
    end
end
%----------
p=zeros(num,points+1);
n_a=zeros(num,points+1);
B=zeros(num,points+1);
C=zeros(num,points+1);
C_in=zeros(num,points+1);
D=zeros(num,points+1);
D_in=zeros(num,points+1);
E_f=zeros(num2,num);
E_f_in=zeros(1,num);
n_a0=zeros(num2,num);
n_a0_in=zeros(1,num);
N_occu=zeros(num2,num);
```

McMaster University

```
N_occu_in=zeros(1,num);
N_a100=zeros(num2,num);
N_a100_in=zeros(1,num);
p_0=zeros(num2,num);
p_0_in=zeros(1,num);
I=zeros(1,num);
I_in=zeros(1,num);
U_cn=zeros(num2,num);
U_cp=zeros(num2,num);
V_bi=zeros(num2,num);
W=zeros(num2,num);
x_p0=zeros(num2,num);
NetN=zeros(num2,num);
%----------------------------
for m=1:num2,
    for l=1:num,
        for i=1:points+1,
            if  (E_i-A(1,i)) >= 0
                p(l,i)=n_i.*exp((E_i-A(1,i))./(k*T));
            else
                p(l,i)=((n_i).^2)./(n_i.*exp((A(1,i)-E_i)./(k*T)));
            end
            n_a(l,i)=(e_n+c_p.*p(l,i)+OFn)./(e_n + c_n.*((n_i.^2)./p
            (l,i)) + OFn + e_p + c_p.*p(l,i) + OFp);%G-R occupied by "h"
            B(l,i)=(1 - n_a(l,i)).*Na(1,l);
            C(l,i)=(((p(l,i)).^2) + (Nd(1,m).*P_ion(m,1).*p(l,i)) -
             ((n_i).^2) )./p(l,i);%or only Nd(1,m)
            C_in(l,i)=(((p(l,i)).^2) - ((n_i).^2) )./p(l,i);%for Nd(1,m)
            =0
            D(l,i)=B(l,i)-C(l,i);
            D_in(l,i)=B(l,i)-C_in(l,i);
        end
        [Dmin,I(l)]=min(abs(D(l,:)));
        [Dmin_in,I_in(l)]=min(abs(D_in(l,:)));
        E_f(m,l)=A(1,I(l));
        E_f_in(1,l)=A(1,I_in(l));
        %- - - - - - - - - - - Intrinsic - - - - - - - - - - -
        if E_f_in(1,l) <= E_i
           p_0_in(1,l)=n_i.*exp((E_i-E_f_in(1,l))./(k*T));
        else
           p_0_in(1,l)=((n_i).^2)./(n_i.*exp((E_f_in(1,l)-E_i)./(k*T)));
        end
```

```
        n_a0_in(1,l)=((e_n+c_p.*p_0_in(1,l)+OFn)./(e_n + c_n.*((n_i.^
        2)./p_0_in(1,l))+OFn+ e_p + c_p.*p_0_in(1,l)+OFp)).*Na(1,l);
        N_occu_in(1,l)=((e_p+c_n.*(((n_i)^2)./p_0_in(1,l)) + OFp)./
        (e_n + c_n.*((n_i.^2)./p_0_in(1,l))+OFp+ e_p + c_p.*
        p_0_in(1,l)+OFn)).*Na(1,l);
        N_a100_in(1,l) = N_occu_in(1,l)./Na(1,l);
        %- - - - - - - - - - - Indium and Phosphorus - - - - -
        if E_f(m,l) <= E_i
           p_0(m,l)=n_i.*exp((E_i-E_f(m,l))./(k*T));
        else
           p_0(m,l)=((n_i).^2)./(n_i.*exp((E_f(m,l)-E_i)./(k*T)));
        end
        n_a0(m,l)=((e_n+c_p.*p_0(m,l)+OFn)./(e_n + c_n.*((n_i.^2)
        ./p_0(m,l))+OFn+ e_p + c_p.*
        p_0(m,l)+OFp)).*Na(1,l);
        N_occu(m,l)=((e_p+c_n.*(((n_i)^2)./p_0(m,l)) + OFp)./
        (e_n + c_n.*((n_i.^2)./p_0(m,l))+OFp+ e_p + c_p.*
        p_0(m,l)+OFn)).*Na(1,l);
        N_a100(m,l) = N_occu(m,l)./Na(1,l);
        U_cn(m,l) = c_n.*n_a0(m,l).*((n_i^2)./p_0(m,l));%electron
         capture rate [electrons/m^{3}s]
        U_cp(m,l) = c_p.*N_occu(m,l).*p_0(m,l);
        % - - - - PN-Junction - - - -
        NetN(m,l)=Nd(1,m)-(N_occu(m,l)-N_occu_in(1,l));
        V_bi(m,l)=(k*T/q).*log((N_occu_in(1,l).*NetN(m,l))./(n_i).^2);
        W(m,l)=sqrt(((2*e_r*e_0.*V_bi(m,l))/(1.6e-19)).*((
        N_occu_in(1,l)+NetN(m,l))./(N_occu_in(1,l).*NetN(m,l))));
        x_p0(m,l)=N_occu_in(1,l)./(N_occu_in(1,l)
        +NetN(m,l)).*W(m,l);
    end
%
end
%  *  *  *  *  *  *  *
%/\/\/\/\/\/\/\/\/\/\/\/\/\/\/\/\/\/\/\/\/\/\/\/\/\/\/\/\/\/\/\/\
%  *  *  *  *  *  *  *
figure(9)
    semilogx9 = semilogx(Nd/cm,(1-(N_a100)),'LineStyle','none');
    set(semilogx9(1),'DisplayName','N_a = 10^{16} [cm^{-
    3}]','LineStyle','-');
    set(semilogx9(2),'DisplayName','N_a = 1.66x10^{16} [cm^{-
    3}]','LineStyle','--');
    set(semilogx9(3),'DisplayName','N_a = 2.78x10^{16} [cm^{-
```

```
    3}]','LineStyle',':');
    set(semilogx9(4),'DisplayName','N_a = 4.64x10^{16} [cm^{-
    3}]','LineStyle','-.');
    set(semilogx9(5),'DisplayName','N_a = 7.74x10^{16} [cm^{-
    3}]','MarkerSize',4,'Marker','o');
    set(semilogx9(6),'DisplayName','N_a = 1.29x10^{17} [cm^{-
    3}]','MarkerSize',4,'Marker','square');
    set(semilogx9(7),'DisplayName','N_a = 2.15x10^{17} [cm^{-
    3}]','MarkerSize',5,'Marker','x');
    set(semilogx9(8),'DisplayName','N_a = 3.58x10^{17} [cm^{-
    3}]','MarkerSize',5,'Marker','.');
    set(semilogx9(9),'DisplayName','N_a = 5.99x10^{17} [cm^{-
    3}]','MarkerSize',5,'Marker','+');
    set(semilogx9(10),'DisplayName','N_a = 10^{18} [cm^{-
    3}]','MarkerSize',4,'Marker','pentagram');
xlabel('N_d [cm^{-3}]')
ylabel('p_T/N_a')
% - - - - - - - - - - - - - - - - - - - -
figure(14)
subplot(2,1,1)
    loglog14 = loglog(Nd/cm,U_cn./cm,'LineStyle','none');
    set(loglog14(1),'DisplayName','N_a = 10^{16} [cm^{-
    3}]','LineStyle','-');
    set(loglog14(2),'DisplayName','N_a = 1.66x10^{16} [cm^{-
    3}]','LineStyle','--');
    set(loglog14(3),'DisplayName','N_a = 2.78x10^{16} [cm^{-
    3}]','LineStyle',':');
    set(loglog14(4),'DisplayName','N_a = 4.64x10^{16} [cm^{-
    3}]','LineStyle','-.');
    set(loglog14(5),'DisplayName','N_a = 7.74x10^{16} [cm^{-
    3}]','MarkerSize',4,'Marker','o');
    set(loglog14(6),'DisplayName','N_a = 1.29x10^{17} [cm^{-
    3}]','MarkerSize',4,'Marker','square');
    set(loglog14(7),'DisplayName','N_a = 2.15x10^{17} [cm^{-
    3}]','MarkerSize',5,'Marker','x');
    set(loglog14(8),'DisplayName','N_a = 3.58x10^{17} [cm^{-
    3}]','MarkerSize',5,'Marker','.');
    set(loglog14(9),'DisplayName','N_a = 5.99x10^{17} [cm^{-
    3}]','MarkerSize',5,'Marker','+');
    set(loglog14(10),'DisplayName','N_a = 10^{18} [cm^{-
    3}]','MarkerSize',4,'Marker','pentagram');
xlabel('N_d [cm^{-3}]')
```

```
ylabel('electron capture rate [electrons/cm^{3}s]')
%- - - - - - - - - - - - - - - -
subplot(2,1,2)
    loglog15 = loglog(Nd/cm,U_cp./cm,'LineStyle','none');
    set(loglog15(1),'DisplayName','N_a = 10^{16} [cm^{-
    3}]','LineStyle','-');
    set(loglog15(2),'DisplayName','N_a = 1.66x10^{16} [cm^{-
    3}]','LineStyle','--');
    set(loglog15(3),'DisplayName','N_a = 2.78x10^{16} [cm^{-
    3}]','LineStyle',':');
    set(loglog15(4),'DisplayName','N_a = 4.64x10^{16} [cm^{-
    3}]','LineStyle','-.');
    set(loglog15(5),'DisplayName','N_a = 7.74x10^{16} [cm^{-
    3}]','MarkerSize',4,'Marker','o');
    set(loglog15(6),'DisplayName','N_a = 1.29x10^{17} [cm^{-
    3}]','MarkerSize',4,'Marker','square');
    set(loglog15(7),'DisplayName','N_a = 2.15x10^{17} [cm^{-
    3}]','MarkerSize',5,'Marker','x');
    set(loglog15(8),'DisplayName','N_a = 3.58x10^{17} [cm^{-
    3}]','MarkerSize',5,'Marker','.');
    set(loglog15(9),'DisplayName','N_a = 5.99x10^{17} [cm^{-
    3}]','MarkerSize',5,'Marker','+');
    set(loglog15(10),'DisplayName','N_a = 10^{18} [cm^{-
    3}]','MarkerSize',4,'Marker','pentagram');
xlabel('N_d [cm^{-3}]')
ylabel('hole capture rate [holes/cm^{3}s]')
%----------------------------------
%N_a100=N_a100';
Nd=Nd';
arreglo1=[Nd/cm,(1-N_a100)];
%arreglo2=Nd/cm;
save Occupied_1mW.dat arreglo1 -ascii
%save Nd.dat arreglo2 -ascii
toc
```

McMaster University

McMaster University

Bibliography

[1] Juthika Basak, Ling Liao, Ansheng Liu, Doron Rubin, Yoel Chetrit, Hat Nguyen, Dean Samara-Rubio, Rami Cohen, Nahum Izhaky, and Mario Paniccia. "Development in Gigascale Silicon Optical Modulator Using Free Carrier Dispersion Mechanism". *Advances in Optical Technologies*, 2008:1–10, 2008.

[2] Bahram Jalali. "Can Silicon Change Photonics". *Physica Status Solidi A*, 205(2):213–224, February 2008.

[3] Richard A. Soref. "Silicon Photonics Technology: past, present and future". *Optoelectronic Integration on Silicon II, proc SPIE*, 5730:18–28, 2005.

[4] Maria L. Calvo and Vasudevan Lakshminarayanan, editors. *"Optical Waveguides: From Theory to Applied Technologies"*. Optical Science and Engineering Series. CRC, 1 edition, 2007.

[5] T. Barwicz, H. Byun, F. Gan, C. W. Holzwarth, M. A. Popovic, P. T. Rakich, M. R. Watts, E. P. Ippen, F. X. Kartner, H. I. Smith, J. S. Orcutt, R. J. Ram, V. Stojanovic, O. O. Olubuyide, J. L. Hoyt, S. Spector, M. Geis, M. Grein, T. Lyszczarz, and J. U. Yoon. "Silicon photonics for compact, energy-efficient interconnects". *Journal of Optical Networking*, 6(1):63–73, January 2007.

[6] Graham T. Reed and C. E. Jason Png. "Silicon Optical Modulators". *Materials Today*, 8(1):40–50, January 2005.

McMaster University

[7] Richard A. Soref and Joseph P. Lorenzo. "All-silicon active and passive guided-wave components for wavelength 1.3 and 1.6 um". *IEEE J. Quantum Electron*, QE-22(6):873–879, June 1986.

[8] Graham T. Reed. "The Optical Age of Silicon". *Nature*, 427:595–596, 2004.

[9] Richard A. Soref. "Silicon-Base Optoelectronics". *Proc. IEEE*, 81(12):1687–1706, December 1993.

[10] Leonid Tsybeskov, David J. Lockwood, and Masakazu Ichikawa. "Silicon photonics: Cmos going optical". *Proceedings of the IEEE*, 97(7):1161–1165, July 2009.

[11] Hank Hogan. "Silicon photonics could save the computer industry". *Photonics Spectra*, 44(3), March 2010.

[12] Michal Lipson. "Guiding, Modulating, and Emitting Light on Silicon–Challenges and Opportunities". *Journal of Lightwave Technology*, 23(12):4222–4238, December 2005.

[13] Bahram Jalali and Sasan Fathpour. "Silicon Photonics". *Journal of Lightwave Technology*, 24(12):4600–4615, December 2006.

[14] Lorenzo Pavesi and David J. Lockwood, editors. *Silicon Photonics*, volume 94 of *Topics in Applied Physics*. Springer-Verlag, 1 edition, 2004.

[15] Bahram Jalali, Sasan Fathpour, and Kevin Tsia. "Green Silicon Photonics". *Optics and Photonics News*, 20(6):18–23, June 2009.

[16] G. G. Shahidi. "SOI Technology for the GHz era ". *IBM J. Res. & Dev.*, 46(2/3):121 – 130, March/May 2002.

McMaster University

[17] Graham T. Reed and Andrew P. Knights. *"Silicon Photonics an Introduction"*. John Wiley and Sons Ltd, 111 River Street Hoboken NJ 07030 USA, 1st edition, 2004.

[18] Bahram Jalali. "Silicon-on-Insulator Photonic Integrated Circuit (SOI-PIC) Technology". *Proc. SPIE*, 2997:60–71, 1997.

[19] K. Petermann. "Properties of Optical rib-waveguides with large cross-section". *Arch. Elektron. Ubertrag. Tech.*, 30:139–140, 1976.

[20] U. Hilleringmann and K. Goser. "Optoelectronic System Integration on Silicon: Waveguides, Photodetectors, and VLSI CMOS Circuits on One Chip". *IEEE TRANSACTIONS ON ELECTRON DEVICES*, 42(5):841–846, May 1995.

[21] Pieter Dumon, Gino Priem, Luis Romeu Nies, Wim Bogaerts, Dries Van Thourhout, Peter Bienstman, Tak Keung Lianf, Masahiro Tsuchiya, Patrick Jaenen, Stephan Beckx, Johan Wouters, and Roel Baets. "Linear and Nonlinear Nanophotonic Devices Based on Silicon-on-Insulator Wire Waveguides". *Japanese Journal of Applied Physics*, 45(8B):65896602, August 2006.

[22] Haisheng Rong, Ansheng Liu, Richard Jones, Oded Cohen, Dani Hak, Remus Nicolaescu, Alexander Fang, and Mario Paniccia. "An all-silicon Raman Laser". *Nature*, 433:725–728, January 2005.

[23] Jurgen Michel, Jifeng Liu, and Lionel C. Kimerling. "High-performance Ge-on-Si photodetectors". *Nature Photonics*, 4:527–534, August 2010.

[24] F. Y. Gardes, G. T. Reed, A. P. Knights, and G. Mashanovich. "Evolution of Optical Modulation using Majority Carrier Plasma Dispersion effect in SOI". *Proc. of SPIE*, 6898:68980C–1 – 68980C–10, 2008.

McMaster University

[25] Michael R. Watts, William A. Zortman, Douglas C. Trotter, Ralph W. Young, and Anthony L. Lentine. "Low-Voltaje, Compact, Depletion-Mode, Silicon Mach-Zehnder Modulator". *Journal of Selected Topics in Quantum Electronics*, 16(1):159–164, January/February 2010.

[26] Amnon Yariv and Pochi Yeh. *"Photonics, Optical Electronics in Modern Communications"*. Electrical and Computer Engineering. Oxford University Press, 198 Madison Avenue, New York, NY 10016, 6th edition, 2007.

[27] Clifford Pollock and Michal Lipson. *"Integrated Photonics"*. Optics. Kluwer Academic Publishers, first edition, 2003.

[28] Pochi Yeh. *"Optical wave in crystal: Propagation and Control of Laser Radiation"*. Wiley-Interscience, 1 edition, November 2002.

[29] Richard A. Soref and Brian R. Bennett. "Electrooptical Effects in Silicon". *IEEE J. Quantum Electron*, 23(1):123–129, Jan 1987.

[30] Ansheng Liu, Ling Liao, Doron Rubin, Juthika Basak, Yoel Chetrit, Hat Nguyen, Rami Cohen, Nahum Izhaky, and Mario Paniccia. "Recent development in a high-speed silicon optical modulator based on reverse-biased pn diode in a silicon waveguide". *Semiconductor Science and Technology*, 23(6):1–7, May 2008.

[31] Mao-Teng Hsua, Ricky W. Chuang, and Jia-Ching Liaoa. "Silicon p-i-n optical waveguide modulators fabricated on the silicon and silicon-on-insulator substrates". *Proc. of SPIE*, 6475:1–6, 2007.

[32] Ansheng Liu, Ling Liao, Doron Rubin, Hat Nguyen, Berkehan Ciftcioglu, Yoel Chetrit, Nahum Izhaky, and Mario Paniccia. "High-speed optical modulation

McMaster University

based on carrier depletion in a silicon waveguide". *Opt. Express*, 15:660–668, 2007.

[33] Zhi Yong Li, Dan Xia Xu, W. Ross McKinnon, Siegfried Janz, Jens H. Schmid, Pavel Cheben, and Jin-Zhomg Yu. "Silicon Waveguide Modulator Base on Carrier Depletion in Periodically Interleaved PN-Junctions". *Optics Express*, 17(18):15947–15958, August 2009.

[34] G. T. Reed, G. Mashanovich, F. Y. Gardes, and D. J. Thomson. "Silicon Optical Modulators". *Nature Photonics*, 4:518–526, August 2010.

[35] Delphine Marris-Morini, Laurent Vivien, Gilles Rasigade, Jean-Marc Fedeli, Eric Cassan, Xavier Le Roux, Paul Crozat, Sylvain Maine, Anatole Lupu, Philippe Lyan, Pierrette Rivallin, Mathieu Halbwax, and Suzanne Laval. "Recent Progress in High-Speed Silicon-Based Optical Modulators". *Proceedings of the IEEE*, 97(7):1199–1215, July 2009.

[36] G. V. Treyz, Paul G. May, and Jean-Marc Halbout. "Modulators at 1.3 um Based on Free-Carrier Absorption". *IEEE Electron Device Letters*, 12(6):276–278, June 1991.

[37] C. K. Tang, G. T. Reed, A. J. Walton, and A. G. Rickman. "Low-Loss, Single-Mode, Optical Phase Modulator in SIMOX Material". *Journal of Lightwave Technology*, 12(8):1394–1400, August 1994.

[38] Ansheng Liu, Richard Jones, Ling Liao, Dean Samara-Rubio, Doron Rubin, Oded Cohen, Remus Nicolaescu, and Mario Paniccia. "A high-speed silicon optical modulator based on a metaloxidesemiconductor capacitor". *Nature*, 427:615–618, February 2004.

McMaster University

[39] F. Y. Gardes, G. T. Reed, N.G. Emerson, and C.E. Png. "A sub-micron depletion-type photonic modulator in Silicon On Insulator". *Opt. Express*, 13(22):8845–8854, October 2005.

[40] D F Logan, P E Jessop, A P Knights, G Wojcik, and A Goebel. "Optical Modulation in SiliconWaveguides via Charge State Control of Deep Levels". *Opt. Express*, 17(21):18571–18580, 2009.

[41] Pochi Yeh. *"Optical Waves in Layered Media"*. Pure and Applied Optics. John Wiley and Sons Ltd, 111 River Street Hoboken NJ 07030 USA, 1st edition, 2005.

[42] Dietrich Marcuse. *"Light Transmission Optics"*. Van Nostrand Reinhold Company, 450 West 33rd street NY, 1st edition, 1972.

[43] Theodor Tamir. *"Guided-Wave Optoelectronics"*, volume 26 of *Springer Series in Electronics and Photonics*. Springer-Verlag, Tiergartenstrasse 17, D-6900 Heidelberg, Germany, 2nd edition, 1990.

[44] Amnon Yariv and Pochi Yeh. *"Photonics: Optical Electronics in Modern Communications"*. The Oxford Series in Electrical and Computer Engineering. Oxford University Press, 6 edition, January 2006.

[45] Hiroshi Nishihara, Masamitsu Haruna, and Toshiaki Suhara. *"Optical Integrated Circuits"*. McGraw-Hill Optical and Electro-Optical Engineering Series. McGraw Hill, 1221 Avenue of the Americas New York, NY 10020, 1st edition, 1985.

[46] Donald L. Lee. *"Electromagnetic Principles of Integrated Optics"*. John Wiley and Sons Inc, 111 River Street Hoboken NJ 07030 USA, 1st edition, June 1986.

McMaster University

[47] Katsunari Okamoto. *"Fundamentals of Optical Waveguides"*. Academic Press, 2 edition, December 2005.

[48] Masanori Koshiba. *"Optical Waveguide Analysis"*. Advanced Science and Technology Series. McGraw-Hill Professional, 1 edition, 1992.

[49] Kenji Kawano and Tsutomu Kitoh. *"Introduction to Optical Waveguide Analysis: Solving Maxwell's Equation and the Schrdinger Equation"*. Wiley-Interscience, 1 edition, July 2001.

[50] F. L. Pedrotti and L. S. Pedrotti. *"Introduction to Optics"*. Prentice-Hall, Upper Saddle River NJ, 2nd edition, June 1993.

[51] Keiko Iizuka. *"Elements of Photonics"*, volume II of *Wiley Series in Pure and Applied Optics*. Wiley-Intescience, first edition, 2002.

[52] Bahaa E. A. Saleh and Malvin Carl Teich. *Fundamentals of Photonics*. Wiley-Interscience, August 1991.

[53] Mark Fox. *"Optical Properties of Solids"*. Oxford Master Series in Condensed Matter Physics. Oxford University Press, first edition, 2005.

[54] Matthew N. O. Sadiku. *"Elements of Electromagnetics"*. Electrical and Computer Engineering. Oxford University Press, 198 Madison Avenue, New York, NY 10016, 3rd edition, 2001.

[55] Bahaa E. A. Saleh and Malvin Carl Teich. *"Fundamenlas of Photonics"*. Pure and applied optics. John Wiley and Sons, Inc., 111 River Street Hoboken NJ 07030 USA, 1st edition, 1991.

McMaster University

[56] Prosenjit Rai-Choudhury, editor. *"MEMS and MOEMS Technology and Applications"*, volume PM85. SPIE Press, Bellingham, Washintong 98227-0010, 1st edition, 2000.

[57] T. Zinke, U. Fisher, A. Splett, B. Schuppert, and K. Petermann. "Comparison of Optical Waveguide Losses in Silicon-on-Insulator". *Electron. Lett.*, 29(23):2031–2033, Nov 1993.

[58] J. Schmidtchen, A. Splett, B. Schuppert, and K. Petermann. "Low Loss Singlemode Optical Waveguides with large Cross-Section in Silicon-On-Insulator". *Electronics Letter*, 27(16):1486–1488, August 1991.

[59] R. A. Soref, J. Schmidtchen, and K. Petermann. "Large single-mode RIB waveguides in GeSi-Si and Si-on-SiO_2". *IEEE J. Quantum Electron*, 27(8):1971–1974, Aug 1991.

[60] S. P. Pogossian, L. Vescan, and A. Vonsovici. "The single-mode condition for semiconductor Rib Waveguide with Large Cross Section". *J. Lightwave Technol.*, 16(10):1851–1853, Oct. 1998.

[61] A. G. Rickman, G. T. Reed, and Fereydoon Namavar. "Silicon-on-Insulator Optical Rib Waveguide Loss and Mode Characteristics". *J. Lightwave Technol.*, 12(10):1771–1776, Oct 1994.

[62] Olly Powell. "Single-Mode Conditionfor Silicon Rib Waveguides". *J. Lightwave Technol. Lett.*, 20(10):1851–1855, Oct. 2002.

[63] Olly Powell. "Erratum to Single-Mode Conditionfor Silicon Rib Waveguides". *J. Lightwave Technol. Lett.*, 21(3):868, Mar. 2003.

McMaster University

[64] Timo T. Aalto, Mikko Harjanne, Markku Kapulainen, Paivi Heimala, and Matti J. Leppihalme. "Development of Silicon-On-Insulator Waveguide Technology". *Proceedings of SPIE*, 5355:81–95, May 2004.

[65] Martina de Laurentis, Andrea Irace, and Giovanni Breglio. "Determination of single-mode condition in dielectric rib waveguide with large cross section by finite element analisys". *J. Comput. Electron.*, 6:285–287, 2007.

[66] J. Lousteau, A. B. Seddon D. Furniss, T. M. Benson, A. Vukovic, and P. Sewell. "The Single-Mode Condition for Silicon-on-Insulator Optical Rib Waveguide with Large Cross Section". *J. Lightwave Technol. Lett.*, 22(8):1923–1929, August 2004.

[67] Edmond J. Murphy. *"Integrated Optical Circuits and Components: Design and Applications"*. Optical Engineering. Marcel Dekker, 270 Madison Avenue, New York, NY 10016, 1st edition, August 1999.

[68] Dieter W Pohl and S. E. Schwarz. "Thermo- and Elasto-optic Parameters of NaF and their implications for light scattering from second sound ". *Phys. Rev. B*, 7(6):2735 – 2739, March 1973.

[69] Robert G. Hunsperger. *"Integrated Optics: Theory and Technology"*, volume 33 of *Springer series in Optical Sciences*. Springer-Verlag, Tiergartenstrasse 17, W-6900 Heidenberg, Germany, 5th edition, 2002.

[70] V. Subramaniam, G. N. De Brabander, D. H. Naghski, and J. T. Boyd. "Measurement of Mode Field Profiles and Bending and Transition losses in curved optical channel Waveguides". *J. Lightwave Technol.*, 15(6):990–997, June 1997.

[71] E. A. J. Marcatali. "Dielectric Rectangular Waveguides and Directional Coupler for Integrated Optics". *B.S.T.J.*, 48(7):2071–2102, September 1969.

McMaster University

[72] Shaodong Wu and Hans J. Frankena. "Integrated optical sensor using micromechanical bridges and cantilivers". *SPIE Integrated Optics and Microstructures*, 1793:83–89, 1992.

[73] Ben G. Streetman and Sanjay Banerjee. *"Solid State Electronic Devices"*. Prentice Hall, 5 edition, 2000.

[74] F. Gan, F.J. Grawert, J.-M. Schley, S. Akiyama, J. Michel, K. Wada, L.C. Kimerling, and F.X. Kartner. "Design of all-optical switches based on carrier injection in si/sio/sub 2/ split-ridge waveguides (srws)". *Lightwave Technology, Journal of*, 24(9):3454–3463, Sept. 2006.

[75] Martin A. Green and Mark J. Keevers. "Optical Properties of Intrinsic Silicon at 300K". *Progress in Photovoltaics: Research and Applications*, 3:189–192, 1995.

[76] R. Santbergen. *"Optical Absorption Factor of Solar Cells for PVT Systems"*. Eindhoven University Press, 2008.

[77] R. A. Soref and B. R. Bennett. "Kramers-Kronig analisys of Electro-Optic switch in silicon". *SPIE Integrated Opt. Circuit Eng.*, 704:32–37, 1986.

[78] Simon M. Sze and Kwok K. Ng. *"Physics of Semiconductor Devices"*. Wiley-Interscience, 3 edition, October 2006.

[79] Gerold W. Neudeck. *"The PN-Junction Diode"*, volume II of *Modular Series on Solid State Devices*. Prentice Hall, 2 edition, January 1988.

[80] Martin A. Green. *Solar Cells: Operating Principles, Technology and Systems Applicatinos*. Prentice Hall, 1982.

McMaster University

[81] Shyh Wang. *Fundamentals of Semiconductors Theory and Devices Physics*. The Prentice Hall series in electrical and computer engineering. Prentice-Hall, first edition, 1989.

[82] C. S. Chen and J. C. Corelli. "Infrared Spectroscopy of Divacancy-Associated Radiation-Induced Absorption Bands in Silicon". *Phys. Rev. B*, 5(4):1505–1517, Feb 1972.

[83] D. F. Logan, P. E. Jessop, A. P. Knights, R. M. Gwilliam, and P. Halsall. "The Effect of Doping Type and Concentration on Optical Absorption via Implantation Induced Defects in Silicon-On-Insulator Waveguides". *COMMAD 2008 IEEE Proc. Conf. on Optoelectronics and Microelectronic Materials and Devices*, pages 152–155, 28 2008-aug. 1 2008.

[84] Sokrates T. Pantelides. "The Electronic Structure of Impurities and other point defects in semiconductors". *Rev. Mod. Phys.*, 50(4):797–858, Oct 1978.

[85] H. G. Grimmeiss. "Deep Level Impurities in Semiconductors". *Annual Review of Materials Science*, 7:341–376, 1977.

[86] James D. Plummer, Michael D. Deal, and Peter B. Griffin. *"Silicon VLSI Technology: Fundamentals, Practice, and Modeling"*. Prentice Hall Electronics and Vlsi Series. Prentice Hall, July 2000.

[87] Joseph H. Nevin and H. Thurman Henderson. "Thallium-Doped Silicon Ionization and Excitation Levels by Infrared Absorptino". *Journal of Applied Physics*, 46(5):2130–2133, May 1975.

[88] S. D. Brotherton and A. Gill. "The EnergyLlevel of Thallium in Silicon. *Applied Physics Letters*, 33(11):953–955, December 1978.

[89] Walter Scott and J. L. Schmit. "Infrared Excitation Spectrum of Thallium-Doped Silicon". *Applied Physics Letters*, 33(4):294–296, August 1978.

[90] W. Shockley and W. T. Read. "Statistics of the Recombination of Holes and Electrons". *Physical Review*, 87(5):835–842, September 1952.

[91] R. N. Hall. "electron-Hole Recombination in Germanium". *Phys. Rev*, 87:387, 1952.

[92] M. J. Keevers and M. A. Green. "Efficiency improvements of silicon solar cell by impurity photovoltaic effect". *Journal of Applied Physics*, 75(8):4022–4031, April 1994.

[93] Y. K. Hsieh and H. C. Card. "Limitation to Shockley-Read-Hall model due to direct photoionization of the defect states". *Journal of Applied Physics*, 65(6):2409–2415, March 1989.

[94] Robert F. Pierret. *"Advance Semiconductors Fundamentals"*, volume VI of *Modular Series on Solid State Devices*. Prentice Hall, 2 edition, August 2002.

[95] Dieter K. Schroder. *"Semiconductor Material and Device Characterization"*. Wiley-IEEE Press, 3 edition, January 2006.

[96] Martin A. Green. "Intrinsic Concentration, Effective Densities of States, and Effective Mass in Silicon". *Journal of Applied Physics*, 67(6):2944–2954, March 1990.

[97] Baoxing Zhao, Jichng Zhou, and Yongmin Chen. "Numerical simulation of the Impurity Photovoltaic Effect in Silicon Solar Cells Doped with Thallium". *Physica B*, 10(12):1016, June 2010.

McMaster University

[98] Robert Hull, editor. *"Properties of Crystalline Silicon"*. INSPEC, The institution of Electrical Engineers, 1999.

[99] H. Thurman Henderson and K. L. Ashley. "A Negative Resistance Diode based upon double injection in Thallium-Doped Silicon". *Proceedings of the IEEE*, 57(9):1677–1677, September 1969.

[100] N. A. Stolwijk and H. Bracht. *"Diffusion in Silicon, Germanium and their Alloys"*, volume III/33, Subvolume A of *Landolt-Brnstein New Series*. Springer, New York, 1998.

[101] Daniel K. Sparacin, Steven J. Spector, and Lionel C. Kimerling. Silicon waveguide sidewall smoothing by wet chemical oxidation. *Journal of Lightwave Technology*, 23(8):2455–2461, August 2005.

[102] G. K. Celler, D. L. Barr, and J. M. Rosamilia. "Etching of Silicon by the RCA Standard Clean 1". *Electrochemical and Solid-State Letters*, 3(1):47–49, 2000.

[103] P. M. Fahey, P. B. Griffin, and J. D. Plummer. "Point Defects and Dopant Diffusion in Silicon". *Reviews of Modern Physics*, 61(2):289–384, April 1989.

[104] S. M. Hu, P. Fahey, and R. W. Dutton. "On Models of Phosphorus Diffusion in Silicon". *Journal of Applied Physics*, 54(12):6912–6922, December 1983.

[105] Kunihiro Yagi, Nobuo Miyamoto, and Jun ichi Nishizawa. "Anomalous diffusion of phosphorus into silicon". *Japanese Journal of Applied Physics*, 9(3):246–254, March 1970.

[106] Masashi Uematsua. "Simulation of boron, phosphorus, and arsenic diffusion in silicon based on an integrated diffusion model, and the anomalous phosphorus

McMaster University

diffusion mechanism". *Journal of Applied Physics*, 82(5):2228–2246, September 1997.

[107] Scotten W. Jones. "Diffusion in Silicon". www.icknowledge.com/, April 2008.

[108] Inc. Silvaco Data System. Athena. www.silvaco.com, 1984-2010.

[109] R. Newman. "Optical Properties of Indium-Doped Silicon. *Phys. Rev*, 99(2):465–467, July 1955.

[110] A. Sato, K. Suzuki, H. Horie, and T. Sugii. "Determination of Solid Solubility Limit of In and Sb in si using bonded Silicon-On-Insulator (SOI) Substrate". *Proc. IEEE 1995 Int. Conference on Microelectronic Test Structures*, 8:259–263, 1995.

[111] Inc. RSoft Design Group. Beamprop. http://www.rsoftdesign.com, 1990-2011.

[112] Gregory T. A. Kovacs, Nadim I. Maluf, and Kurt E. Petersen. "Bulk Micromachining of Silicon". *Proceedingsof the IEEE*, 86(8):1536–1551, August 1998.

[113] Oliver Powell and H. Barry Harrison. "Anisotropic etching of {100} and {110} Planes in (100) Silicon". *Journal of Micromechanics and Microengineering*, 11:217220, 2001.

[114] D. B. Lee. Anisotropic etching of silicon. *Journal of Applied Physics*, 40:4569–4574, 1969.

[115] James Ziegler. "SRIM - the Stopping and Range of Ions in Matter". http://www.srim.org/, 2009.

[116] Department of Electrical and Computer Engineering. *"Theory and Fabrication of Integrated Circuits"*. University of Illinois at Urbana-Champaign, 1308 West Green St. Urbana, IL 61801, 2009.

McMaster University

[117] M. Finetti, P. Ostoja, S. Solmi, and G. Soncini. "Aluminum-Silicon Ohmic Contact on "Shallow" n+/p Junctions". *Solid-State Electronics*, 23:255–262, 1980.

[118] G. Tittelbach, B. Richter, and W. Karthe. "Comparison of Three Transmission Methos for Integrated Optical Waveguide Propagation Loss Meassurement". *Pure Appl. Opt.*, 2:683–706, 1993.

[119] Atsushi Sakai, Go Hara, and Toshihiko Baba. "Propagation Characteristics of Ultrahigh-Δ Optical Waveguide on Silicon-on-Insulator Substrate". *Jpn. J. Appl. Phys.*, 40(4B):L383–L385, April 2001.

[120] M. Wolf. "Limitations and Possibilities for Improvement of Photovoltaic Solar Energy Converters: Part 1: Considerations for earth's surface operation". *Proceedings of the IRE*, 48(7):1246 – 1263, July 1960.

[121] M. Schmeits and A. A. Mani. "Impurity Photovoltaic Effect in c -Si Solar Cells. A Numerical Study". *Journal of Applied Physics*, 85(4):2207–2212, November 1998.

[122] S. Khelifi, J. Verschraegen, M. Burgelman, and A. Belghachi. "Numerical Simulation of the Impurity Photovoltaic Effect in Silicon Solar Cell". *Renewable Energy*, 33:293–298, 2008.

[123] S. Zh. Karazhanov. "Impurity Photovoltaic Effect in Indium-Doped Silicon Solar Cells". *Journal of Applied Physics*, 89(7):4030–4036, January 2001.

[124] William Shockley and Hans J. Queisser. "Detailled Balans Limit of Efficiency of p-n Junction Solar Cells". *Journal of Applied Physics*, 32(3):510–519, March 1961.

McMaster University

[125] P. Wurfel. "Limiting Efficiency for Solar Cells with Defects from a Three-level Model". *Solar Energy Materials and Solar Cells*, 29:403–413, 1993.

[126] T. S. Navruz and M. Sarita. "Efficiency Variation of the Intermediate Band Solar Cell due to the Overlap Between Absorption Coefficients". *Solar Energy Materials and Solar Cells*, 92(3):273–282, March 2008.

[127] Albert S. Lin, Weiming Wang, and Jamie D. Phillips. "Model for Intermediate Band Solar Cells Incorporating Carrier Transport and Recombination". *Journal of Applied Physics*, 105(064512):1–8, March 2009.

[128] Hiroto Kasai and Hideki Matsumura. "Study for Improvement of Solar Cell Efficiency by IPV Effect". *Solar Energy Materials and Solar Cells*, 48:93–100, 1997.

[129] Akeed A. Pavel, M. Rezwan Khan, and N.E. Islam. "On the possibility of improving silicon solar cell efficiency through impurity photovoltaic effect and compensation". *Solid-State Electronics*, 54:12781283, 2010.

[130] Jenny Nelson. *"The Physics of Solar Cells"*. World Scientific Publishing, 1st edition, December 2006.

[131] Wilfried G J H M van Sark. "Teaching the Relation Between Solar Cell Efficiency and Annual Energy Yield". *European Journal of Physics*, 28(4):415–427, March 2007.

[132] Stephen J. Fonash. *"Solar Cell Device Physics"*. Solid state physics. Academic Press, 2nd edition, 2010.

[133] Hiroto Kasai and Hideki Matsumura. "Optical Absorption Properties

McMaster University

of Indium-Doped Thin Crystalline Silicon Films". *Jpn. J. Appl. Phys.*, 37(10):5609–5613, October 1998.

[134] Hiro Kasai, Toshiyuki Sato, and Hideki Matsumura. "Impurity Photovoltaic Effect in Crystalline Silicon Solar Cells". In *Photovoltaic Specialists Conference, 1997., Conference Record of the Twenty-Sixth IEEE*, pages 215 – 218, Anaheim, CA , USA, Sept. 30 to Oct. 3 1997.

[135] H. Seidel, L. Csepregi, A. Heuberger, and H. Baumgartel. "anisotropic etching of crystalline silicon in alkaline solutions, i. orientation dependence and behavior of passivation layers". *Electrochem. Soc.*, 137(11):3612–3626, Novemver 1990.

McMaster University